SMOOTH SLIDING CONTROL AND EXTREMUM SEEKING APPLIED TO WIND TURBINES

Gabriel Felippe da Cruz Pacheco

Dissertação de Mestrado apresentada ao Programa de Pós-graduação em Engenharia Elétrica, COPPE, da Universidade Federal do Rio de Janeiro, como parte dos requisitos necessários à obtenção do título de Mestre em Engenharia Elétrica.

Orientador: Alessandro Jacoud Peixoto

Rio de Janeiro
Março de 2018

SMOOTH SLIDING CONTROL AND EXTREMUM SEEKING APPLIED TO WIND TURBINES

Gabriel Felippe da Cruz Pacheco

DISSERTAÇÃO SUBMETIDA AO CORPO DOCENTE DO INSTITUTO ALBERTO LUIZ COIMBRA DE PÓS-GRADUAÇÃO E PESQUISA DE ENGENHARIA (COPPE) DA UNIVERSIDADE FEDERAL DO RIO DE JANEIRO COMO PARTE DOS REQUISITOS NECESSÁRIOS PARA A OBTENÇÃO DO GRAU DE MESTRE EM CIÊNCIAS EM ENGENHARIA ELÉTRICA.

Examinada por:

Prof. Alessandro Jacoud Peixoto, D.Sc.

Prof. Fernando Cesar Lizarralde, D.Sc.

Prof. Tiago Roux de Oliveira, D.Sc.

RIO DE JANEIRO, RJ – BRASIL
MARÇO DE 2018

Pacheco, Gabriel Felippe da Cruz

Smooth Sliding Control and Extremum Seeking Applied to Wind Turbines/Gabriel Felippe da Cruz Pacheco. – Rio de Janeiro: UFRJ/COPPE, 2018.

XIV, 73 p.: il.; 29, 7cm.

Orientador: Alessandro Jacoud Peixoto

Dissertação (mestrado) – UFRJ/COPPE/Programa de Engenharia Elétrica, 2018.

Bibliografia: p. 68 – 73.

1. Estrutura Variável. 2. Modos Deslizantes. 3. Busca Extremal. 4. Sistemas Não-Lineares. 5. Sistemas de Conversão de Energia Eólica. I. Peixoto, Alessandro Jacoud. II. Universidade Federal do Rio de Janeiro, COPPE, Programa de Engenharia Elétrica. III. Título.

Agradecimentos

Primeiramente, agradeço ao Prof. Alessandro Jacoud pela orientação acadêmica, pelo apoio e pela dedicação de levar este trabalho sempre na primeira pessoa do plural. Obrigado também por acreditar ser possível fazer uma dissertação de mestrado mesmo com todos os percalços que existem ao se trabalhar simultaneamente.

Estendo meus agradecimentos ainda aos meus pais, Sandra e Nereu, e à minha irmã, Ana Carolina, que sempre estiveram do meu lado, desde muito antes do meu ingresso na engenharia. Obrigado por serem sempre meu refúgio, meu porto seguro, meus torcedores de carteirinha. Diariamente, vocês me dão a força que me faz seguir em frente de cabeça erguida em busca dos meus sonhos e sabem que são, os três, meus exemplos a serem seguidos.

Muito obrigado ao meu amor, minha companheira de vida, Jéssica Oliveira, que embarcou comigo no meio desta jornada e que, com todo seu amor, carinho, cuidado, compreensão e ajuda, abdicou de seus próprios momentos em família e com amigos para que eu pudesse completar esta etapa de forma bem sucedida. Espero te fazer feliz todos os dias e levar à tua vida pelo menos a metade de todos os sentimentos incríveis que tu trazes à minha.

Por fim, agradeço a todos os meus familiares e amigos que tenho como irmãos que estiveram comigo durante este percurso, souberam compreender quando não pude estar presente e, por vezes, me forçaram a estar mesmo quando eu não julgava que deveria. Muito obrigado por me lembrarem diariamente que viver é muito mais que alcançar objetivos pessoais, acadêmicos ou profissionais. A vida é sobre momentos e experiências, é sobre as boas relações que cultivamos.

Cada um de vocês é extremamente importante para mim e, por isso, divido esta conquista com todos aqui mencionados. Não houvesse vocês nessa caminhada, não sou capaz de julgar qual teria sido o desfecho, mas uma coisa posso afirmar com convicção: o caminho não teria sido tão bonito e muito menos tão divertido. Muito obrigado!

Resumo da Dissertação apresentada à COPPE/UFRJ como parte dos requisitos necessários para a obtenção do grau de Mestre em Ciências (M.Sc.)

CONTROLE SUAVE POR MODOS DESLIZANTES E BUSCA EXTREMAL APLICADOS A TURBINAS EÓLICAS

Gabriel Felippe da Cruz Pacheco

Março/2018

Orientador: Alessandro Jacoud Peixoto

Programa: Engenharia Elétrica

Este estudo se direciona à aplicação de controle por busca extremal (ESC) em uma malha de controle externa a fim de realizar o rastreamento de ponto de máxima potência (MPPT). Para o caso no qual medições de potência não estão disponíveis, um mecanismo para estimação de torque ou potência é proposto. Este algoritmo de otimização não necessita qualquer tipo de medida ou estimação da velocidade do vento nem de conhecimento prévio acerca da curva de potência da turbina.

Na malha de controle interna, um controlador não linear robusto também é projetado a fim de garantir rastreamento prático global para a velocidade angular do rotor da turbina. A parte robusta do controlador, que mantém uma resposta transiente rápida, é baseada em controle por modos deslizantes mas apresenta um sinal de controle suavizado (SSC), evitando *chatttering*. Tal controlador fora previamente projetado para sistemas lineares com grau relativo arbitrário, este trabalho apresenta uma primeira generalização para classe de plantas não-lineares representada pelos sistemas de conversão de energia eólica. Além disso, o algoritmo de controle não necessita de medidas de fluxos do estator ou de observadores desta variável. O mesmo é projetado usando uma propriedade de estabilidade inerente à dinâmica do WECS e demonstrada neste documento, chamada de estabilidade entrada para estado com relação à velocidade de rotação do rotor da turbina e suas derivadas no tempo.

A análise de estabilidade em malha fechada para o sistema de conversão de energia eólica é fornecida considerando a malha interna com SSC e a externa com uma variação do ESC baseado em perturbações senoidais. A eficácia do esquema de otimização e controle proposto é evidenciada através de simulações numéricas.

Abstract of Dissertation presented to COPPE/UFRJ as a partial fulfillment of the requirements for the degree of Master of Science (M.Sc.)

SMOOTH SLIDING CONTROL AND EXTREMUM SEEKING APPLIED TO WIND TURBINES

Gabriel Felippe da Cruz Pacheco

March/2018

Advisor: Alessandro Jacoud Peixoto

Department: Electrical Engineering

This study addresses the application of extremum seeking control (ESC) in an outer loop to perform the maximum power point tracking (MPPT) in wind energy conversion systems (WECS). For the case when power measurements are not available, a torque or power estimation scheme is proposed. This optimization algorithm is categorized as a Hill Climb Search (HCS) control and does not require any measurement or estimation of the wind speed nor previous knowledge about the turbine's power-curve.

It is also designed a nonlinear robust controller for the inner loop in order to achieve global practical tracking of the turbine's rotor speed. The robust part of the controller, which maintains fast transient response, is based on sliding mode control that features a smooth control signal (SSC), free of *chattering*, previously designed for linear plants with arbitrary relative degree. In this sense, this work presents a first generalization of this controller for the class of nonlinear plants representing the WECS dynamics. Moreover, the proposed robust inner loop control does not require measurements of the stator flux nor any flux observer. The controller is designed by using an inherent stability property of the WECS dynamics demonstrated in this document, named, the input-to-state stable with respect to the turbine angular velocity and its time derivatives.

The closed-loop stability analysis is provided considering the WECS with an inner loop with SSC and an outer loop with a variation of the ESC based on sinusoidal perturbations. The effectiveness of the proposed scheme is supported by analysis and simulation results.

Contents

List of Figures

List of Tables

List of Acronyms

Abbreviations

MPPT Maximum Power Point Tracking

MPP Maximum Power Point

ESC Extremum Seeking Control

VSC Variable Structure Control

SMC Sliding Mode Control

WECS Wind Energy Conversion Systems

FOC Field Oriented Control

PI Proportional-Integral

HAWT Horizontal Axis Wind Turbine

VAWT Vertial Axis Wind Turbine

TSR Tip Speed Ratio

PSF Power Signal Feedback

HCS Hill-Climb Search

MPC Model Predictive Control

IG Induction Generator

SCIG Squirrel Cage Induction Generator

AC Alternate Current

DC Direct Current

SVPWM Space Vector Pulse Width Modulation

SISO Single-Input-Single-Output

$\mathcal{UB}$ Uniformly Norm Bounded

BIBO Bounded-Input Bounded-Output

GAS Globally Asymptotic Stability

Nomenclature

P_w Wind Power Available at the Blade [W]

ρ_a Air Density [kg/m^3]

S Cross-sectional Surface [m^2]

V Wind Speed [m/s]

λ Tip Speed Ratio [Dimensionless]

R Maximum Radius of the Rotating Turbine / Blade Length [m]

ω_t Turbine's Angular Speed [rad/s]

P_m Actual Available Mechanical Power [W]

C_p Power Coefficient [Dimensionless]

T_a^V Aerodynamic Torque [N m]

$\mathcal{B}$ Pitch Angle [rad]

J_t Turbine's Moment of Inertia [kg m^2]

I_α α Stator Current Component on the (α, β) Model [A]

I_β β Stator Current Component on the (α, β) Model [A]

λ_α α Stator Flux Component on the (α, β) Model [V m]

λ_β β Stator Flux Component on the (α, β) Model [V m]

θ_0 Rotor Flux Position [rad]

ω_0 Stator Electrical Frequency [rad/s]

V_{om} Stator Peak Amplitude Voltage [V]

L_m Mutual Inductance [H]

R_r Rotor Electric Resistance [Ω]

L_s Stator Electric Inductance [H]

R_s Stator Electric Resistance [Ω]

T_e Electromagnetic Torque [N m]

T_L Load Torque created by Spring-Damper Model [N m]

J Rotor's Moment of Inertia [kg m^2]

p Number of Pole Pairs [Dimensionless]

n Gearbox Reduction Ratio [Dimensionless]

ω_r Generator's Rotor Frequency [rad/s]

$\tilde{\theta}$ Angle Between Wind Turbine and Generator's Electrical Angular Positions [rad]

K_s Spring Stiffness Coefficient [N m/rad]

B Damping Ratio Coefficient [N m s/rad]

Chapter 1

Introduction

In the past decades, renewable energy has been a hot topic among both academic and industrial segments. Over the last 25 to 30 years, studies [4, 7–9] have shown that the worlsd's main energetic grid is, undoubtedly, to changed from a fossil fuel base to some alternative sources for the sake of the planet. The two major actors in this scenario are: nuclear and renewable energies [10]. Each of them have its benefits and drawbacks. This chapter aims to provide the reader an introduction on the wind energy industry segment as well as how the technical details studied on this work around nonlinear control and optimization are relevant for helping wind electricity generation to be more efficient and, thus, even more economically attractive. After that, section 1.2 provides some important notation and terminology remarks used throughout the text and, finally, an overview of how the document is organized is presented in section 1.3.

1.1 Wind Energy Electricity Generation

One of the most promising renewable energies sources is the wind power generation. Although taking benefit from the wind power is somehing that dates thousands of years back with the first wind mills, its usage for electricity generation has one of the most important breakthroughs associated to the the oil crisis in 1973, when the USA government has started being involved with wind energy research and development of vertical-axis, horizontal-axis and innovative types of wind turbines [11–15]. As of 2016, Wind Energy Convertion Systems (WECS) have reached 7% of the total global electricity generation capacity [16].

Among all renewable energy technologies used to generate electricity, wind energy is the second one in terms of installed capacity, loosing only for hydro power generation [7], showing that it is a very mature technology. The global installed capacity has been continuously increased each year as shown in figure 1.1. Figure 1.2 shows the current top ten players on the wind energy generation scenario.

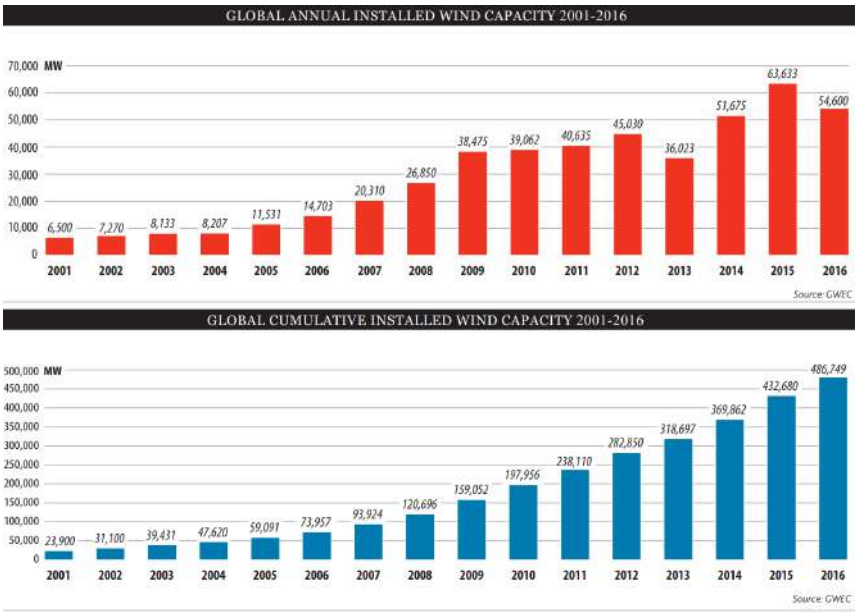

FIGURE 1.1: Global Annual (top) and Cummulative (bottom) Installed Wind Capacity [1]

One might acknowledge that WECS can also have some drawbacks: for instance some studies [17, 18] have shown the increase on the number of bird and bat mortality around wind farms, impacting wildlife, and the increase of noise pollution and visual interference [19]. Although these impacts are extremely important and must be addressed by both academia and industry, this kind of problems are certainly less significant than the environmental impacts caused by hydroelectric power plants or nuclear power plants, which have also the disadvantage of having substantially higher installations costs and construction times. [10]. In addition, the benefits taken from WECS on the reduction of water consumption and environmental pollution [19] still make this type of renewable energy as the most promising one.

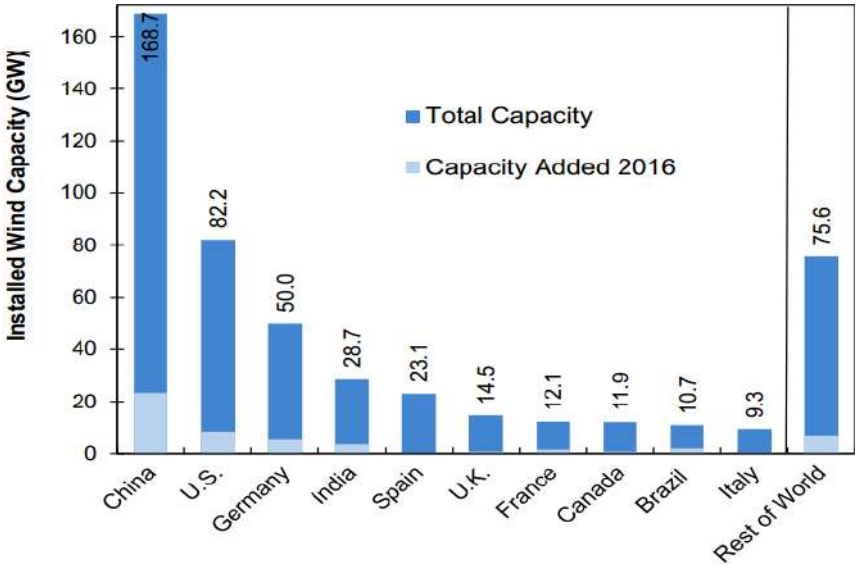

FIGURE 1.2: Top 10 Countries in Global Wind Capacity, 2016 [2]

1.1.1 WECS Techonology

There two main categories of wind turbines: horizontal-axis wind turbines (HAWTs) and vertical-axis wind turbines (VAWTs). However, within these two categories there are several variations as figure 1.3 depicts. The turbines can also vary on the number of rotor blades used, on the ideal wind conditions for operation (i.e. high or low wind speeds), whether or not having a gearbox, generator type (i.e. synchronous, asynchronous or direct current), etc.

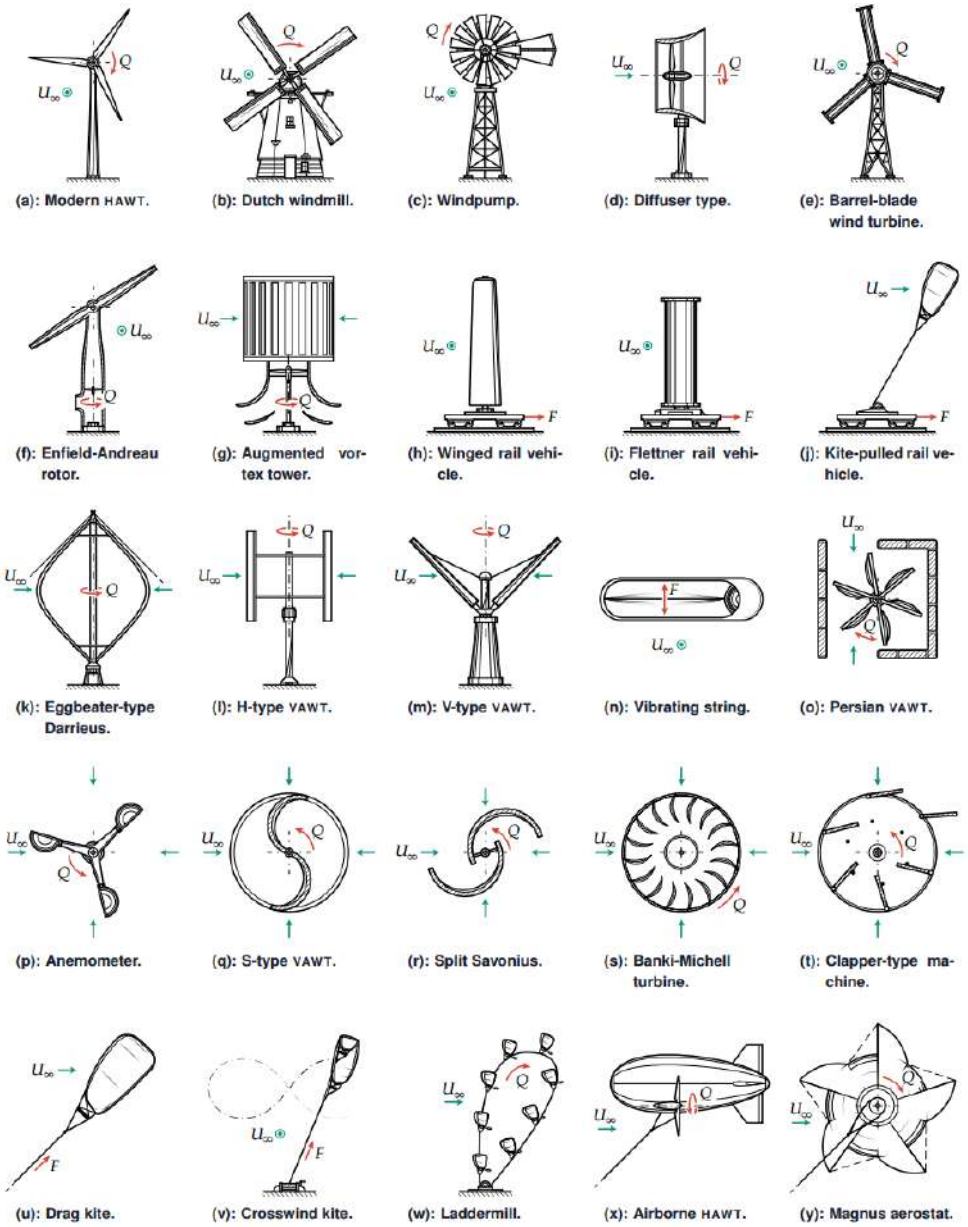

FIGURE 1.3: Different Types of Wind Turbines [3]

Each type of turbine has different aerodynamics characteristics and has advantages when compared to the others. For instance, for urban electricity generation, VAWTs like the Darrieus turbine are preferred due to the fact they can extract more energy from turbulent flows, which is the case around buildings, since they are

capable of generating electricity independently of the wind direction [3].

However, the most usual type is the *(a): Modern HAWT* with three blades sketched in figure 1.3. This kind of turbine is the most commercially available for industrial applications due to hiistorical reasons and to its higher efficiency (greatest power coefficient) for a relatively wide range of the tip speed over wind speed ratio as shown in figure 1.4.

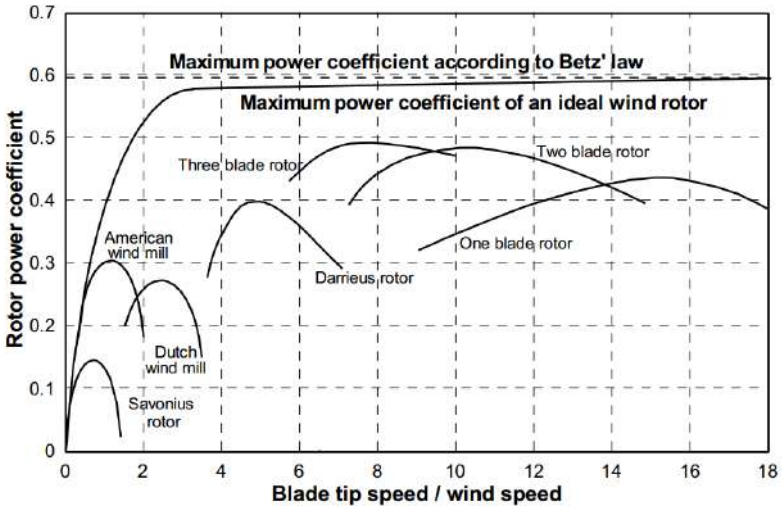

FIGURE 1.4: Power Coefficient of Different Wind Turbines Compared to Betz's Law [4]

Figure 1.4 also shows the difference between the theoretical limit for the power coefficient given by the Betz' law [20, 21] and their values obtained from real tests. This difference is explained due to aerodynamic, mechanical and electrical losses in the assembled system. More details about the power coefficient C_p and the WECS properties are given in Chapter 2. Nevertheless, it is important to mention here that each wind energy converter has a specific characteristic power curve that evidences the dependency of the generated output power on the average wind speed. Although this curve varies from a converter to another, some general operational characteristics can be pointed out looking at a generic power curve as shown in figure 1.5.

Figure 1.5 shows that there are four different regions of operation for a wind energy conversion system:

- Region/Phase I : In this region, the wind speed is lower than the converter minimum speed needed for start-up. For that reason, this speed threshold is called the cut-in wind speed. Thus, in this phase, the electric power output is obviously zero;

- Region/Phase II : This is called the sub-rated region. The wind speed is higher than cut-in wind speed (3-4 m/s), so the converter is running and generating electric energy, and it is below the rated wind speed (12-14m/s).

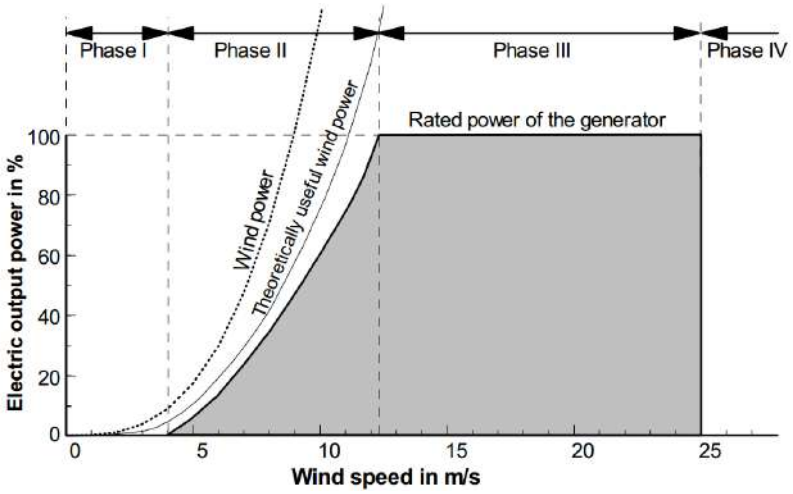

FIGURE 1.5: Typical HAWT Characteristic Power Curve [4]

The *Theoretically useful wind power* curve has a cubic dependency on the wind speed, however, due to losses that are not linear to speed such as aerodynamic friction ones, the dependency is changed from the theoretic relationship when it comes to useful electric power at the generator.

- Region/Phase III: This is called the rated region. At the rated wind speed (12-14 m/s), the generator reaches its capacity, hence, for wind speeds above this value and below the cut-out speed (24-26 m/s), the rotor absorbs more power than the installed nominal generator is designed for, which must be avoided by some control strategy that transfers at most the installed generator capacity to the generator.

- Region/Phase IV: In this region, the wind speed is too high (above the cut-out wind speed) for the installed converter and the WECS structure might be mechanically damaged if operation continues. In that case, the generator is shut down the delivered power is obviously zero.

1.1.2 Control of Wind Systems

For phases II and III, i.e wind speeds above the cut-in and below cut-out, adequate control techniques are necessary so that the all available power on the characteristic power curve is extracted. As previously explained, phase III requires that the delivered power is controlled to avoid rotors deterioration and and to not exceed the generator's thermal limitation. However, once the nominal wind speed is reached, the best thing that can be done is to maintain the generators power constant on its nominal capacity regardless of the wind speed.

There are two main strategies for power control on the rated region: stall and pitch controls, but the second one presents smoother phase transitions and shut-downs [4]. Thus, the most used control strategy is the variable pitch to maintain

the generator power in its maximum nominal capacity for the rated power region. Nonetheless, the main focus of the present work is to deal with power optimization in the sub-rated region (phase II) because, in this phase, there is an optimal value for the tip-speed ratio for each wind speed so that the Maximum Power Point (MPP) can be achieved. Hence, it is not only necessary to control the pitch angle or the rotor speed but also to make these variables follow a desired set-point that maximizes mechanical power extraction for each different wind speed.

Thus, the so-called Maximum Power Point Tracking (MPPT) can be achieved in two steps: solving the control/tracking problem and calculating the optimal/desired reference signal to the tracking problem. In the following, these two steps are discussed in more details. To tackle the tracking problem, there are different ways of manipulating the electric output on a WECS, but, below the rated wind speed, the most efficient way to maintain the optimum power coefficient is to adapt constantly the rotor speed [22]. For the second point, design methods of tracking the maximum power or torque are essential for WECS with variable wind speed [23–25] and present several advantages, such as: improvement of transient performance [25] and model uncertainties [24]. There are mainly three categories of MPPT techniques: tip speed ratio (TSR) control, power signal feedback (PSF) control and hill-climb search (HCS) control [26, 27]. HCS is considered to be flexible and simple in implementation and no wind speed sensors (or observers) nor prior knowledge of the wind turbine's characteristics is required, while TSR and PSF usally rely on both of these variables.

A new trend regarding the control of wind systems is trying to optimize power generation for a whole wind farm. The goal in that case is to control numerous wind turbines simultaneously, taking into account their interaction. An HCS strategy based on Extremum Seeking Control has been developed in [28].

1.1.3 Dissertation Purpose

The objective of this work is to present a fixed pitch-variable speed hierarchical control scheme for the sub-rated region (see figure 1.5) in order to achieve MPPT in WECS. The main idea is to use as an inner loop a Variable Structure Control (VSC) based controller in order to solve the global tracking problem with fast transient response so that the turbine's angular speed error stays within the vicinity of zero for all times. For the outer loop, a real-time non model based algorithm relying on Extremum Seeking Control (ESC) is developed to calculate at each instant the turbine's rotor speed reference signal that maximizes the power or torque. In that way, the ESC outer loop provides this variable set-point to the inner loop, maximizing wind power extraction.

In the literature, many works such as [29–32] rely on wind measurement or estimation to perform MPPT via TSR control. However, as in other works like [33–38], this is an HCS algorithm and has the advantage of not needing any information about the wind speed nor the turbine's power curve. In this work, the MPP is extracted by just knowing that the mechanical power is an unimodal convex function of both wind and turbine rotor speeds as well as some other turbine's parameters. An interesting work is presented in [39], in which the authors, by using the proper change of variables, transform the nonlinear and not convex optimization problem into a linear convex one and then apply economical Model Predictive Control (MPC) to handle both maximization of transferred energy while respecting grid delivered power gradient and other constraints.

1.2 Notation and Terminology

The following notation and basic concepts are employed: **(1)** ISS means Input-to-State-Stable and classes $\mathcal{K}$, $\mathcal{K}_\infty$ functions are defined as in [40]. **(2)** The Euclidean norm of a vector x and the corresponding induced norm of a matrix A are denoted by $|x|$ and $|A|$, respectively. **(3)** The symbol "s" represents either the Laplace variable or the differential operator "d/dt", according to the context. **(4)** As in [41, 42] the output y of a linear time invariant (LTI) system with transfer function $H(s)$ and input u is given by $y = H(s)u$. Convolution operations $h(t)*u(t)$, with $h(t)$ being the impulse response from $H(s)$, will be eventually written, for simplicity, as $H(s) * u$. **(5)** As usual in Sliding Mode Control (SMC), Filippov's definition for solution of discontinuous differential equations is adopted [43]. **(6)** $\pi(t)$ is any exponentially decreasing signal, i.e., a signal satisfying $|\pi(t)| \leq \Pi(t)$, where $\Pi(t) := Re^{-\lambda t}$, $\forall t$, for some scalars $R, \lambda > 0$.

1.3 Document's Organization

This document is organized as follows: First, in order to provide to the reader the necessary contents for understanding the application of the results obtained by this study, an overview of Wind Energy Conversion Systems is provided. Both mechanical and electrical subsystems are presented in details so that a ground basis, necessary for further chapters, is built.

After that, the optimization and control mathematical problem formulation is stated along with all the necessary hypothesis so that the following results are valid. Then, the focus stays on the Smooth Sliding Controller for which new results and extensions in the context of WECS are presented and discussed. In Chapter 4, other VSC-based controllers are presented as they were studied as possible replacements

for the Smooth Sliding Controller. Still in Chapter 4, a variation of the Extremum Seeking Control Algorithm is discussed and its application on WECS is presented in details. Also, the proof of the overall closed-loop stability theorem for WECS is provided.

Once the theoretical foundations are given and the theorems are proven for the studied case, simulation results are presented and discussed for a specific HAWT, proving the benefits of the developed Optimization and Control scheme. Finally, the conclusions about this work are addressed, pointing out the scientific benefits brought by this study as well as some drawbacks and limitations that could be addressed on future work.

Chapter 2

Wind Energy Convertion Systems

This chapter aims to present all WECS's main elements and components. Technical details about wind turbines, generators and conncection to the power grid are provided, followed by an overall scheme for a usual WECS. Finally, the mathematical modellings related to the aerodynamics and the energy conversion System for the type of wind turbine studied in this work are presented as well as some important properties related to electrical and mechanical subsystems. An overview of other contents presented such as Field Oriented Control (FOC) and Modulation Techniques is also given.

2.1 Wind Turbines

A simplified scheme of a three blade rotor HAWT is given in figure 2.1. Even though the concepts of the control strategies developed here are not dependent on the type of the wind turbine, all theoretical results rely on a specific (but usual) mathematical formulation for the aerodynamics, the mechanical and electrical subsystems. Thus, the HAWT shown figure 2.1, which is the most usual in the industry, is the type to be considered on the present work. As figure 2.1 depicts a wind turbine is consisted by a high number of complex subsystems. Three main components can be seen in figure 2.1: the tower, the nacelle and (of course) the rotor blades.

2.1.1 Tower

The tower has the function of absorbing static and dynamic stresses applied to all suspended elements. Their height, which is usually around 80 meters off the ground for modern wind turbines [2], is determined from a calculation based on the rotor blade length (turbine radius). Any length added to this value would be an economic study on the trade-offs between the increased engineering costs and the higher average wind speeds (leading to higher power generation) at this new height

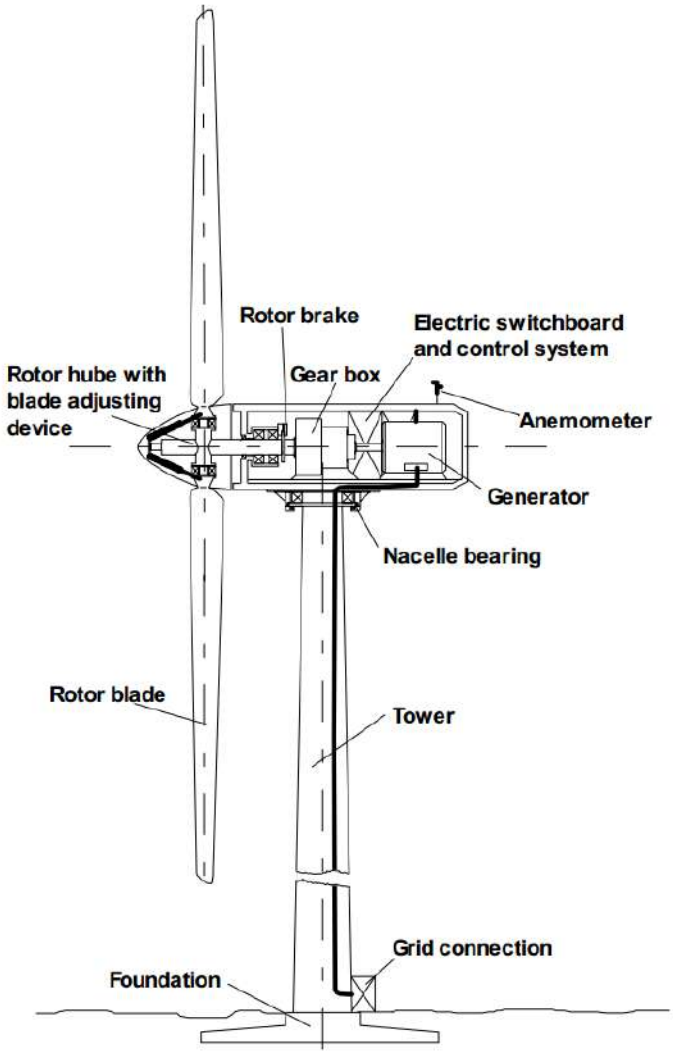

FIGURE 2.1: Three Blade Rotor HAWT Scheme [4]

[4]. Due to technological progress and history, there are many different tower heights present in the industry, varying from 20 meters high towers to more than 100 meters ones [11].

2.1.2 Rotor Blades

In contact with the moving mass, the rotor blades have their shape and size optimized for capturing the greatest possible amount of energy from the wind. However, to do that, it is necessary that the rotor is aligned with the wind direction, which is performed by yaw mechanisms that can control it passive or actively depending on the size of the turbine. This mechanism is usually mounted on top of the tower where a gear wheel drives the rotor to be aligned with the wind direction via mechanical, hydraulic or electromechanical elements [11] . When yaw control is performed actively (most usual case), this mechanism has a dedicated control system that handles all relevant wind direction data coming from the sensors mounted

on the nacelle. In this work, the focus is on the turbine rotor speed control, it is assumed that the adequate yaw mechanisms are in place and that the rotor is always facing the winds coming to the turbine.

Rotor blades adjustment mechanisms are also an important topic due to their impact in power and revolution control on the rated power region, their capability of putting the blades into feathered (no tangential forces applied) pitch position in emergency situations and their ability to provide additional breaking to the already existent brake elements. However, as stated in Chapter 1, the focus of the present work is MPPT during the sub-rated power region, which is more effectively performed by continuous adaptation of the rotor speed. As yaw mechanisms, blade adjustments ones will be assumed to be in place so that the focus of the study is maintained.

2.1.3 Nacelle

The nacelle is a cover housing that enclosures the rotor hube, the braking system, the gearbox, the generator, the electric switch board and control system unit and some wind sensors mounted on its shell. Thus, the energy conversion train takes place inside the nacelle.

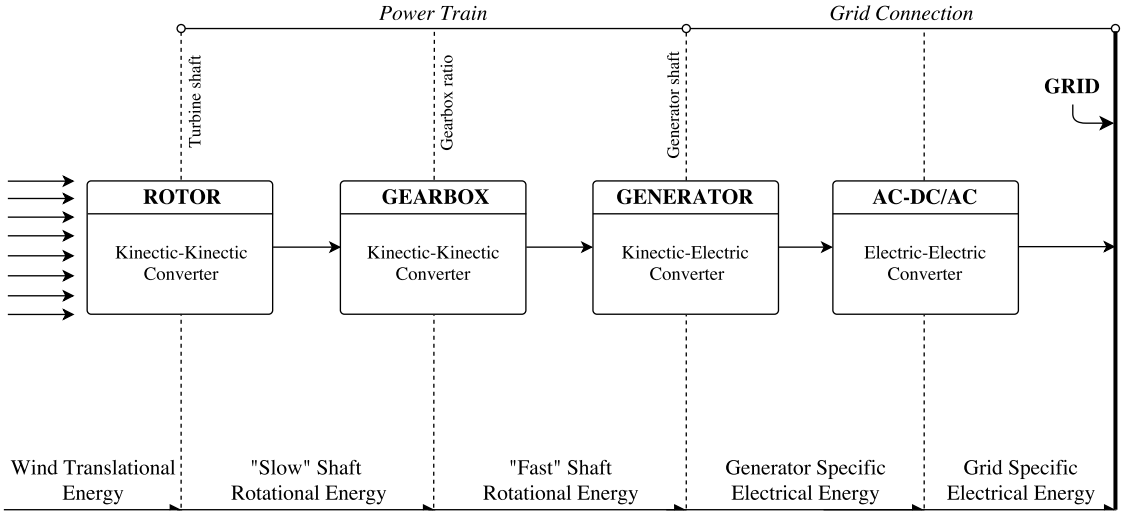

FIGURE 2.2: WECS Energy Conversion Train.

Figure 2.2 describes this process of energy conversion dividing the WECS into multiple stages. First, the rotor blades take the translational kinetic energy coming from the winds and make the rotor turn, transforming this energy into rotational kinetic energy. At this point, the turbine shaft, also called the ”slow” shaft of the power train, is turning. Although there exists gearless wind turbines, usually, the angular speeds on the turbine shaft are not high enough to be directly connected to a generator because its nominal capacity normally require faster speeds. Thus, a gearbox is responsible for increasing that angular speed by a factor equals to its ratio

(n) at the generator shaft, also called the "fast" shaft. Commonly, the gearbox also serves as the main rotor bearing. On its turn, the generator converts the mechanical rotation energy into electrical energy. Generators can be synchronous, asynchronous (induction) or direct current, more details are explored in section 2.2. Finally, the grid connection can be done directly, using AC/AC, AC-DC/DC-AC or DC/AC converters depending on the converter's and generator's type, or indirectly, when the generated electric energy is stored somewhere else or sent to a centralized unit so that it would connect to the power grid in a second moment.

In each part of the energy conversion train, there are losses due to numerous reasons. Aerodynamic losses are present mainly due to non-optimal blade shape, mechanical losses are caused by friction and consequently heat generated at shaft bearings and/or gearboxes and electrical losses might occur at the energy conversion inside the generator, at the subsequent generator-to-power-grid converters or even due to grid power losses. This fact leads to the comments presented in Chapter 1 for figures 1.4 and 1.5 regarding the difference the Betz' law theoretical limits and the actual maximum power coefficients for different types of wind turbines.

In the following sections, electric generators (section 2.2) and grid connection technologies (section 2.3) are discussed in more details.

2.2 Electric Generators and Field Oriented Control

As stated in the latest section, electric generators are one of the key components of the wind energy conversion system. They can be direct current-type, synchronous or induction generators. However, DC generators are rarely used in WECS due to their usual inferior nominal capacity when compared to AC ones. Big DC generators are commonly very expensive and for generating energy to be transmitted to the power grid, the step of DC/AC by means of inverters would still be necessary. Induction generators are usually less expensive, require less maintenance and are more robust than synchronous generators and so they are the preferred type of generator used in the context of WECS.

Concerning the generator-side control techniques, Field Oriented Control (FOC) is a widely known method that allows torque and flux control decoupling on 3-phase electric machines, both synchronous and induction ones. This task is performed by means of two linear operators: Clark and Park transformations, followed by modulation techniques - such as Space Vector Pulse Width Modulation (SVPWM) - to drive the 3-phase AC inverter and control the generator‘s speed, for example. The idea behind FOC is that it is way easier and intuitive to design control laws once taking the important variables to the most adequate reference frame. After this is done, all the complexity that would appear on the initial reference frame will

be handled exclusively by the transformations themselves.

The Clark direct-transformation is responsible for taking the stator currents from the 3-phase (A, B, C) space and project them into the 2-phase (α, β) orthogonal space. The calculations go as follows:

$$\begin{bmatrix} I_\alpha \\ I_\beta \end{bmatrix} = \begin{bmatrix} 1 & 0 & 0 \\ \frac{1}{\sqrt{3}} & \frac{2}{\sqrt{3}} & 0 \end{bmatrix} \begin{bmatrix} i_A \\ i_B \\ i_C \end{bmatrix}, \quad \text{where} \quad i_A + i_B + i_C = 0 \tag{2.1}$$

After Clark's transformation, the currents are rotated into the rotating frame of the generator's rotor, which is the 2-phase (d, q) space. This represents Park's direct transformation, and the rotation matrix is defined as follows:

$$\begin{bmatrix} i_d \\ i_q \end{bmatrix} = \underbrace{\begin{bmatrix} cos(\theta_o) & sin(\theta_o) \\ -sin(\theta_o) & cos(\theta_o) \end{bmatrix}}_{R_{\theta_o}} \begin{bmatrix} I_\alpha \\ I_\beta \end{bmatrix} \tag{2.2}$$

where θ_o is the rotor flux position.

Figure 2.3 shows an schematic representation of Clark and Park transformations and the reference-frame changes.

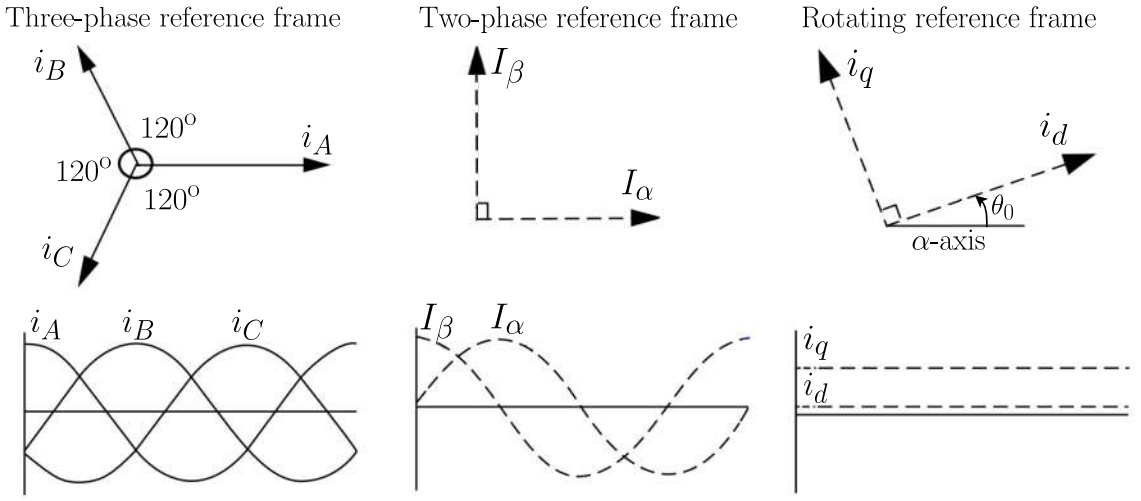

FIGURE 2.3: Clark-Park frame transformations, adapted from [5]

Both Clark and Park transformations have inverses, so the strategy in FOC is to perform the direct transformations using measurements, apply the control algorithm (usually PI) in the rotating rotor frame and then apply inverse transformations back so the appropriate modulation can drive the 3-phase AC inverter. For more details on FOC, please refer to [44].

For the reasons mentioned above, in this study, a Squirrel-Cage Induction Generator (SCIG) is considered, as in [33].

2.3 Power Grid Connection

In the WECS context, there are mainly two types of generator-grid converters if AC electric generators are being used. The first type represent the most traditional ones, called back-to-back converters. They rely on rectifier (AC/DC), storage (DC-link) and inverter (DC/AC) mechanisms in which the storage elements are usually big capacitors.

Matrix converters (MCs) are semiconductor based circuits that allow bidirectional power flow via specific switches organized in a 3-by-3 matrix (for the case of 3-phase input and 3-phase output power transfer). Also, MCs have the capability of having a controlled power factor, do not require big storage elements and can be significantly smaller than usual back-to-back converters. Figure 2.4 shows a typical MC used on WECS for connecting an Induction Generator IG to the power grid.

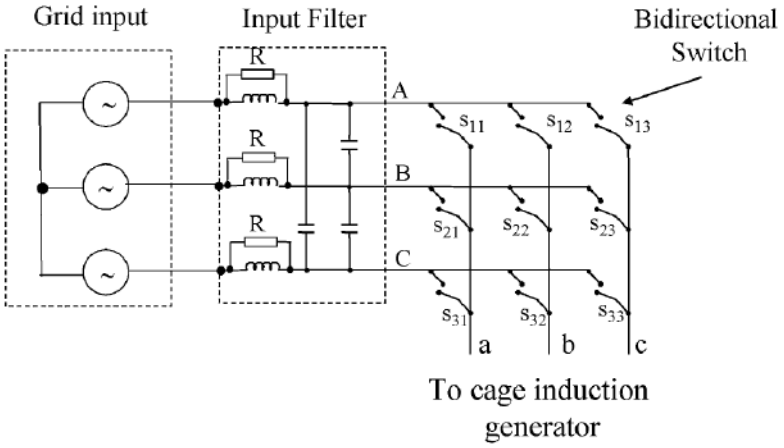

FIGURE 2.4: Matrix Converter usual topology. [6]

A detailed study comparing the various different types of power electronics converters used on wind turbine systems is provided in [45]. In this work, an MC was chosen due to the advantages pointed out in the last paragraphs. The model of the used MC can be found at [33]. It is important to highlight, though, that it is not considered here the modulation techniques to act on the MC. It is considered, however, that the stator electrical frequency and peak amplitude generated at the MC's output are directly available to the controller as it's going to be presented on the following subsections.

2.4 WECS Scheme

After this summary about all main technologies used on WECS, a complete diagram using the most pertinent pieces discussed in the last sections is elaborated for this case study and presented in figure 2.5.

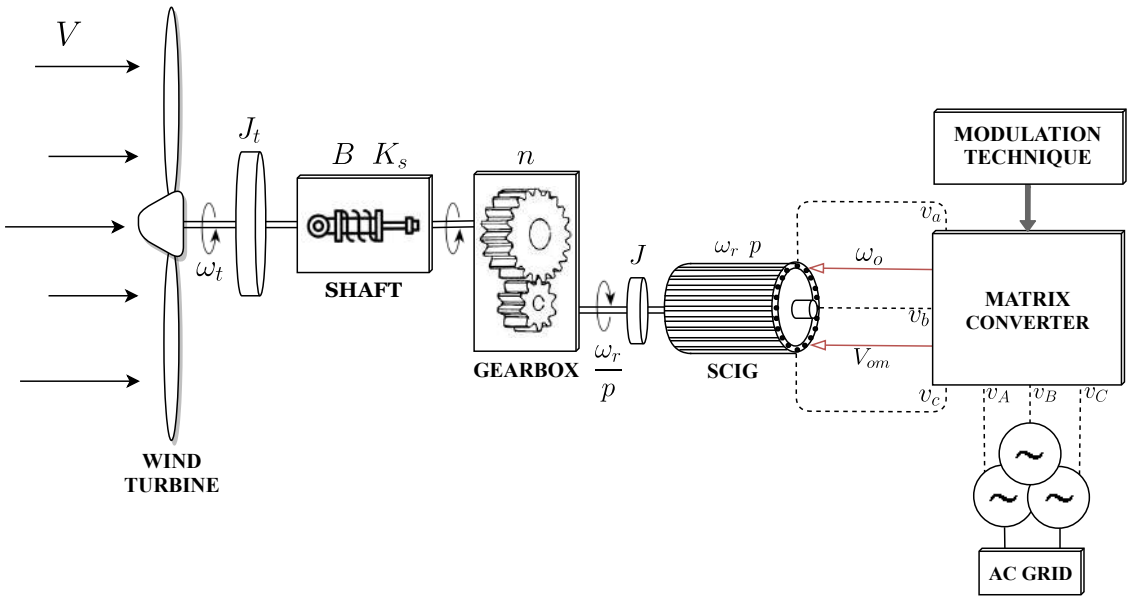

FIGURE 2.5: Detailed WECS scheme

Figure 2.5 shows that a squirrel cage induction generator is used for electricity generation and that an MC is used for AC/AC direct conversion from the generator to the power grid side. The next sections cover almost every aspect of the above diagram with the only exception being the modulation techniques for commuting the bidirectional switches on the MC. This diagram will be referenced throughout the text as it groups into a visual representation all the necessary elements for understanding the modeling, control and optimization parts of the specific WECS studied in the present work.

2.4.1 The Aerodynamics

The wind power available (P_w) on the blade impact area is defined as:

$$P_w := \frac{1}{2}\rho_a S V^3 \,, \tag{2.3}$$

where ρ_a is the air density in kg/m^3, S is the cross-sectional area in m^2, and V is the wind speed in m/s.

The fraction of power effectively extracted from the wind (P_w) by a wind turbine varies with the wind speed V, the rotational speed of the turbine ω_t, and turbine blade parameters, for instance, the angle of attack and pitch angle $\mathcal{B}$, which is assumed zero without loss of generality. The ratio of the turbine tip speed ($R\,\omega_t$) to the wind speed (V), standing for *Tip Speed Ratio* (TSR), is defined as

$$\lambda = \frac{R\,\omega_t}{V} \,, \tag{2.4}$$

where R is the maximum radius (blade length) of the rotating turbine in m and

ω_t is in rad/s.

The actual *mechanical power* output of the turbine P_m is defined as:

$$P_m := C_p P_w \tag{2.5}$$

where C_p is the coefficient of performance or power coefficient, which is in general a function of the blade pitch angle (once again, considered zero), the wind speed V and the rotor speed ω_t. Moreover, P_m can be written as a function of λ, by considering one usual approximation for C_p [46]:

$$C_p(\lambda, 0) := C_1 \left[\frac{1}{\lambda} - C_2\right] e^{-(\frac{C_3}{\lambda} - C_4)}, \tag{2.6}$$

with $C_1 = 0.45/0.003$, $C_2 = 13.635/151$, $C_3 = 20$ and $C_4 = 0.003$. According to Betz's law the theoretical limit of the ratio of the turbine power to the wind power is 0.59, however, in practice, this value varies about 0.20–0.45, [24, 47]. Although the power coefficient curve can only be completely known by tests performed on the actual WECS, including all its subsystems, it has been approximated numerically in several references [24, 46, 47]. Figure 2.6 illustrates the power coefficient C_p in (2.6) with wind speeds varying from 0 to 14 m/s.

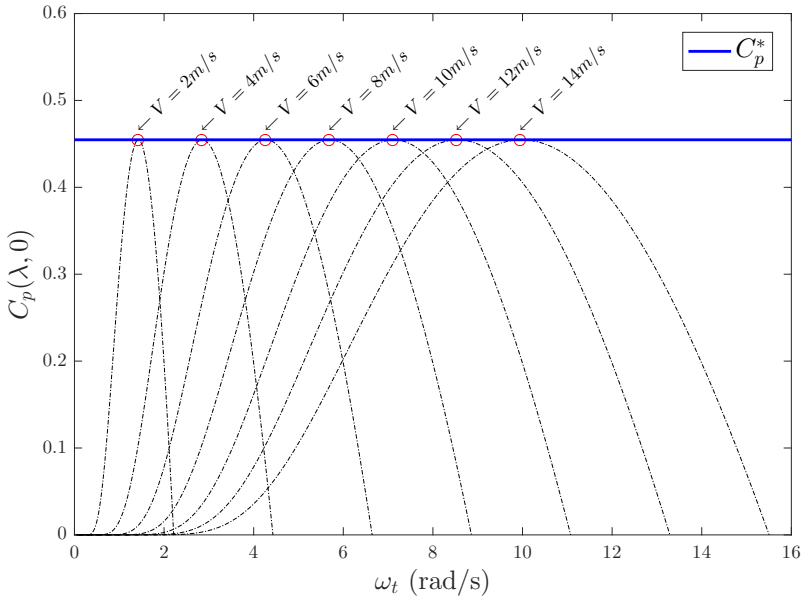

FIGURE 2.6: The power coefficient (2.6) as a function of the angular velocity ω_t for wind velocity varying in the interval $(0, 14]$.

It is interesting to note that for each wind speed, there is a maximum C_p^* given by the maximizer w_t^*. Moreover, taking the definition of P_m given in equation 2.5, one can rewrite it as:

$$P_m = \frac{1}{2}\rho_a S V^3 C_p(\lambda) \tag{2.7}$$

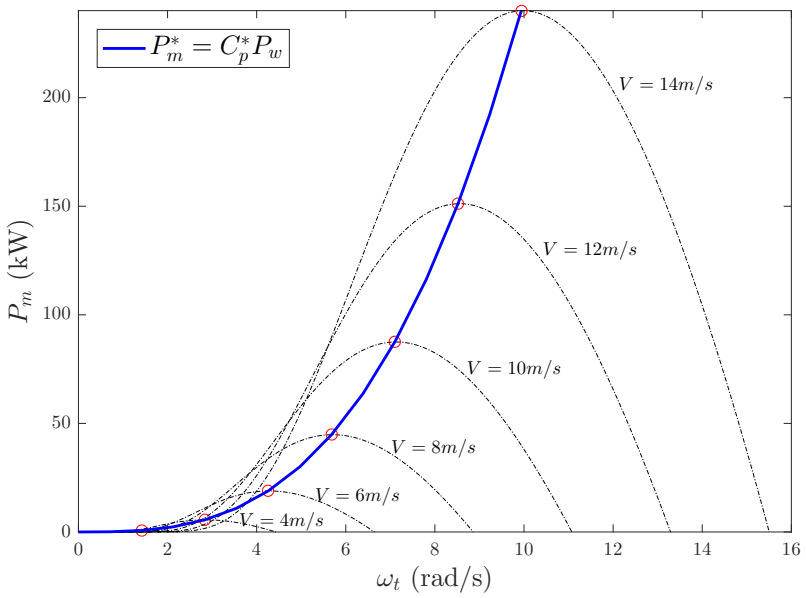

FIGURE 2.7: The mechanical power (2.6) as a function of the turbine's angular speed ω_t for wind speeds varying in the interval $(0, 14]$.

Figure 2.7 shows that for the same set of maximizers w_t^* as the ones achieving C_p^* in figure 2.6, the maximum values of power extracted from wind can be found by polynomial interpolation of the maxima. Thus, a third-order-like curve can be generated and, theoretically, the MPP evolves along this curve. Hence, MPPT, can be viewed as the problem of the tracking this unknown *unknown* function Pm^* or, equivalently C_p^*.

In addition, the *aerodynamic torque* applied to the rotor by the wind is a variable that can be estimated from the dynamic system equations presented in the following subsections. Thus, they can also be used as cost functions to be maximized or as auxiliary variables for estimating the mechanical power when this kind of information is not available via measurements $\left(T_a^V(\omega_t) = P_m/\omega_t\right)$. One might rewrite the aerodynamic torque as:

$$T_a^V = \frac{1}{2}\rho_a S \frac{V^3}{\omega_t} C_p(\lambda) = \frac{1}{2}\rho_a S R V^2 \frac{C_p(\lambda)}{\lambda}\,. \tag{2.8}$$

Figure 2.8 shows that also how the maximum torque varies with the turbine's angular speed. In Chapter 6, it will become clear, however, that maximizing torque does not imply in maximum power and this happens because these two functions have different maximizers ω_t^* for each wind speed.

Hence, to summarize, according to the instantaneous wind speed, it is possible to have different operation points. In other words, the optimum rotor speed is variable for each value of the wind speed. The challenge is how to develop a system capable of calculating automatically this variable set point always maintaining the desired operation.

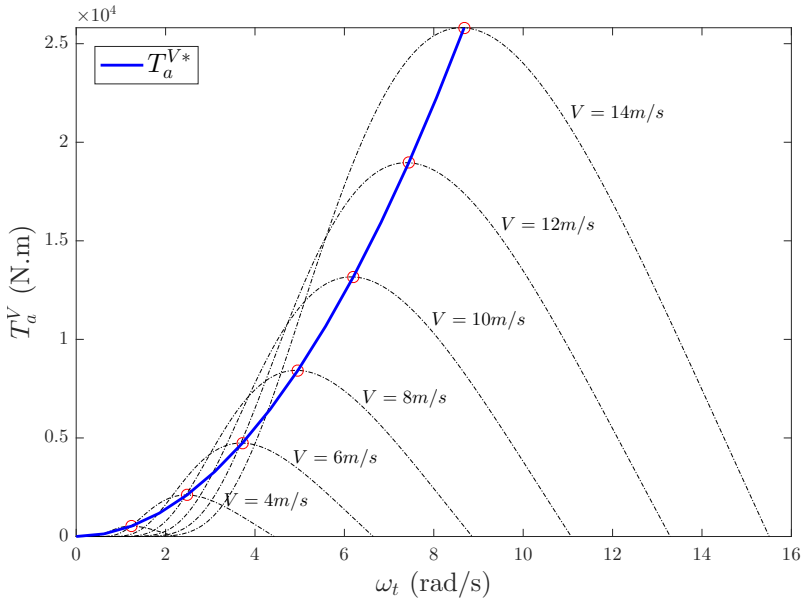

FIGURE 2.8: The aerodynamic torque (2.8) as a function of the angular velocity ω_t for wind velocity varying in the interval $(0, 14]$.

2.4.2 Energy Conversion System

From [33], the post Clark transformation (α, β) model equations for the electrical subsystem considering a SCIG as in 2.5 are given by:

$$\dot{I}_\alpha = -a_0 I_\alpha + a_1 \lambda_\alpha + a_2 \omega_r \lambda_\beta + k_0 \cos(\theta_0)\,, \tag{2.9}$$

$$\dot{I}_\beta = -a_0 I_\beta + a_1 \lambda_\beta - a_2 \omega_r \lambda_\alpha + k_0 \sin(\theta_0)\,, \tag{2.10}$$

$$\dot{\lambda}_\alpha = -a_4 \lambda_\alpha + a_3 I_\alpha - \omega_r \lambda_\beta\,, \tag{2.11}$$

$$\dot{\lambda}_\beta = -a_4 \lambda_\beta + a_3 I_\beta + \omega_r \lambda_\alpha\,, \tag{2.12}$$

where I_α and I_β are the measured stator currents, λ_α and λ_β are the rotor flux linkages (**not available for feedback**) and $\theta_0 = \int_0^t \omega_0(\tau) d\tau$ is the rotor flux position and the output electrical angle of the matrix converter connecting the IG to the power grid, with the electrical frequency of the stator ω_0 being considered as the control signal input satisfying:

$$\dot{\theta}_0 = \omega_0\,. \tag{2.13}$$

The electromagnetic torque generated by the IG can be considered as the output of the electrical subsystem and it is given by:

$$T_e = \frac{3pL_m}{2L_r}(I_\beta \lambda_\alpha - I_\alpha \lambda_\beta)\,, \tag{2.14}$$

where L_m is the mutual inductance, $L_s L_r$ is the rotor inductance and p is the number of pole pairs of the IG.

In (2.9) and (2.10), $k_0 := V_{om}/(L_s - L_m^2/L_r)$ where the terms $V_{om}\cos(\theta_0)$ and $V_{om}\sin(\theta_0)$ are the stator voltage of the (α, β) model, V_{om} being the stator **constant** peak amplitude voltage obtained through the MC output voltage and L_s being the stator inductance. In that sense, considering figure 2.5, as V_{om} is constant, ω_o is the only control signal coming from the MC and going to the IG and it's role is drive the wind turbine speed to it's desired value.

The constants a_0, a_1, a_2, a_3 and a_4 are calculated based on the system parameters as follows:

$$\begin{aligned} \Lambda &= 1 - \frac{L_m^2}{L_r\, L_s} \\ a_0 &= a_2\, a_3 + \frac{R_s}{\Lambda\, L_s} \\ a_1 &= a_2\, a_4 \\ a_2 &= \frac{L_m}{\Lambda\, L_s\, L_r} \\ a_3 &= \frac{L_m\, R_r}{L_r} \\ a_4 &= \frac{R_r}{L_r} \end{aligned} \tag{2.15}$$

where R_r is the rotor electric resistance and R_s is the stator electric resistance.

The mechanical subsystem (the turbine, the shaft and the gearbox) of the wind turbine is modeled as a spring-damper with dynamics given as:

$$\dot{\omega}_r = \frac{p}{J}(T_e - T_L/n)\,, \tag{2.16}$$

$$\dot{\tilde{\theta}} = \omega_t - \omega_r/(pn)\,, \tag{2.17}$$

$$\dot{\omega}_t = \frac{1}{J_t}(T_a^V(\omega_t) - T_L)\,, \tag{2.18}$$

where ω_r/p is the generator rotor angular speed, n is the gearbox ratio, T_a^V is the aerodynamic turbine torque evaluated at a fixed wind velocity V, $\tilde{\theta}$ is the angle shift between the wind turbine angular position and the electrical angle of the rotor of the IG (considering the gearbox), J_t (J) is the turbine (rotor) inertia and

$$T_L = K_s\tilde{\theta} + B(\omega_t - \omega_r/(pn))\,, \tag{2.19}$$

is the load torque created by the spring-damper model, with K_s being the stiffness coefficient of the spring and B is the damping ratio.

2.4.3 WECS Stability Property

The following stability property of the WECS considered in the present work is demonstrated in the this section considering both the electrical and mechanical subsystems of figure 2.5.

Property The WECS dynamics (2.9)–(2.12) and (2.16)–(2.18) is ISS with respect to $|\varepsilon|$, where

$$\varepsilon := \begin{bmatrix} \varepsilon_1 & \varepsilon_2 & \varepsilon_3 & \varepsilon_4 \end{bmatrix}^T = \begin{bmatrix} \omega_t & \dot{\omega}_t & \ddot{\omega}_t & \dddot{\omega}_t \end{bmatrix}^T \tag{2.20}$$

The notion of Input-to-State Stability was first introduced by Eduardo Sontag in 1989 [48]. This concept has been developed since then [49, 50] and it is an extremely important tool in the analysis of nonlinear systems.

Being a generalization of Global Asymptotic Stabily (GAS), ISS's main advantage is that it regroups into a single formulation both Lyapunov Internal Stability and Input-Output Stability, such as bounded-input, bounded-output stability (BIBO), notions.

A system is ISS w.r.t an input u if and only if there exist $\beta \in \mathcal{KL}$ and $\gamma \in \mathcal{K}$ so that, for all initial states x_0 and controls u_t, and all $t \geq 0$:

$$|x(t, x_0, u_t)| \leq \beta(|x_0|, t) + \gamma(||u_t|\,|_\infty) \tag{2.21}$$

Subsections 2.4.3 and 2.4.3 are used as a two-step proof of the above (2.4.3).

Electrical Subsystem

As usual in FOC, consider the transformation of the flux and the stator currents:

$$\begin{bmatrix} \lambda_d \\ \lambda_q \end{bmatrix} := R_{\theta_0} \begin{bmatrix} \lambda_\alpha \\ \lambda_\beta \end{bmatrix} \text{ and } \begin{bmatrix} i_d \\ i_q \end{bmatrix} := R_{\theta_0} \begin{bmatrix} I_\alpha \\ I_\beta \end{bmatrix}, \tag{2.22}$$

with R_{θ_0} given by equation 2.2. Premultiplying the first equation in (2.22) by

$$M := \begin{bmatrix} 0 & 1 \\ -1 & 0 \end{bmatrix} \tag{2.23}$$

one can obtain,

$$\begin{bmatrix} \lambda_q \\ -\lambda_d \end{bmatrix} = M R_{\theta_0} \begin{bmatrix} \lambda_\alpha \\ \lambda_\beta \end{bmatrix}$$

$$\left[\begin{array}{cc} i_d & i_q \end{array}\right]\left[\begin{array}{c} \lambda_q \\ -\lambda_d \end{array}\right] R_{\theta_0}^T M R_{\theta_0}\left[\begin{array}{c} \lambda_\alpha \\ \lambda_\beta \end{array}\right]$$

$$\left[\begin{array}{c} \lambda_q \\ -\lambda_d \end{array}\right] = M R_{\theta_0}\left[\begin{array}{c} \lambda_\alpha \\ \lambda_\beta \end{array}\right]\left[\begin{array}{cc} i_d & i_q \end{array}\right]\left[\begin{array}{c} \lambda_q \\ -\lambda_d \end{array}\right] = \left[\begin{array}{cc} I_\alpha & I_\beta \end{array}\right] R_{\theta_0}^T M R_{\theta_0}\left[\begin{array}{c} \lambda_\alpha \\ \lambda_\beta \end{array}\right]$$

$$\left[\begin{array}{cc} i_d & i_q \end{array}\right]\left[\begin{array}{c} \lambda_q \\ -\lambda_d \end{array}\right] = \left[\begin{array}{cc} I_\alpha & I_\beta \end{array}\right] R_{\theta_0}^T M R_{\theta_0}\left[\begin{array}{c} \lambda_\alpha \\ \lambda_\beta \end{array}\right]$$

By noting that $R_{\theta_0}^T M R_{\theta_0} = M$, one can verify that

$$\zeta_q := I_\beta \lambda_\alpha - I_\alpha \lambda_\beta = -(i_d \lambda_q - i_q \lambda_d)\,. \tag{2.24}$$

Taking time derivatives of (2.22) along the solutions of (2.9)–(2.12), in the new coordinates, the electrical subsystem (2.9)–(2.12) of the WECS is given by

$$\begin{aligned}
\dot{i}_d &= -a_0 i_d + a_1 \lambda_d + a_2 \omega_r \lambda_q + i_q \omega_0 + k_0\,, && (2.25)\\
\dot{i}_q &= -a_0 i_q + a_1 \lambda_q - a_2 \omega_r \lambda_d - i_d \omega_0\,, && (2.26)\\
\dot{\lambda}_d &= -a_4 \lambda_d + a_3 i_d - \omega_r \lambda_q + \lambda_q \omega_0\,, && (2.27)\\
\dot{\lambda}_q &= -a_4 \lambda_q + a_3 i_q + \omega_r \lambda_d - \lambda_d \omega_0\,, && (2.28)
\end{aligned}$$

or, equivalently,

$$\dot{\mathcal{X}} = A(t)\mathcal{X} + B_0\,, \quad A(t) := A_0 + \Delta(t)\,, \tag{2.29}$$

with $B_0 = \left[\begin{array}{cccc} k_0 & 0 & 0 & 0 \end{array}\right]^T$,

$$A_0 := \left[\begin{array}{cc} -a_0\mathcal{I} & a_1\mathcal{I} \\ a_3\mathcal{I} & -a_4\mathcal{I} \end{array}\right], \quad \Delta = \left[\begin{array}{cc} \omega_0 M & a_2\omega_r M \\ 0 & (\omega_0 - \omega_r)M \end{array}\right],$$

where M is in2.23 and $\mathcal{I}$ is the identity matrix of order 2, $\mathcal{X} = \left[\begin{array}{cc} \mathcal{X}_1^T & \mathcal{X}_2^T \end{array}\right]^T$ $\mathcal{X}_1 = \left[\begin{array}{cc} i_d & i_q \end{array}\right]^T$ and $\mathcal{X}_2 = \left[\begin{array}{cc} \lambda_d & \lambda_q \end{array}\right]^T$. Hence, by considering the Lyapunov candidate function

$$V := \mathcal{X}^T \mathcal{X}$$

one has that

$$\dot{V} = \mathcal{X}^T(A_0^T + A_0)\mathcal{X} + \mathcal{X}^T(\Delta^T + \Delta)\mathcal{X} + 2\mathcal{X}^T B_0$$

Due to the skew-symmetric matrices appearing in Δ, one has that

$$\mathcal{X}^T(\Delta^T + \Delta)\mathcal{X} = \mathcal{X}_1^T M \mathcal{X}_2(2a_2\omega_r) = 2a_2\omega_r(i_d\lambda_q - i_q\lambda_d) = -2a_2\zeta_q\omega_r$$

,

where the last equality comes from (2.24). Moreover, the characteristic polynomial of $A_0^T + A_0$ is given by $[s^2 + (a_0 + a_4)s + (a_0a4 - a_1a_3)]^2$ which is a Hurwitz polynomial. Then, one can further write

$$\dot{V} = \mathcal{X}^T(A_0^T + A_0)\mathcal{X} - 2a_2\zeta_q\omega_r\,, \tag{2.30}$$

and conclude that the $\mathcal{X}$-dynamics in (2.29), or the (2.25)–(2.28), is ISS w.r.t. $\zeta_q\omega_r$, for k_0 (or V_{om}) sufficiently small such that the stability margin of $(A_0^T + A_0)$ is not compromised. From (2.22) it is clear that the flux and the stator currents dynamics (2.9)–(2.12) are also ISS w.r.t. $\zeta_q\omega_r$.

Mechanical Subsystem

Consider the mechanical subsystem (2.16)–(2.18). Then, from the definition of T_L in (2.19) and the ω_t-dynamics in (2.18) one has that

$$\frac{B}{J_t}(\varepsilon_1 - \frac{\omega_r}{pn}) \;=\; -\varepsilon_2 - \frac{K_s}{J_t}\tilde{\theta} + \frac{T_a^V(\varepsilon_1)}{J_t}\,. \tag{2.31}$$

Now, from (2.17), the $\tilde{\theta}$-dynamics can be rewritten as

$$\frac{B}{J_t}\dot{\tilde{\theta}} \;=\; -\frac{K_s}{J_t}\tilde{\theta} + \frac{T_a^V(\varepsilon_1)}{J_t} - \varepsilon_2\,, \tag{2.32}$$

from which one assure that the $\tilde{\theta}$-dynamics is ISS w.r.t. $|\varepsilon|$. Consequently, from (2.31) one can conclude that the rotor angular velocity ω_r is a function of ε and $\tilde{\theta}$. Thus, since the $\tilde{\theta}$-dynamics is ISS w.r.t. $|\varepsilon|$ one can further conclude that the ω_r-dynamics (2.16) is also ISS w.r.t. $|\varepsilon|$.

From (2.31) and (2.17), one can obtain:

$$\frac{B}{J_t}(\varepsilon_2 - \frac{\dot{\omega}_r}{pn}) \;=\; -\varepsilon_3 - \frac{K_s}{J_t}(\varepsilon_1 - \frac{\omega_r}{pn}) + \frac{\dot{T}_a^V(\varepsilon_1)}{J_t}\,. \tag{2.33}$$

Therefore, the time derivative of the rotor angular velocity $\dot{\omega}_r$ can be obtained as a function of ε and ω_r. Now, from (2.16), the electromagnetic torque T_e is given by

the following function of $\dot{\omega}_r$, ε and $\tilde{\theta}$:

$$T_e \;=\; \frac{J}{p}\dot{\omega}_r + \frac{T_L}{n} = \frac{J}{p}\dot{\omega}_r + \frac{K_s}{n}\tilde{\theta} + \frac{B}{n}(\varepsilon_1 - \frac{\omega_r}{pn})\,. \tag{2.34}$$

where the expression of T_L in (2.19) was used. From (2.14) one can additionally conclude that ζ_q in (2.24) is also a function of $\dot{\omega}_r$, ε and $\tilde{\theta}$.

Since $\tilde{\theta}$-dynamics is ISS w.r.t. $|\varepsilon|$ and the flux and the stator currents dynamics (2.9)–(2.12) are also ISS w.r.t. $\zeta_q\omega_r$, according to (2.30), one can finally conclude that all the WESC dynamics is ISS w.r.t. $|\varepsilon|$. ∎

Chapter 3

Problem Formulation

In this chapter, at first, a generic class of nonlinear plants is studied so that the further developments on the chapter could be as much generic as possible. Thus, the global practical tracking and the real-time input-output optimization problems are formulated in a generic fashion as well as the proposed optimization and control strategy. Once these problems are formulated and the strategy is defined, their application into the WECS MPPT problem is addressed since the WECS dynamics are a particular case of the generic nonlinear plant exposed. Finally, the key ideas and a scheme of the proposed control strategy are presented so that each individual control element could be analyzed in Chapter 4.

3.1 Generic Nonlinear Plant Dynamics

Consider the set of SISO nonlinear systems of the form:

$$\dot{x} = f(x,t) + g(x,t)u_s\,, \tag{3.1}$$

$$y_s = h(x,t)\,, \tag{3.2}$$

$$y = \Phi(y_s) \tag{3.3}$$

where $u_s \in \mathbb{R}$ is the control input (discontinuous), $x \in \mathbb{R}^n$ is the state, $y_s \in \mathbb{R}$ is the measured output, $y \in \mathbb{R}$ is a performance function output and the uncertain functions $f(\cdot,\cdot) : \mathbb{R}^n \to \mathbb{R}^n$, $g(\cdot,\cdot) : \mathbb{R}^n \to \mathbb{R}^n$, $h(\cdot,\cdot) : \mathbb{R}^n \to \mathbb{R}$ and the mapping $\Phi(\cdot) : \mathbb{R} \to \mathbb{R}$ are smooth enough to ensure local existence and uniqueness of the solution through every initial condition (x_0, t_0). For each solution of (3.1) there exists a maximal time interval of definition given by $[0, t_M)$, where t_M may be finite or infinite. Hence, *a priori*, finite-time escape can be considered.

Filippov's definition for discontinuous right-hand side differential equations is adopted [43] and the *extended equivalent control*, in which this concept is also valid during the reaching phase, is used. The equivalent control signal is assumed to be

piecewise continuous and is denoted by $u_s(t)$.

In the following, consider u_s as the plant input and y_s as the plant output, where the underscored s stands for *smooth* due to the nature of the proposed VSC-based controller.

3.1.1 Global Practical Tracking Problem

The goal in *Global Practical Tracking* is to find an output feedback dynamic control law u_s to drive the *output tracking error*, defined as:

$$e(t) = y_s(t) - y_m(t) \tag{3.4}$$

exponentially to zero or to some small neighborhood of zero (practical tracking), starting from any plant/controller initial conditions and maintaining uniform closed-loop signal boundedness, in spite of the uncertainties. Usually, The *desired trajectory* $y_m(t)$ is assumed to be generated by the following *reference model*:

$$\dot{\varsigma}_m = A_m\varsigma_m + B_{n^*}k_m r\,, \quad A_m = A_{n^*} + B_{n^*}K_m\,, \tag{3.5}$$

where

$$\varsigma_m := [\ y_m \quad \dot{y}_m \quad \dots \quad y_m^{(n^*-1)}\ ]^T,$$

$k_m > 0$ is constant, $K_m \in \mathbb{R}^{1\times n^*}$ is such that A_m is Hurwitz and $r(t)$ is assumed piecewise continuous and $\boldsymbol{\mathcal{UB}}$.

In the case that the desired trajectory is given by an external controller or optimization algorithm, $y_m(t)$ is assumed to have the same properties as $r(t)$, i.e. piecewise continuous and uniformly norm bounded.

3.1.2 Real-Time Input-Output Opmization Problem

Consider the SISO uncertain static input-output map $\Phi : \mathbb{R} \to \mathbb{R}$ given by (3.3), which is rewritten here for simplicity:

$$y = \Phi(y_s)\,,$$

with $y \in \mathbb{R}$ being a specific performance function output and $y_s \in \mathbb{R}$ being the measured output depending dinamically on both the state $x \in \mathbb{R}^n$ and the control input $u_s \in \mathbb{R}$.

The nonlinear function Φ is assumed locally Lipschitz continuous in y_s and sufficiently smooth (all required derivatives are continuous) so that existence and forward uniqueness of solutions can be assured. It is worth mentioning that for (3.1) and (3.2) these Lipschitz and smoothness assumptions also hold. As previously stated,

for each solution of (3.1)–(3.3), there exists a maximal time interval of definition given by $[0, t_M)$, where t_M may be finite or infinite.

Without loss of generality, it is possible to deal with real-time optimization regarding the maximum seeking problem of (3.3) under the dynamical restriction given in (3.1)–(3.2). All plant parameters are uncertain belonging to a compact set defined by Ω. Hence, the maximum seeking problem can be stated as follows:

(I) *Extremum Points:* Suppose that the function Φ define a nonempty set of maximizers, denoted by

$$\Theta^* := \{\theta \in \mathbb{R} \,|\Phi(\alpha) \leq \Phi(\theta)\,, \forall \alpha \in \mathbb{R}\}\,,$$

It is said that $y^* = \Phi(y_s^*)$ is an extremum (maximum) of the smooth mapping $\Phi(\cdot)$ when $y_s^* \in \Theta^*$. Moreover, y_s^* is said to be a maximizing point of $y(\cdot)$ when y_s^* is as close as possible of the set Θ^* and $y^* = \Phi(y_s^*)$ is said to be an extremum (maximum) of the smooth mapping $\Phi(\cdot)$ when $y_s^* \in \Theta^*$. In addition, as the SISO case is considered, it is supposed to exist a unique maximizing $\theta_j^\dagger \in \mathbb{R}$ for the function $y = \Phi(y_s)$ such that $y^\dagger = \Phi(\theta^\dagger)$ is the extremum (maximum) of the smooth function $\Phi : \mathbb{R} \to \mathbb{R}$. In other words, in Ω, the mapping function $\Phi(\cdot)$ is unimodal w.r.t. y_s, *i.e.*, when $y_s = \theta$ is a constant, there exists a unique $\theta^* \in \mathbb{R}$ such that:

$$\left.\frac{\partial \Phi}{\partial y_s}\right|_{y_s=\theta^*} = 0 \quad \text{and} \quad \left.\frac{\partial^2 \Phi}{\partial y_s^2}\right|_{y_s=\theta^*} < 0\,.$$

(II) *Parametric Uncertainties:* Θ^*, y_s^*, $\Phi(\cdot)$ and its gradient are assumed to be unknown to the control designer. In Ω, for any given $\Delta > 0$ and $y_s = \theta$ being a constant, there exists a constant $L(\Delta) > 0$ such that

$$L \leq \left|\left.\frac{\partial \Phi}{\partial y_s}\right|_{y_s=\theta}\right|, \quad \forall \theta \notin \mathcal{D}_{\Delta_j}$$

where $\mathcal{D}_{\Delta_j} := \{\theta : \ |\theta - \theta^*| < \frac{\Delta}{2}\}$ is called Δ-vicinity of θ^* and Δ can be made arbitrary small by allowing a smaller L. .

(III) *Optimization Objective*: It is necessary to find an output-feedback control law y_m such that, from any initial condition $x(0)$, the state vector $x(t)$ is positioned, as close as possible, within the set Θ^* of maximizers. Hence, the system (3.1)–(3.3) is driven to reach an extremum point and remain close to it thereafter.

3.2 Optimization & Control Strategy

Considering the plant dymamics given by (3.1)–(3.3) and Sections 3.1.1 and 3.1.2, the proposed solution relies on the implementation of two control loops: an inner loop to deal with the *Practical Tracking Problem* (section 3.1.1) and an outer loop to handle the *Optimization Problem* (section 3.1.2) adjusting the reference signal provided to the inner control loop.

Inner Control Loop By using a robust controller based on Variable Structure Control, an inner loop is formed in order to guarantee stability and to assure that the measured output y_s tracks a desired reference signal y_m, in the presence of the uncertainties of $f(\cdot)$, $g(\cdot)$ and $h(\cdot)$. The VSC-based controller will be presented in details as well as its stability properties in Chapter 4. This will be necessary to demonstrate the global stability theorem discussed in Chapter 5. Thus, it will be clear that this robust inner control loop is able to assure that y_s is given by

$$y_s = y_m + e, \quad \text{with} \quad \mu_i := e \tag{3.6}$$

where e is the tracking error which converges to a residual set. Hence, there exists $t_i \geq 0$ such that

$$y_s(t) \approx y_m(t)\,, \quad \forall t \geq t_i \tag{3.7}$$

Outer Control Loop Let $\Phi(y_s)$ be a function also depending on the derivatives of y_s. In some cases, it can be assumed that these derivatives are actually measured. For instance, if y_s represents the shaft position of a DC motor, it is not unusual having access to both speed and acceleration measurements via tacometers and accelorometers for example. However, supposing that only y_s is known, its derivatives could be calculated using the so called "dirty-derivative". For that purpose, consider the following example of generic input-output mapping:

$$y := \hat{\Phi}(y_s) := (K_0 + K_1\psi + K_2\psi^2 + \cdots + K_n\psi^n)y_s + K_{n+1}\,, \tag{3.8}$$

$$\psi(s) := \frac{s}{\tau_o s + 1}\,, \tag{3.9}$$

The factors $K_0, K_1, K_2, \cdots, K_{n+1}$ are assumed to be known but presenting bounded uncertainties. τ_o is a positive design constant and (3.9) the transfer function capable of extracting the "dirty-derivative" of its input. It is clear that, by considering that all necessary derivatives are measured it is equivalent to set $\tau_o = 0$, i.e., $\zeta y_s = \dot{y}_s$. In this case, y is exactly given by $y = \Phi(y_s)$. When $\tau_o \neq 0$, consider the estimation errors $e_o^k := \overset{(k)}{y_s} - \psi^k y_s,\ k = 1, 2, \cdots, n$. Moreover, y is given by

$$y = \Phi(y_s) - \sum_{k=1}^{n} K_k \, e_o^k, \;\; \text{with} \;\; \mu_o := -\sum_{k=1}^{n} K_k \, e_o^k \tag{3.10}$$

Later on will be clear that each estimation error e_o^k converges to a residual if the correspondent $\overset{(k+1)}{y_s}$ is uniformly norm bounded ($\boldsymbol{\mathcal{UB}}$), which will be verified. Therefore, in these circumstances, there exists $t_o \geq 0$ such that

$$y(t) \approx \Phi(y_s)\,, \quad \forall t \geq t_o \tag{3.11}$$

If the inner loop is designed properly, the robust control strategy assures that the output y_s approximately tracks the reference signal y_m as stated in 3.7. In addition, if the auxiliary output signal y is in fact a suitable estimate for the input-output mapping Φ as stated in 3.11, then one has that the corresponding auxiliary plant output approximately given by

$$y(t) \approx \Phi(y_m(t))\,, \forall t \geq \max\{t_i, t_o\}\,, \tag{3.12}$$

which can also be written like

$$y(t) = \Phi(y_m(t) + \mu_i(t)) + \mu_o(t)\,, \quad \forall t \geq 0\,, \tag{3.13}$$

where μ_o is the output error due the imperfections on the estimation of the output mapping $\Phi(\cdot)$. By recalling (3.4), it is evident that $y_s = y_m + \mu_i$, where $\mu_i := e$ is the tracking error in the inner control loop. Thus, μ_i is viewed as an input disturbance and μ_o as an output disturbance. Finally, considering the assumptions about all the functions and mappings, equations (3.1)-(3.3) are rewritten here in order to illustrate the complete class of non-linear SISO plants that are considered in this work.

$$\begin{aligned} \dot{x} &= f(x(t), t) + g(x(t), t) u_s(t)\,, \\ y_s &= h(x(t), t)\,, \\ y &= \Phi(y_m(t) + \mu_i(t)) + \mu_o(t)\,, \quad \forall t \geq 0 \end{aligned} \tag{3.14}$$

3.3 WECS Problem Formulation

The wind turbine dynamics is given by the class of nonlinear uncertain SISO plant given by (2.9)–(2.13) and (2.16)–(2.18) with state vector

$$x := \left[\begin{array}{cccccccc} I_\alpha & I_\beta & \lambda_\alpha & \lambda_\beta & \theta_0 & \omega_r & \tilde{\theta} & \omega_t \end{array} \right]^T , \tag{3.15}$$

and control input ω_0 in (2.13).

Considering both (α, β) (2.9)–(2.13) and (d, q) (2.25)–(2.28) representations, the WECS dynamics takes the form of (3.14) with affine control input $u_s = \omega_0$. Particularly for (2.9)–(2.13), one has that

$$f = \begin{bmatrix} -a_0 x_1 + a_1 x_3 + a_2 x_6 x_4 + k_0 \cos(x_5) \\ a_0 x_2 + a_1 x_4 - a_2 x_6 x_3 + k_0 \sin(x_5) \\ -a_4 x_3 + a_3 x_1 - x_6 x_4 \\ -a_4 x_4 + a_3 x_2 + x_6 x_3 \\ 0 \\ \frac{3p^2 L_m}{2JL_r}(x_2 x_3 - x_1 x_4) - \frac{K_s p}{J} x_7 - \frac{Bp}{Jn}\left(x_8 - \frac{x_6}{pn}\right) \\ x_8 - \frac{x_6}{pn} \\ \frac{1}{J_t}(T_a^V(x_8) - T_L) \end{bmatrix}, \quad g = \begin{bmatrix} 0 \\ 0 \\ 0 \\ 0 \\ 1 \\ 0 \\ 0 \\ 0 \end{bmatrix}$$

As in FOC, it is assumed that $I_\alpha, I_\beta, \omega_r$ are available for feedback, while the flux are not available, so that it is not required to install flux sensing coils (or Hall effect sensors) in the stator nor the usage of state observers. The measured output is chosen as

$$y_s = \underbrace{[0 \;\; 0 \;\; 0 \;\; 0 \;\; 0 \;\; 0 \;\; 0 \;\; 1]}_{h} x = \omega_t$$

It is assumed here that the cost function Φ can be either the aerodynamic torque (T_a^V) or the mechanical power (P_m). Hence,

$$y = \Phi(w_t) := T_a^V(\omega_t) \;\text{ or }\; y = \Phi(w_t) := P_m(\omega_t) = \omega_t T_a^V(\omega_t) \tag{3.16}$$

In both cases, in order to assure existence and forward uniqueness of solutions, it is assumed that the nonlinear functions T_a^V in (2.8) and P_m in (2.7) are locally Lipschitz continuous in ω_t and sufficiently smooth (all required derivatives are continuous). For each fixed wind speed V within the sub-rated power region, the following assumptions are considered:

(Φ.I) Both the aerodynamic torque $T_a^V(\cdot)$ and the mechanical power $P_m(\cdot)$ are unimodal functions with their respective maximizers θ_T^{V*} and θ_P^{V*}.

(Φ.II) There exists a positive constant $\bar{c}$ such that $0 \leq |\Phi(\omega_t)| < \bar{c}$ and, for any given $\underline{c} > 0$, there exists $\bar{\theta}_c > 0$ such that $\underline{c} > \left|T_a^V(\omega_t)\right|$ or $\underline{c} > |P_m(\omega_t)|$, for $|\omega_t| \geq \bar{\theta}_c$.

According to Section 2.4.1, it is clear that assumption **(Φ.I)** is not restrictive, since both functions are typically given by selecting one of the most common equations used for the non-dimensional power coefficient as (2.6).

The function $\Phi(\omega_t)$ is regarded as an uncertain (unknown) and smooth cost function. According to first assumption, it is considered that there exists a unique *unknown* point θ_*^V such that $\Phi(\theta_*^V)$ is the maximum of Φ, whose gradient is unknown for the control designer.

The *control objective* is real-time optimization, *i.e.*, maximization[1] of $\Phi(\cdot)$ under (2.9)–(2.12), (2.13) and (2.16)–(2.18). The goal is to find an output-feedback control law $y_m = \omega_t^*$ so that, for any initial conditions, the system is steered to reach the extremum point and remain on such point thereafter, as close as possible.

From f one can see that this system is non-linear on its state x and affine on its control input u. Although it is not a highly non-linear system, there are multiplicative interaction between states and sinusoidal interactions on the control signal's integral $x_5 = \theta_0$. Thus, even if the open loop system is ISS w.r.t the wind turbine speed and its derivatives, classical control strategies might not be enough to guarantee a fast transient while chasing maximum power point tracking and a non-linear control strategy will be considered.

3.4 Key Ideas

As proposed in section 3.2 the solution relies on the implementation of two nested control loops.

On the **inner loop** a robust sliding mode control (SMC) which produces smooth control action, named *Smooth Sliding Control (SSC)* is used in order to assure global practical tracking. The MC electrical frequency of the stator is given by $\omega_0 = u_s$, where u_s is the SSC law that assures that $y_s = \omega_t = y_m + e$, where the tracking error e is the input disturbance μ_i and , as will be proved later on, converges to a residual set. Hence, equation (3.7) hols.

$$\omega_t(t) \approx y_m(t)\,, \quad \forall t \geq t_i\,.$$

For the **outer loop**, first, an *Auxiliary Output* is defined for *Estimating the Cost Function* $\Phi(w_t)$. From (2.18), one has that $T_a^V(\omega_t) = J_t\dot{\omega}_t + T_L$, with T_L in (2.19). By assuming J_t, K_s, B, p and n as known (but uncertain) constants and ω_t, ω_r are available for feedback, then one can define the following auxiliary output as one possible estimate for the aerodynamic torque:

$$y := \hat{T}_a^V := J_t\zeta + T_L\,, \tag{3.17}$$

$$\zeta := \frac{s}{\tau_o s + 1}\omega, \tag{3.18}$$

[1]Without loss of generality, only the maximum seeking problem is addressed.

where τ_o is a positive design constant as stated on the previous section. It is clear that, by considering that an accelerometer is available one can set $\tau_o = 0$, i.e., $\zeta = \dot{\omega}_t$. In this case, y is exactly given by $y = T_a^V(\omega_t)$. When $\tau_o \neq 0$, consider the estimation error $e_o := \dot{\omega}_t - \zeta$. Moreover, y is given by $y = T_a^V(\omega_t) - J_t e_o$. If the mechanical power is estimated through $P_m := \omega_t T_a^V$ using the aerodynamic torque estimate in 3.17, one has that $y := P_m(w_t) - \omega_t\,(J_t e_o)$. Thus, the output error μ_o is given either by $\mu_o = -J_t e_o$ or $\mu_o = -\omega_t J_t e_o$.

Later on will be clear that this estimation error e_o converges to a residual set since it will be verified that $\ddot{\omega}_t$ is uniformly norm bounded. As it will be clear that ω_t is also $\mathcal{UB}$, both choices of $\Phi(\cdot)$ would imply into limited output errors e_o. Therefore, equation (3.13) holds and

$$y(t) \approx T_a^V(\omega_t(t)) \;\text{ or }\; y(t) \approx P_m(\omega_t(t))\,, \quad \forall t \geq t_o\,, \tag{3.19}$$

for τ_o sufficiently small. If the inner loop is designed properly, the SSC strategy assures that the rotor angular velocity approximately tracks the reference signal y_m and if the auxiliary output signal is in fact a suitable estimate for the aerodynamic torque or mechanical power, then one has that the corresponding auxiliary plant output is approximately given by

$$y(t) \approx \Phi(y_m(t)) := T_a^V(y_m(t)) \;\text{ or }\; P_m(y_m(t))\,, \forall t \geq \max\{t_i, t_o\}\,, \tag{3.20}$$

Hence, by using an ESC scheme it is possible to drive y_m, consequently the turbine speed ω_t, to the maximizer, for any wind velocity V, with y_m being the ESC signal [51].

Thus, the actual **input-output** relationship is given by (3.13), where y_m is the ESC law, $\Phi(\cdot)$ is the *static input-output mapping*, $\mu_i := e$ stands for the *input disturbance* due to the inner control loop tracking error while $\mu_o := -J_t e_0$ or $\mu_o := -\omega_t J_t e_0$ stands for the *output disturbance* due to the "dirty derivative" estimation error.

One could also think about choosing directly $\Phi(.) = C_p(\lambda)$, however, differently from torque and power which can both be estimated by means of the dynamic equations 2.10-2.19, C_p can only estimated from 2.6. Thus, this implies both the knowledge of the parameters $C_i, i \in [1, 4]$ and a measurement or estimate of the wind speed, which is not the focus of the present HCS control strategy.

It is usual to consider, though, that the turbine pass thought several aerodynamic tests from which J_t, B and K_s can be obtained. The inertia J_t is obtained during the mechanical design while B is usually obtained by computing the difference between the mechanical power and the electrical power [47]. However, uncertainties in K_s

(and B) can be incorporated in the output disturbance μ_o and can be made small since $\tilde{\theta}$ tends to zero, as shown in Chapter 4.

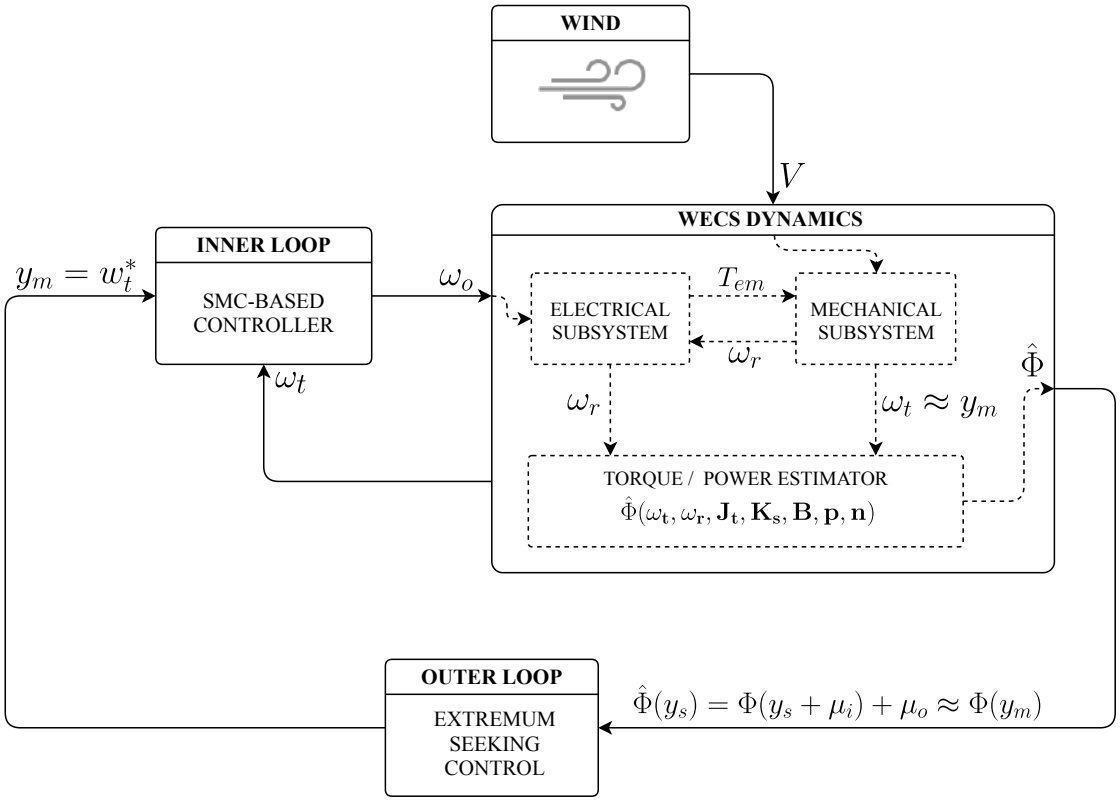

FIGURE 3.1: Control Scheme for WECS' MPPT.

On the other hand, this estimation approach encompasses the case when there is access to turbine power measurements, so that the turbine power and the aerodynamic torque are available for feedback. Thus, in this case, one can set $\mu_o := 0$ in (3.13) and choose:

$$y := P_m(\omega_t) \quad \text{or} \quad y := T_a^V(\omega_t) = \frac{P_m(\omega_t)}{\omega_t}$$

Hence, $y := \Phi(y_m(t) + \mu_i(t))$ with $\Phi(\cdot) = P_m(\cdot)$ or $\Phi(\cdot) = T_a^V(\cdot)$.

Finally, after presenting all these scenarios, assumptions and implications, the overall control scheme with the two nested control loops is given in figure 3.1. This control scheme summarizes the role of each part of the proposed strategy (inner loop, outer loop and estimation algorithm) and also shows how wind speed affects both the dynamics and, consequently, the cost function $\Phi(\cdot)$. Along with the WECS scheme (figure 2.5), these two schematics provide a visual representation of the control and optimization strategy developed for the WECS considered in this work.

Chapter 4

Control and Optimization

In this chapter, both the global practical tracking problem for the inner loop of the WECS dynamics and the real-time input-output optimization problem for the outer loop of the proposed scheme are addressed. First, the usage of a Smooth Slide Controller based on Variable Structure Control at the inner loop is analyzed and some important properties and results are demonstrated. Finally, a Extremum Seeking Control algorithm is studied to accomplish Maximum Power Point Tracking of the WECS and its properties and important results are also highlighted and demonstrated.

4.1 Smooth Sliding Control

In this section, a smooth sliding control (SSC) based on variable structure control (VSC) is considered [52]. In contrast to conventional VSC, this strategy has a smooth control signal.

The challenge of this technique is to overcome the implementation difficulties regarding VSC. Variable structure controllers have a well-known undesirable phenomenon, named *chattering*, induced by non-idealities like small delays or unmodeled plant dynamics. The *SSC* is a version of the Variable Structure Model Reference Control (VS-MRAC) based on the framework of the conventional Model Reference Adaptive Control (MRAC).

4.1.1 SSC and the WECS Tracking Problem

Consider the class of SISO non-linear plants provided on (3.1)–(3.2):

$$\dot{x} = f(x,t) + g(x,t)u_s$$
$$y_s = h(x,t)$$

The *SSC* in [52] was generalized for linear plants with arbitrary relative degree in [53, 54]. However, as bibliography research indicated, the present study appears to be the first work which considers the applicability of the SSC to the class of non-linear plants considered here.

The main idea in sliding mode control is to close the loop of the sliding variable (usually the tracking error) with a relay, having an appropriate modulation function. If the relative degree of the sliding variable ($\tilde{\sigma}$) is unitary[1], an ideal sliding loop is formed around the switching function and, consequently, the sliding variable tends exponentially or in finite time to zero.

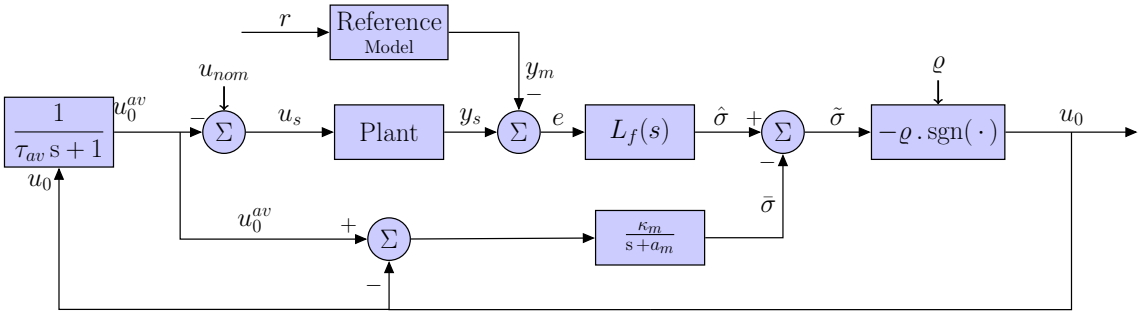

FIGURE 4.1: Topology of the *Smooth Sliding Control* (SSC) for an arbritary relative degree ($n^* \geq 1$).

Recalling the output tracking error defined in 3.4

$$e(t) := y_s(t) - y_m(t)\,,$$

where y_m is the reference signal, which is a uniformly bounded signal by construction. Let n^* be the relative degree from the SSC signal u_s to the output tracking error e. When $n^* = 1$, the output tracking error can be directly used to define the sliding variable. However, when $n^* > 1$, it is considered a linear (non-causal) operator $L(s) = s^{n^*-1} + l_1 s^{n^*-2} + \ldots + l_{n^*-1}$ (Hurwitz polynomial), such that the *ideal output variable* defined as

$$\sigma(t) := L(s)e(t)\,, \tag{4.1}$$

has relative degree one from u_s. However, it is clear that the signal σ is not measured and cannot be directly applied to design the sliding variable. One possible approximation is given by

$$\hat{\sigma}(t) = L_f(s)e(t) := \frac{L(s)}{F(\tau_f s)}e(t)\,, \tag{4.2}$$

where the approximation filter $F^{-1}(\tau_f s)$ is a low pass filter with $F(\tau_f s)$ being a

[1]It means that the relative degree is one around the relay, i.e., from the sliding variable (relay input) to the relay output.

Hurwitz polynomial in $\tau_f s$ with order $n^* - 1$ and unit DC gain given by $F(\tau_f s) := (\tau_f s + 1)^{n^*-1}$.

Therefore the sliding variable $\tilde{\sigma}$ is defined as,

$$\tilde{\sigma} := \hat{\sigma} - \bar{\sigma}\,, \tag{4.3}$$

where $\bar{\sigma}$ is the output of the prediction error loop and satisfies:

$$\dot{\bar{\sigma}} = -a_m \bar{\sigma} - \kappa_m (u_0 - u_0^{av})\,, \tag{4.4}$$

where $a_m, \kappa_m > 0$ are design constants. The control law is given by

$$\begin{aligned} u_s &= u_{nom} - u_0^{av}\,, & (4.5)\\ \tau_{av}\dot{u}_0^{av} &= -u_0^{av} + u_0\,, & (4.6)\\ u_0 &= -\varrho(t)\mathrm{sgn}(\tilde{\sigma})\,, & (4.7) \end{aligned}$$

where u_{nom} is the nominal control law, initially designed with the knowledge of the nominal parameters of the plant (which could be set to zero, i.e. $u_nom \equiv 0$), ϱ is the modulation function, $\tilde{\sigma}$ is the sliding variable and u_0^{av} is the filtered signal of the switching control u_0. It is worth to mention that, for a sufficient small time constant τ_{av}, u_0^{av} is an approximation of the extended equivalent control $(u_0)_{eq}$, when an ideal sliding mode occurs [55].

4.1.2 Prediction Error and the ISS Property

The following lemma can be stated.

Lemma 4.1 (ISS property from u_0^{av} to $\bar{\sigma}$)**.** *Consider the $\bar{\sigma}$-dynamics (4.4) with $u_0 := -\varrho(t)sgn(\tilde{\sigma})$ and averaging control u_0^{av} in (4.6). Then, (4.4) is ISS with respect to u_0^{av} and the following inequality holds*

$$|\bar{\sigma}(t)| \leq k_{\bar{\sigma}} \kappa_m \tau_{av} |u_0^{av}(t)| + \pi_{\bar{\sigma}}\,, \tag{4.8}$$

where $\pi_{\bar{\sigma}} := \beta_{\bar{\sigma}}(|\bar{\sigma}(0)|)e^{-\lambda_{\bar{\sigma}} t}$, $\beta_{\bar{\sigma}} \in \mathcal{K}_\infty$, $0 < \lambda_{\bar{\sigma}} < a_m$ and $k_{\bar{\sigma}} > 0$ are appropriate constants.

Proof: From (4.6), one has that $u_0 - u_0^{av} = \tau_{av}\dot{u}_0^{av}$, then the prediction error dynamics can be rewritten as $\dot{\bar{\sigma}} = -a_m\bar{\sigma} - \kappa_m\tau_{av}\dot{u}_0^{av}$. By defining the auxiliary signal $\sigma_a := \kappa_m\tau_{av}u_0^{av} + \bar{\sigma}$, one also has that $\dot{\sigma}_a = -a_m\sigma_a + a_m\kappa_m\tau_{av}u_0^{av}$. Consequently, the σ_a-dynamics is ISS w.r.t. u_{av}, with a small gain $\kappa_m\tau_{av}$, and (4.8) holds. ∎

4.1.3 Existence of Ideal Sliding Mode

The realization of the ideal sliding modes are important to ensure that *chattering* is avoided. In *SSC*, an ideal sliding surface is given by $\tilde{\sigma}(t) \equiv 0$.

Now, from (4.3) and (4.4) the sliding variable dynamics is given by:

$$\dot{\tilde{\sigma}} = -a_m\tilde{\sigma} - \kappa_m u_0^{av} + \kappa_m(u_0 + d_e)\,, \tag{4.9}$$

where $d_e := (a_m\hat{\sigma} + \dot{\hat{\sigma}})/\kappa_m$. By defining

$$\tilde{x} := \begin{bmatrix} \tilde{\sigma} & u_0^{av} \end{bmatrix}^T\,, \tag{4.10}$$

and from (4.6) and (4.9), one can write:

$$\dot{\tilde{x}} = A_\sigma\tilde{x} + B_\sigma u_0 + B_d d_e\,, \quad \tilde{\sigma} = C_\sigma\tilde{x}\,, \tag{4.11}$$

where $A_\sigma := \begin{bmatrix} -a_m & -\kappa_m \\ 0 & -1/\tau_{av} \end{bmatrix}$, $B_\sigma := \begin{bmatrix} \kappa_m & 1/\tau_{av} \end{bmatrix}^T$, $B_d := \begin{bmatrix} \kappa_m & 0 \end{bmatrix}^T$ and $C_\sigma := \begin{bmatrix} 1 & 0 \end{bmatrix}$. The system $(A_\sigma, B_\sigma, C_\sigma)$ is ASPR (Almost Strictly Positive Real) [56]. Indeed, since $C_\sigma B_\sigma = \kappa_m \neq 0$, then $(A_\sigma, B_\sigma, C_\sigma)$ has relative degree one. Moreover, by using the Rosenbrock system matrix, the triple $(A_\sigma, B_\sigma, C_\sigma)$ is minimum phase and can be easily shown [57]. Now, by adding and subtracting $B_\sigma k_0\tilde{\sigma} = B_\sigma C_\sigma k_0\tilde{x}$, one can write

$$\dot{\tilde{x}} = (A_\sigma + B_\sigma C_\sigma k_0)\tilde{x} + B_\sigma u_0 - B_\sigma k_0\tilde{\sigma} + B_d d_e\,, \tag{4.12}$$

where k_0 is the constant such that $(A_\sigma + B_\sigma C_\sigma k_0, B_\sigma, C_\sigma)$ is SPR. The existence of k_0 is assured by [56]. Indeed, for k_0 sufficiently large one has that $(A_\sigma + B_\sigma C_\sigma k_0, B_\sigma, C_\sigma)$ is SPR. Now, define $G_\sigma(s) := C_\sigma(sI - (A_\sigma + B_\sigma C_\sigma k_0))^{-1}B_\sigma$, $W_{d_e}(s) := C_\sigma(sI - (A_\sigma + B_\sigma C_\sigma k_0))^{-1}B_d$ and $W_{\tilde{\sigma}}(s) := -C_\sigma(sI - (A_\sigma + B_\sigma C_\sigma k_0))^{-1}B_\sigma k_0$. Then, one can write $\tilde{\sigma} = G_\sigma(s) * u_0 + W_{d_e}(s) * d_e + W_{\tilde{\sigma}}(s) * \tilde{\sigma} + \pi$, where π is an exponentially decaying term depending on the initial condition $\tilde{x}(0)$. Therefore, by defining the vanishing term $\pi_\sigma := G_\sigma^{-1}(s) * \pi$ one can further write

$$\tilde{\sigma} = G_\sigma(s) * (u_0 + d_{eq} + \pi_\sigma)\,, \tag{4.13}$$

where the *equivalent disturbance*

$$d_{eq} := G_\sigma^{-1}(s)W_{d_e}(s) * d_e + G_\sigma^{-1}(s)W_{\tilde{\sigma}}(s) * \tilde{\sigma}\,, \tag{4.14}$$

is such that $G_\sigma^{-1}(s)W_{d_e}(s)$ and $G_\sigma^{-1}(s)W_{\tilde{\sigma}}(s)$ are strictly stable and proper trans-

fer functions.

Lemma 4.2. *Consider the input/output relationship (4.13) where $G_\sigma(s)$ is SPR and $d_{eq}(t)$ is given by (4.14). Let $x_{\tilde{\sigma}}$ be the state of a stable, possibly nonminimal, realization of $G_\sigma(s)$. If $u_0 := -\varrho(t)sgn(\tilde{\sigma})$, where*

$$|\varrho(t)| \geq |d_{eq}(t)| + \delta\,, \tag{4.15}$$

with $\delta > 0$ been an arbitrary constant, then the inequality

$$|\tilde{\sigma}(t)| \text{ and } |x_{\tilde{\sigma}}(t)| \leq \pi_{\tilde{\sigma}}\,, \tag{4.16}$$

holds $\forall t \geq 0$, where $\pi_{\tilde{\sigma}} := \beta_{\tilde{\sigma}}(|x_{\tilde{\sigma}}(0)|)e^{-\lambda_{\tilde{\sigma}}t}$, $\beta_{\tilde{\sigma}} \in \mathcal{K}_\infty$, $0 < \lambda_{\tilde{\sigma}} < \lambda_{min}(G_\sigma(s))$ and $k_{\tilde{\sigma}} > 0$ is an appropriate constant. Moreover, there exists some finite time $t_e \geq 0$ such that $\tilde{\sigma}(t)$ becomes identically zero $\forall t \geq t_e$.

Proof: The proof follows the steps in [58, 59]. ∎

It must be highlighted that the plant nonlinearities affect the equivalent input disturbance d_{eq}. Moreover, despite of a filtered version of the VSC law be in fact applied to the plant input, it is guaranteed that no VSC robustness is lost, similarly to the *Integral Sliding Mode* control scheme proposed by [55]. The robustness is regarded w.r.t. the sliding mode which occurs in the sliding surface $\tilde{\sigma} \equiv 0$, corresponding to an internal control loop (the prediction error loop).

4.1.4 SSC Modulation Function Design

From the definition of T_L in (2.19) and the ω_t-dynamics in (2.18) one can write

$$\dot{\omega}_t \;=\; -\frac{B}{J_t}(\omega_t - \frac{\omega_r}{pn}) - \frac{K_s}{J_t}\tilde{\theta} + \frac{T_a^V(\omega_t)}{J_t}\,. \tag{4.17}$$

Since, as usual in WECS applications, the flux of the IG stator is not available for feedback while the other state variables can be measured without significant difficulties. So, by considering that ω_t, ω_r and $\tilde{\theta}$ are available and assuming that the uncertain plant parameters are bounded by now constants, then one can obtain the available norm bound for the first time derivative of the turbine angular velocity:

$$|\dot{\omega}_t| \;\leq\; \bar{\omega}_t := k_{\rho 1}\left|\omega_t - \frac{\omega_r}{pn}\right| + k_{\rho 2}|\tilde{\theta}| + k_{\rho 3}\,, \tag{4.18}$$

where $k_{\rho 1} > |B/J_t|$, $k_{\rho 2} > K_s/J_t$ and $k_{\rho 3} > \bar{c}/J_t$ with $\bar{c}$ from assumption (**(Φ.II)**).

The modulation function is designed to satisfy (4.15), with d_{eq} in (4.14), and $d_e := (a_m\hat{\sigma} + \dot{\hat{\sigma}})/\kappa_m$. Therefore, a norm bound for d_{eq} mst be obtained. First, note

that the disturbance d_e satisfies

$$|d_e| \leq \frac{a_m}{\kappa_m}|\hat{\sigma}| + \frac{a_m}{\kappa_m}|\dot{\hat{\sigma}}| \leq \frac{a_m}{\kappa_m}\frac{b_{\rho 1}}{s+a_{\rho 1}}|e| + \frac{a_m}{\kappa_m}\frac{b_{\rho 2}}{s+a_{\rho 2}}|\dot{e}|\,,$$

where the last inequality comes from (4.2) by noting that one can obtain positive constants $a_{\rho 1}, a_{\rho 2}, b_{\rho 1}$ and $b_{\rho 2}$ such that $\left|\frac{L(s)}{F(\tau_f s)}e\right| \leq \frac{b_{\rho 1}}{s+a_{\rho 1}}|e|$ and $\left|\frac{L(s)}{F(\tau_f s)}\dot{e}\right| \leq \frac{b_{\rho 2}}{s+a_{\rho 2}}|\dot{e}|$, *modulo* exponentially decaying terms.

Moreover, since $G_\sigma^{-1}(s)W_{d_e}(s)$ and $G_\sigma^{-1}(s)W_{\tilde{\sigma}}(s)$ in (4.14) are strictly stable proper transfer functions, there exists positive constants c_e, a_e such that the equivalent disturbance d_{eq} satisfies

$$|d_{eq}(t)| \leq \frac{c_e}{s+a_e} * \left(K_{\rho 1}|e| + K_{\rho 2}|\dot{e}| + K_{\rho 3}|\tilde{\sigma}|\right), \tag{4.19}$$

Hence, by using the upper bound (4.18) and reminding that $\dot{e} = \dot{\omega}_t - \dot{u}$ one can design the modulation function in the form

$$\varrho = \frac{b_\rho}{s+a_\rho} * \left(K_{\rho 1}|e| + K_{\rho 2}(|\dot{y}_m| + \bar{\dot{\omega}}_t) + K_{\rho 3}|\tilde{\sigma}|\right) + \delta\,, \tag{4.20}$$

where $\delta > 0$ is an arbitrary constant.

4.2 Extremum Seeking Control

In this section, the optimization problem is addressed once the inner control loop strategy has already tackled the global practical tracking problem. Thus, this section provides an HCS control algorithm based on Extremum Seeking Control so that MPPT is achieved for the WECS dynamics, which belongs to the class of plants presented in Chapter 3. The strategy considered in this work is a perturbation-based version of ESC, such as in [60], but presents some variations when compared to this technique.

Although other ESC techniques do exist, such as periodic switching functions based ones, as provided in [61, 62], and Newton-based approaches for estimating the map Hessian , as presented in [63, 64], their usage is justified once the system‘s high frequency gain direction is uncertain or when the map presents big time delays, respectively. As it is not the case for this specific application, in this work, the usual perturbation-based ESC scheme as in [60, 65] and presented in figure 4.2 is used with an output-feedback variation considering the gradient estimate saturation on its formulation.

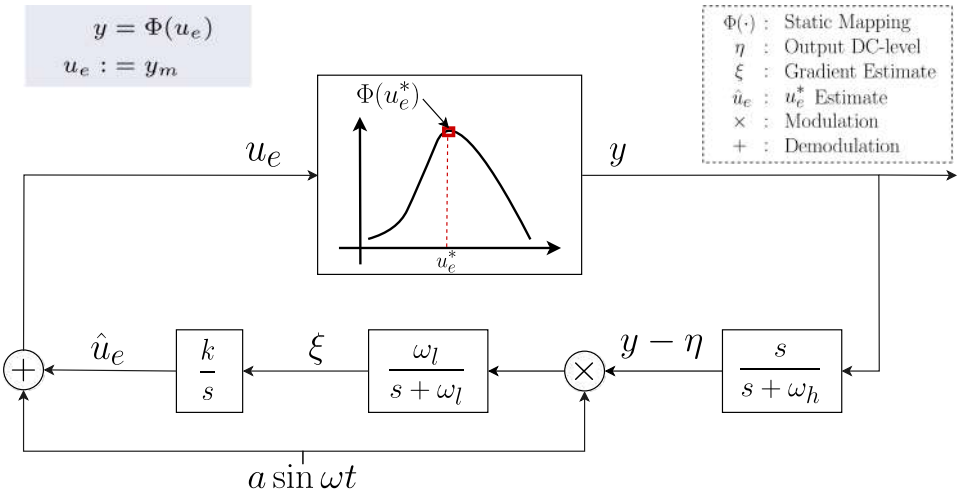

FIGURE 4.2: Extremum Seeking Control Topology.

4.2.1 ESC and the WECS Optimization Problem

Consider the input-output mapping previously stated on 3.3 and the assumptions made so that equation (3.14) could be written. The equations are rewritten here for the sake of the reader's better understanding.

$$y = \Phi(y_s(t)) \ = \Phi(u_e(t) + \mu_i(t)) + \mu_o(t)\,, \quad \forall t \geq 0$$

where u_e is the ESC control signal and $u_e := y_m$, meaning that the ESC control signal is the reference for the inner control loop to be tracked by the designed non linear robust controller. As a necessary condition for the results presented on this chapter to be valid, the tracking error on the inner loop μ_i needs to be limited to a residual set in neighborhood of zero as proved in Chapter 4.

Considering the static input-output mapping described in (3.3), the static mapping properties highlighted in (3.1.2) and assumptions **(Φ.I)** and **(Φ.II)**, the Extremum Seeking Control strategy is presented.

4.2.2 Estimator Implementation

In state space form, the "dirty derivative" appearing in the *auxiliary output*, defined in (3.18), used for *estimating the aerodynamic torque* can be implemented as:

$$\dot{x}_f = -\frac{1}{\tau_o}x_f + \frac{1}{\tau_o}\omega_t\,, \quad \zeta = -\frac{1}{\tau_o}x_f + \frac{1}{\tau_o}\omega_t\,. \tag{4.21}$$

It is clear, from (4.21), that ζ satisfies the following dynamics:

$$\dot{\zeta} = -\frac{1}{\tau_o}\zeta + \frac{1}{\tau_o}\dot{\omega}_t$$

Hence, the error signal $e_o = \dot{\omega}_t - \zeta$ satisfies the dynamics:

$$\dot{e}_o = -\frac{1}{\tau_o} e_o + \ddot{\omega}_t$$

since $\dot{\zeta} = -\frac{1}{\tau_o}\zeta + \frac{1}{\tau_o}\dot{\omega}_t = \frac{1}{\tau_o} e_o$.

Thus, if the aerodynamic torque is chosen as the auxiliary output y, one can further write:

$$y = J_t\zeta + T_L = J_t\dot{\omega}_t + T_L - Je_o = \Phi(\omega_t) - Je_o, \tag{4.22}$$

In the case that mechanical power is being used as the auxiliary output, the equations above turn into:

$$y = \omega_t \left(J_t\zeta + T_L\right) = J_t\dot{\omega}_t\omega_t + T_L\omega_t - J_t\omega_t e_o = \Phi(\omega_t) - J_t\omega_t e_o, \tag{4.23}$$

Since the signal $\ddot{\omega}_t$ is norm bounded then $|e_o|$ converges to a residual set of order $\mathcal{O}(\tau_o)$, which will be verified later on the text.

4.2.3 ESC Law

In the conventional ESC method [60] the control signal is composed by an estimated $\hat{\theta}$ for the maximizer θ^* added to a sinusoidal perturbation, i.e., $\hat{\theta}+a\,\sin(\omega t)$. Consider the perturbation-based extremum seeking control method described in [60, 65], but including an anti-windup control scheme around the ESC integrator, similar to [66]. while the outer loop is a version of the ESC approach of implemented with an anti-windup scheme. Here, it is considered a saturated version similar to [66] for the ESC law, named:

$$u_e(t) := \text{sat}\left(\hat{\theta}(t)\right) + a\,\sin(\omega t)\,, \tag{4.24}$$

where

$$\text{sat}\left(\vartheta\right) := \begin{cases} u_e^M\,, & \text{if} \quad \sigma \geq u_e^M\,, \\ u_e\,, & \text{if} \quad u_e^m \leq \vartheta \leq u_e^M\,, \\ u_e^m\,, & \text{if} \quad \vartheta \leq u_e^m\,, \end{cases} \tag{4.25}$$

and u_e^m , u_e^M are the constant lower and upper limits, respectively. The purpose of considering such a scheme (with saturation) is to avoid high absolute values on the gradient's estimate and introducing that peak back to the system's input. However, as previously stated and shown in 4.29 an anti-windup control strategy is necessary. Here, the auxiliary signal y is then given by:

$$y(t) := \Phi(\text{sat}\left(\hat{\theta}(t)\right) + a\,\sin(\omega t) + \mu_i) + \mu_o\,. \tag{4.26}$$

As in the conventional ESC method [60], the gradient of the function Φ evaluated at $\hat{\theta}$ is estimated by using the signal ξ, obtained via demodulation of the (washout) filtered version η of the output y, according to:

$$\dot{\eta} = -\omega_h \eta + \omega_h y \,, \tag{4.27}$$

$$\dot{\xi} = -\omega_l \xi + \omega_l (y - \eta) a \, \sin(\omega t) \,, \tag{4.28}$$

where ω_l, ω_h are design positive constants. An interesting alternative that could be tested in future work would be to consider an amplitude of $\frac{2}{a}$ on the demodulation that has been proven to improve the convergence rate of the ESC algorithm when compared to the classical approach. In [60], the estimate $\hat{\theta}$ is given by $\dot{\hat{\theta}} = k\xi \approx ka^2\Phi'(\hat{\theta})$, resulting in a dynamics having an asymptotically stable equilibrium point given by the maximizer $\hat{\theta} = \theta^*$. Here, as in [66], the estimate $\hat{\theta}$ is given by:

$$\dot{\hat{\theta}} = k[\xi + \xi_{aw}] \,, \quad \xi_{aw} := k_s[\text{sat}\,(\hat{\theta}(t)) - \hat{\theta}(t)] \,, \tag{4.29}$$

where $k_s > 0$ is the anti-windup gain and ξ_{aw} is the anti-windup error signal.

Simulation results are presented in Chapter 6, but before presenting them, an overall closed loop stability proof is given in Chapter 5.

Chapter 5

Closed Loop Stability Analysis

In this chapter, a complete analysis of the closed loop stability is performed considering the proposed strategy for the WECS. Some of the properties and assumptions detailed in Chapters 2, 3 and 4 are necessary to comples the proofs. By the end of this chapter, the main stability result is presented considering the WECS dynamics and the proposed ESC+SSC control scheme.

5.1 Tracking Error Convergence

The following lemma states the *tracking error convergence* property considering the inner control loop.

Lemma 5.1. *Assume that the reference signal y_m and its derivative $\dot{y}_m$ are $\mathcal{UB}$ and that the unimodality assumption of $\Phi(\cdot)$ holds. Consider the plant (2.9)–(2.12), (2.13) and (2.16)–(2.18) with state vector (3.15), output tracking error (3.4), SSC control law (4.5), (4.6), (4.7) with sliding variable $\tilde{\sigma}$ in (4.3), prediction error (4.4) and modulation function ϱ in (4.7) satisfying (4.15). Then, for sufficiently small time constants of the linear lead filter (τ_f) in (4.2) and the smooth filter (τ_{av}) in (4.6), the tracking error e converges to a small residual set of order $\mathcal{O}(\tau_{av}+\tau_f)$ and the following inequality holds*

$$|e(t)| \leq \mathcal{O}(\tau_{av}+\tau_f) + \pi_e\,, \tag{5.1}$$

where π_e is an exponential decaying term depending on the initial conditions. In addition, all closed-loop signals remain uniformly bounded.

Proof: From Lemma 4.1, the prediction error dynamics is ISS w.r.t. u_0^{av} with ISS gain $\tau_{av}\kappa_m$, according to (4.8). Thus, from (4.3), the surrogate $\hat{\sigma}$ for the ideal variable σ in (4.1) satisfies

$$|\hat{\sigma}(t)| \leq k_{\tilde{\sigma}}\kappa_m\tau_{av}|u_0^{av}(t)| + \pi_{\hat{\sigma}}\,, \tag{5.2}$$

where $\pi_{\hat{\sigma}} := \pi_{\bar{\sigma}} + \pi_{\tilde{\sigma}}$. Moreover, from (4.1) and (4.2) one can further write

$$\sigma - \hat{\sigma} = L(s)e - \frac{L(s)}{F(\tau_f s)}e = \frac{(1 - F(\tau_f s))}{sF(\tau_f s)}\dot{\sigma}.$$

Then, reminding that

$$F(\tau_f s) := (\tau_f s + 1)^{n^* - 1},$$

one can conclude that $\frac{(1-F(\tau_f s))}{sF(\tau_f s)}$ is a transfer function of order $\mathcal{O}(\tau_f)$ and the following inequality holds

$$|\sigma - \hat{\sigma}| \leq k_f \tau_f |\dot{\sigma}| + \pi_f \,, \tag{5.3}$$

where π_f is an exponential decaying term depending on the lead filter initial condition.

In the present case, the wind turbine dynamics (2.9)–(2.12), (2.13) and (2.16)–(2.18) with state vector (3.15) has relative degree $n^* = 4$ from the control input $u_s = \omega_0$ in (2.13) to the output ω_t. Moreover, the σ-dynamics can be written as

$$\dot{\sigma} = k_p(x,t)u_s + d(x,t) \,, \tag{5.4}$$

where k_p is the plant HFG and d is regarded as an input disturbance. However, from Property (2.4.3), one can conclude that the WECS dynamics is ISS w.r.t. the ideal variable norm ($|\sigma|$). Indeed, from Property (2.4.3), the WECS dynamics is ISS w.r.t. the vector $|\varepsilon|$ which contains the time derivatives of the turbine velocity ω_t up to the third order.

From (4.1), the ideal variable σ can be viewed as the input of the system described by differential equation

$$\dddot{e} + l_1\ddot{e} + l_2\dot{e} + l_3 e = \sigma.$$

Since $L(s)$ is a Hurwitz polynomial by design, then the e-dynamics is ISS w.r.t. σ. Moreover, one can subsequently write:

$$e = \frac{1}{L(s)}\sigma, \quad \dot{e} = \frac{s}{L(s)}\sigma, \quad \ddot{e} = \frac{s^2}{L(s)}\sigma \quad \text{and} \quad \dddot{e} = \frac{s^3}{L(s)}\sigma.$$

Hence, the tracking error e and its time derivatives $\dot{e}, \ddot{e}$ and $\dddot{e}$ are driven by σ.

Now, reminding that $e := \omega_t - y_m$ and that y_m in uniformly bounded by construction, then ω_t is driven by σ, *modulo* some constant. In addition, from (4.27), (4.28) one can verify that the η-dynamics and the ξ-dynamics are ISS w.r.t. ω_t. Consequently, from (4.29), the first time derivative of the ESC law (4.24) is driven by ω_t and, thus, $\dot{\omega}_t = \dot{y}_m - \dot{e}$ is driven by σ, modulo some constant. The second and third time derivatives of the ESC law also satisfy similar properties. Indeed, from (4.27), (4.28) and (4.29), the second time derivative of te ESC law is driven by ω_t.

So, $\ddot{\omega}_t = \ddot{y}_m - \ddot{e}$ is driven by σ. Finally, from (4.27), (4.28) and (4.29), one can verify that the third time derivative of the ESC law is driven by ω_t and $\dot{\omega}_t$, consequently, driven by σ.

Therefore, since from Property (2.4.3) the WECS dynamics is ISS w.r.t. $|\varepsilon|$, then the complete WECS state (3.15) norm is driven by σ. Then one can conclude that, given $R > 0$, there exists a positive constant k_R such that $|\dot{\sigma}| \leq k_R|\sigma| + k_R|u_0^{av}| + k_R + \pi_x$, $\forall |x(0)| < R$, where π_x is an vanishing term depending on the plant initial condition $x(0)$. Hence, from (5.3) one has

$$|\sigma - \hat{\sigma}| \leq k_f k_R \tau_f |\sigma| + k_f k_R \tau_f |u_0^{av}| + k_f \tau_f k_R + \pi_f + k_f \tau_f \pi_x \,. \tag{5.5}$$

Consequently, since $|\sigma| \leq |\hat{\sigma}| + |\sigma - \hat{\sigma}|$ and from (5.2), the following inequality is valid

$$(1 - k_f k_R \tau_f)|\sigma| \leq k_\tau(\tau_{av} + \tau_f)|u_0^{av}(t)| + \pi_\sigma + \mathcal{O}(\tau_f) \,, \tag{5.6}$$

provided $\tau_f < 1/(k_f k_R)$, where $\pi_\sigma := \pi_{\hat{\sigma}} + \pi_f + k_f \tau_f \pi_x$. By reminding $e = \frac{1}{L(s)}\sigma$, then one can conclude that the tracking error e, the upper bound for the turbine velocity $\bar{\dot{\omega}}_t$ in (4.18), the time derivative of the ESC law $\dot{y}_m$ are all driven by σ. Hence, since the averaging control (u_0^{av}) dynamics is ISS w.r.t. the modulation function $\rho(t)$ in (4.7) satisfying (4.15), then one can finally conclude that u_0^{av} and σ are uniformly norm bounded and, consequently, inequality (5.1) holds. In addition, since from Property (2.4.3) the WECS dynamics is ISS w.r.t. $|\varepsilon|$ then, the the WECS state is uniformly norm bounded. ∎

Hence, the *input disturbance* μ_i satisfies

$$|\mu_i(t)| \leq \pi_i(t) + \epsilon_i \nu_i(t),$$

with π_i being an exponentially decaying term depending on the initial conditions, ν_i an uniformly norm bounded function and $\epsilon_i > 0$ $(\tau_{av} + \tau_f)$ a small design parameter, see Lemma 5.1.

5.2 Estimation Error

Lemma 5.2. *Under the conditions stated on Lemma 5.1, the estimate ζ for the acceleration $\dot{\omega}_t$ is such that the estimation error $e_o = \dot{\omega}_t - \zeta$ converges to a small residual set of order $\mathcal{O}(\tau_o)$ not depend on the initial conditions and the following inequality holds*

$$|e_o(t)| \leq \mathcal{O}(\tau_o) + \pi_o \,, \tag{5.7}$$

for a sufficiently small time constant τ_o of the "dirty derivative" filter (4.21), where $\pi_o := \beta_o(|x_f(0)| + |T_L(0)|)e^{-\lambda_o t}$, $\beta_o \in \mathcal{K}_\infty$ and $0 < \lambda_o < 1$.

Proof: Indeed, from (2.18) one has that

$$J_t\ddot{\omega}_t = -\dot{T}_L + \frac{d}{d\omega_t}T_a^V(\omega_t)\dot{\omega}_t.$$

Thus, by the uniformly norm bound property in Lemma 5.1 one can conclude that $\ddot{\omega}_t$ is also uniformly norm bounded. Then, reminding that $\dot{\mu}_o = -\frac{1}{\tau_o}\mu_o - \ddot{\omega}_t/J_t$ one can write

$$\dot{\mu}_o = -\frac{1}{\tau_o}\mu_o - \ddot{\omega}_t/J_t$$

and note that the μ_o-dynamics is ISS w.r.t. $\ddot{\omega}_t$ with ISS gain τ_o, completing the proof. ∎

Therefore, from Lemma 5.2, the *output disturbance* μ_o satisfies

$$\mu_o(t) \leq \pi_o(t) + \epsilon_o\nu_o(t),$$

with π_o being an exponentially decaying term depending on the initial conditions, ν_o an uniformly norm bounded function and $\epsilon_o > 0$ (τ_o) a small design parameter.

Finally, one can verify that there exists a finite time $t_0 > 0$, such that $|\pi_i(t)| \leq \epsilon_i$ and $|\pi_o(t)| \leq \epsilon_o$, $\forall t \geq t_0$. Consequently, one can write that

$$\mu_i(t) = \epsilon_i\bar{\mu}_i(t)\,, \quad \mu_o(t) = \epsilon_o\bar{\mu}_o(t)\,, \quad \forall t \geq t_0\,, \tag{5.8}$$

where $\bar{\mu}_i \leq \pi_i/\epsilon_i + \nu_i$ and $\bar{\mu}_o \leq \pi_o/\epsilon_o + \nu_o$ satisfy $|\bar{\mu}_i(t)|, |\bar{\mu}_o(t)| \leq \mathcal{O}(1)$, $\forall t \geq t_0$, respectively.

5.3 Main Result

The following theorem states the overall stability analysis including both inner and outer control loops and the proposed estimation scheme.

Theorem 5.1. *Consider the auxiliary output y in (3.18) and the input-output mapping $\Phi(\cdot)$ in (3.13) with input disturbance $\mu_i = e$ satisfying (5.1) and output μ_o satisfying (5.7). The ESC law (4.24), (4.27), (4.28) and (4.29) is implemented with operating frequency ω, $k = \omega\epsilon k'$, $k_s = \omega\epsilon k_s'$, $\omega_l = \omega\epsilon\omega_l'$ and $\omega_h = \omega\epsilon\omega_h'$, where ϵ is a positive design constant and $k', k_s', \omega_l', \omega_h'$ are positive constants of order $\mathcal{O}(1)$. The SSC law of the inner loop is implemented with averaging filter time constant $\tau_{av} = \omega\epsilon$ and the "dirty derivative" time constant $\tau_o = \omega\epsilon$. Then, there exist ϵ^* and a^* such that for all $\epsilon \in (0, \epsilon^*)$ and $a \in (0, a^*)$, the vicinity of the maximizer of the input-output mapping (3.13) is attractive and the oscillations around the maximum can be made sufficiently small of order $\mathcal{O}(a) + \mathcal{O}(\epsilon)$, with a given in (4.24).*

Proof: The proof is carried out by applying the Averaging Theorem [40]. It is well known that the resulting system needs to be be periodic w.r.t. to the time variable and that can be obtained by setting the small parameter to zero. The proof here considers aperiodic time varying signals. However, these signals appears multiplied by the small parameter in the averaging analysis. So, when this small parameter vanishes, only time-varying periodic signals remain, allowing the usage of the Averaging Theorem [40]. The complete proof follows:

Introducing the error variables $\tilde{\theta} := \hat{\theta} - \theta^*$ and $\tilde{\eta} := \eta - \Phi(\theta^*)$, one can obtain from (4.27), (4.28) and (4.29) the *Error System* defined as:

$$\dot{\tilde{\eta}} = -\omega_h \tilde{\eta} + \omega_h (y - \Phi(\theta^*)) \,, \tag{5.9}$$

$$\dot{\xi} = -\omega_l \xi + \omega_l (y - \tilde{\eta} - \Phi(\theta^*)) a \, \sin(\omega t) \,, \tag{5.10}$$

$$\dot{\tilde{\theta}} = k\xi + k k_s [\text{sat}\,(\tilde{\theta} + \theta^*) - \tilde{\theta} - \theta^*] \,, \tag{5.11}$$

with y in (4.26). By applying Taylor series expansion for function Φ at $sat(\hat{\theta})$, the auxiliary output y in (4.26) can be rewritten as

$$y(t) = \Phi(sat(\hat{\theta}(t)) + \Phi^{'}(sat(\hat{\theta}(t))(a \, \sin(\omega t) + \mu_i) + \frac{1}{2}\Phi^{''}(sat(\hat{\theta}(t))(a \, \sin(\omega t) + \mu_i(t))^2 + \ldots + \mu_o(t),$$

which can be rewritten as ($\forall t \geq 0$):

$$\begin{aligned} y(t) = \Phi(sat(\hat{\theta}(t)) + \Phi^{'}(\text{sat}\,(\hat{\theta}(t)) a \, \sin(\omega t) + \\ + a^2 p_i(\text{sat}\,(\hat{\theta}(t)), a, t) + \mu_i q_i(\text{sat}\,(\hat{\theta}(t)), a, t) + \mu_o \,, \end{aligned} \tag{5.12}$$

where q_i is a norm bounded function collecting all the terms that contain μ_i while p_i is a norm bounded function T-periodic in t which incorporates all terms independent of μ_i.

Now, let $k = \omega \epsilon k^{'}$, $k_s = \omega \epsilon k_s^{'}$, $\omega_l = \omega \epsilon \omega_l^{'}$ and $\omega_h = \omega \epsilon \omega_h^{'}$, where ϵ is a positive design constant and $k^{'}, k_s^{'}, \omega_l^{'}, \omega_h^{'}$ are positive constants of order $\mathcal{O}(1)$. In addition, let $t_0 \geq 0$ be such that (5.8) holds with constants $\epsilon_i = \omega\epsilon$ and $\epsilon_o = \omega\epsilon$.

Hence, $\forall t \geq t_0$, the auxiliary output $y(t)$ satisfies

$$y(t) = \Phi(\text{sat}\,(\hat{\theta})) + \Phi^{'}(\text{sat}\,(\hat{\theta})) a \, \sin(\omega t) + a^2 p_i + \epsilon\omega(\bar{\mu}_i q_i + \bar{\mu}_o),$$

where some functions arguments were omitted to simplify the notation. Thus, the

error system composed by (5.9), (5.10) and (5.11), with state vector[1]

$$\mathcal{X} := \left[\begin{array}{ccc} \tilde{\eta} & \xi & \tilde{\theta} \end{array} \right]^T, \tag{5.13}$$

is given by $\dot{\mathcal{X}} = \epsilon\omega f(\mathcal{X}, t, \epsilon\omega)$ with $\mathcal{X}(t_0) = \mathcal{X}_0$ and

$$f = \left[\begin{array}{c} -\omega_h^{'}\tilde{\eta} + \omega_h^{'}(y - \Phi(\theta^*)) \\ -\omega_l^{'}\xi + \omega_l^{'}(y - \tilde{\eta} - \Phi(\theta^*))a\,\sin(\omega t) \\ k^{'}\xi + \epsilon\omega k^{'}k_s^{'}[\text{sat}\,(\tilde{\theta} + \theta^*) - \tilde{\theta} - \theta^*] \end{array} \right]. \tag{5.14}$$

Note that $f(\mathcal{X}, t, 0)$ is a T-periodic function in t. The Average System [40] for the system $\dot{\mathcal{X}} = \epsilon\omega f(\mathcal{X}, t, \epsilon\omega)$ is defined as the autonomous system

$$\dot{\mathcal{X}}_a = \epsilon\omega f_a(\mathcal{X}_a) := \epsilon\omega \int_{t_0}^{t_0+T} f(\mathcal{X}_a, t, 0)dt,$$

with $\mathcal{X}_a(t_0) = \mathcal{X}_0$, $\mathcal{X}_a := \left[\begin{array}{ccc} \tilde{\eta}_a & \xi_a & \tilde{\theta}_a \end{array} \right]^T$ and $T = 2\pi/\omega$.

In order to prepare for obtaining the Average System, first multiply by $a\,\sin(\omega t)$. Now, using the identity $2\sin^2(\omega t) = 1 - \cos(2\omega t)$, one has that

$$y(t)a\,\sin(\omega t) = \Phi a\,\sin(\omega t) + \Phi^{'}\frac{a^2}{2}(1 - \cos(2\omega t)) + (a^3 p_i + \epsilon\omega a(\bar{\mu}_i q_i + \bar{\mu}_o))\,\sin(\omega t)$$

which holds, $\forall t \geq t_0$, where once again some functions arguments were omitted to simplify the notation.

Therefore, considering $\epsilon\omega = 0$, the following relationships can be obtained

$$\begin{aligned} \int_{t_0}^{t_0+T} y(t)dt &= \Phi(\text{sat}\,(\hat{\theta})) + a^2 p_i^a(\text{sat}\,(\hat{\theta})) \\ \int_{t_0}^{t_0+T} y(t)a\,\sin(\omega t)dt &= \Phi^{'}(\text{sat}\,(\hat{\theta}))\frac{a^2}{2} + a^3\bar{p}_i^a(\text{sat}\,(\hat{\theta})), \end{aligned}$$

where the evaluation of $\hat{\theta}, \xi$ and η in the integrals were considered fixed and

$$\begin{aligned} p_i^a(\hat{\theta}) &:= \int_{t_0}^{t_0+T} p_i(\text{sat}\,(\hat{\theta}(t)), a, t)dt \\ \bar{p}_i^a(\text{sat}\,(\hat{\theta})) &:= \int_{t_0}^{t_0+T} p_i(\text{sat}\,(\hat{\theta}(t)), a, t)\,\sin(\omega t)dt, \end{aligned}$$

are uniformly norm bounded continuous functions of $\hat{\theta}$. Now, from (5.14) one can

[1]Here, the error state vector is not considering inner loop variables, their effect are taken into account by both input and output disturbances, μ_i and μ_o, respectively. A proof for Global Stability would require a Singular Perturbation Analysis of the complete space-state error system.

obtain the Average System with:

$$f_a = \begin{bmatrix} -\omega_h^{'}\tilde{\eta}_a + \omega_h^{'}(\Phi(\cdot) - \Phi(\theta^*) + a^2 p_i^a(\cdot)) \\ -\omega_l^{'}\xi_a + \omega_l^{'}(\Phi^{'}(\cdot)\frac{a^2}{2} + a^3\bar{p}_i^a(\cdot)) \\ k^{'}\xi_a \end{bmatrix}, \tag{5.15}$$

where $\hat{\theta}_a = \tilde{\theta}_a + \theta^*$ and the argument sat $(\hat{\theta}_a)$ were omitted to simplify the notation. The Average System has an equilibrium point at $\mathcal{X}_a^e := \begin{bmatrix} \tilde{\eta}_a^e & \xi_a^e & \tilde{\theta}_a^e \end{bmatrix}^T$. Indeed, from (5.15), $\mathcal{X}_a^e$ must satisfy

$$\begin{aligned} \xi_a^e &= 0, \\ \omega_l^{'}(\Phi^{'}(\text{sat}\,(\hat{\theta}_a^e))\frac{a^2}{2} + a^3\bar{p}_i^a(\text{sat}\,(\hat{\theta}_a^e))) &= 0 \\ -\omega_h^{'}\tilde{\eta}_a^e + \omega_h^{'}(\Phi(\text{sat}\,(\hat{\theta}_a^e)) - \Phi(\theta^*) + a^2 p_i^a(\text{sat}\,(\hat{\theta}_a^e))) &= 0, \end{aligned}$$

where $\hat{\theta}_a^e = \tilde{\theta}_a^e + \theta^*$. Thus, $\hat{\theta}_a^e$ is the solution of the following equation $(\Phi^{'}(\text{sat}\,(\hat{\theta}_a^e)) = -2a\bar{p}_i^a(\text{sat}\,(\hat{\theta}_a^e)))$. This equation always has a solution for sufficiently small a. In fact, since θ^* is the maximizer of $\Phi(\cdot)$, then

$$\Phi^{'}(\text{sat}\,(\theta^*)) = \Phi^{'}(\theta^*) = 0$$

and $\Phi^{'}(\cdot)$ changes sign around θ^*. Moreover, since $\bar{p}_i^a$ is a bounded and continuous function a $|\bar{p}_i^a| \leq \mathcal{O}(a)$ in the vicinity of θ^*. Therefore, there exists $\hat{\theta}_a^e$ in the vicinity of θ^* such that the curves $\Phi^{'}(\text{sat}\,(\hat{\theta}_a^e))$ and $-2a\bar{p}_i^a(\text{sat}\,(\hat{\theta}_a^e)))$ intercept each other. Hence,

$$\tilde{\theta}_a^e = \mathcal{O}(a).$$

Finally,

$$\tilde{\eta}_a^e = (\Phi(\mathcal{O}(a) + \theta^*) - \Phi(\theta^*) + a^2 p_i^a(\mathcal{O}(a) + \theta^*)) = \mathcal{O}(a)$$

and the equilibrium point is

$$\mathcal{X}_a^e := \begin{bmatrix} \mathcal{O}(a) & 0 & \mathcal{O}(a) \end{bmatrix}^T.$$

By noting that the Jacobian of Average System at $\mathcal{X}_a^e$ is block-triangular one can verify that the condition

$$(\Phi^{''}(\text{sat}\,(\hat{\theta}_a))\frac{a^2}{2} + a^3(\bar{p}_i^a)^{'}(\text{sat}\,(\hat{\theta}_a))) = 0$$

assures that the Jacobian is Hurwitz. This condition holds for a sufficiently small. Hence, the Average System has an exponentially stable equilibrium point. This

guarantees that $\hat{\theta}$ converges to a vicinity of the maximizer by applying the Averaging Theorem [40]. ■

Remark. Uniform Signal Boundedness *From (3.13) and (5.8) one can verify that $y(t)$ is an $\mathcal{UB}$ signal since $\Phi(\cdot)$ is a continuous function with $\mathcal{UB}$ input. Hence, from (4.27) and (4.28) is is clear that η and ξ are also $\mathcal{UB}$. Finally, from (4.29), one can write $\dot{\hat{\theta}} = -kk_s\hat{\theta} + k\xi + kk_s sat(\hat{\theta})$. Thus, since ξ is a $\mathcal{UB}$ signal it implies that $\hat{\theta}$ is also $\mathcal{UB}$.*

Finally, considering the estimator implementation in section 4.2.2, one might use the calculated ''dirt derivative" of ω_t, the known, but possibly uncertain, values of J_t, K_s, B, p, n and the values ω_t, ω_r which are available for feedback, to reconstruct both the aerodynamic torque T_a^V and the mechanical power P_m. Once estimated, the cost function $\hat{\Phi}(\omega_t)$ is fed to the ESC algorithm so that, as per Lemma 5.2 and Theorem 5.1, the maximizer ω_t^* is calculated and given as set-point to the SSC control loop as shown in figure 3.1.

Chapter 6

Numerical Simulations

In this chapter, the results obtained via numerical simulations using MATLAB/Simulink are presented and discussed. In the first section, the WECS considering the proposed optimization and control scheme with a SSC inner loop and a ESC outer loop is simulated in different scenarios and the results are discussed in details.

TABLE 6.1: Simulation Parameters of the WECS Dynamics

Element	Value	Unit
ρ_a	1.225	kg/m^3
R	10	m
S	πR^2	m^2
J_t	100	$kg.m^2$
K_s	2×10^6	$N.m/rad$
B	5×10^5	$N.m.s/rad$
J	11.06	$kg.m^2$
n	20	Dimensionless
p	2	Dimensionless
L_m	143.36	mH
L_{ls}	3.20	mH
L_s	$L_m + L_{ls}$	mH
L_{lr}	3.20	mH
L_r	$L_m + L_{lr}$	mH
a_0	70.1557	Ω/H
a_1	0.2038	Ω/H^2
a_2	156.2483	H^{-1}
a_3	0.1870	Ω
a_4	0.0013	Ω/H

In order to illustrate the proposed control strategy, consider the electrical subsystem (2.9)–(2.12) and the mechanical subsystem (2.16)–(2.18) of the WECS dynamics. The used numerical values are given in Table 6.1 and were extracted from [33]. For more details on the description of each element, please refer to the acronyms

section in the beginning of this document. The a_i, $i \in [0, 4]$ parameters are obtained using equations (2.16).

6.1 Piecewise Constant Wind Speed

At first, in order to illustrate the results obtained and proved in Chapters 4 and 5 a piece-wise continuous wind speed is considered, whose profile is shown in figure 6.1. The goal is to provide a first result showing that the purposed control scheme is able to achieve MPPT for a constant wind speed, putting in evidence how the system adapts itself due to wind changes. For numerical reasons, in certain situations

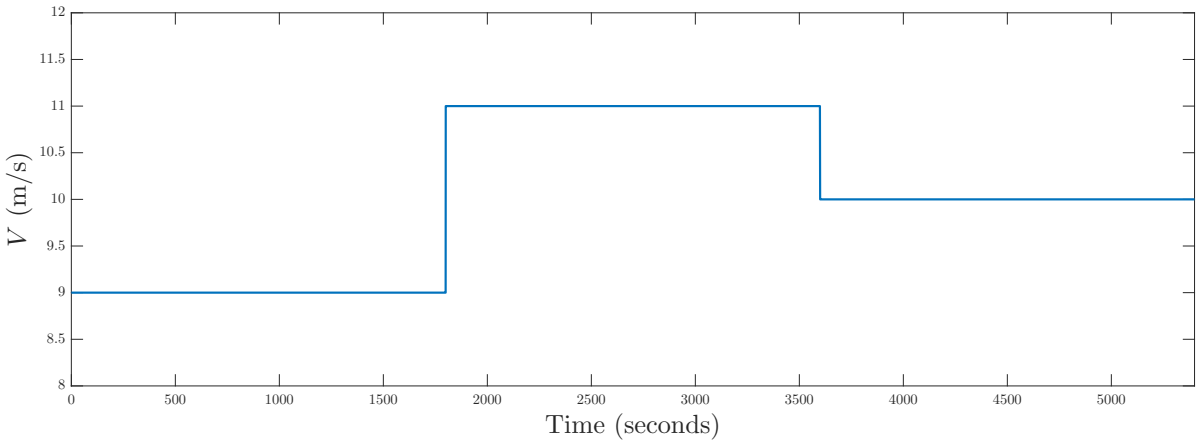

FIGURE 6.1: Piecewise Constant Wind Speed

SSC requires a very small simulation step to achieve a high commutation frequency necessary to "eliminate" the relative degree on the lead filter.

Thus, the two-layered controller tuning has been deliberated chosen slow so that simulation would not take much long. Tables 6.2 and 6.3 show the parameters used on both SSC and ESC controllers, respectively.

TABLE 6.2: SSC Parameters and Initial Conditions

Parameter	Value
τ_{av}	0.0960
$x_{av}(0)$	0
u_{nom}	0
a_m	1
κ_m	1
$x_m(0)$	0
$L(s)$	$(s+1)^4$
τ_f	0.01
$x_f(0)$	0
ϱ	150
$\sigma(0)$	0

TABLE 6.3: ESC Parameters and Initial Conditions

Parameter	Value
ω	0.1π
ω_l	$\omega/10$
$\xi(0)$	0
ω_h	$\omega/2$
$\eta(0)$	0
a	0.4
k	1
k_s	1
u_M	80
u_m	10
$\tau_o(0)$	0
$x_o(0)$	0
$\hat{\theta}(0)$	20

6.1.1 Inner Loop (SSC) and State Variables

First, figure 6.2 shows that the sliding variable remains on the manifold and, by consequence, $\hat{\sigma}$ remains in the neighborhood of zero while $\bar{\sigma}$ tracks the desired reference. Pictures on the right represent a time zoom so that more details can be checked.

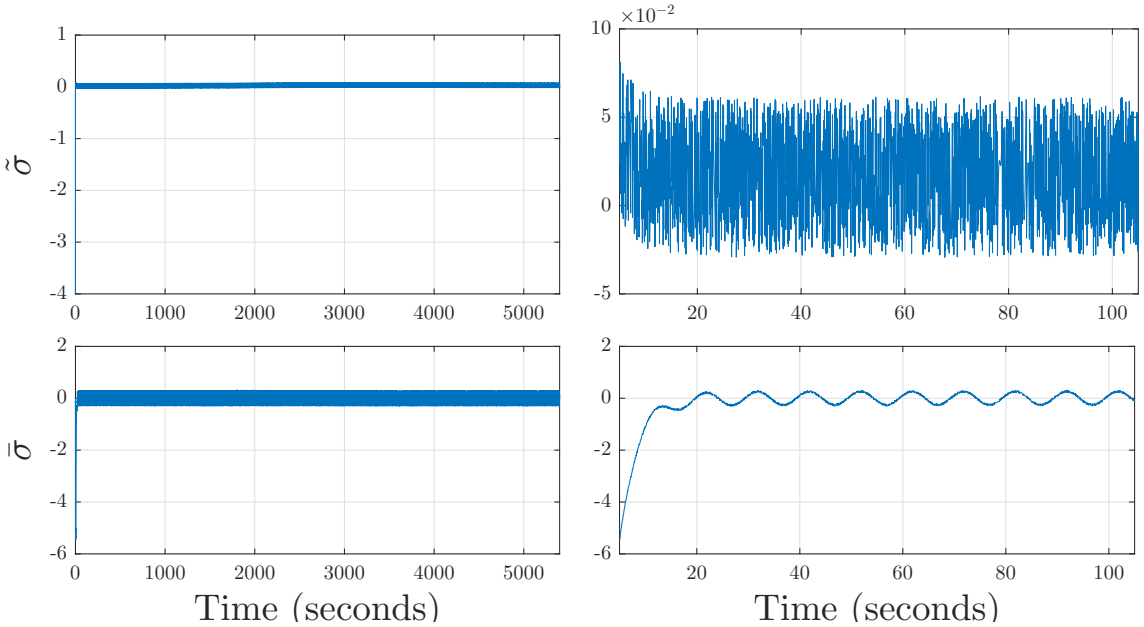

FIGURE 6.2: Sliding Surface

In figure 6.3 one might note the smooth control and commuted control signals, showing how the controller adapts due to initial conditions and/or wind changes.

In the next figures, the complete state's evolution over time - as described in Chapter 3 - is presented. In figure 6.4, one can see that the generator rotor speed $\omega_r/(pn)$ tracks the wind turbine angular speed ω_t as expected implying in a small $\tilde{\theta}$.

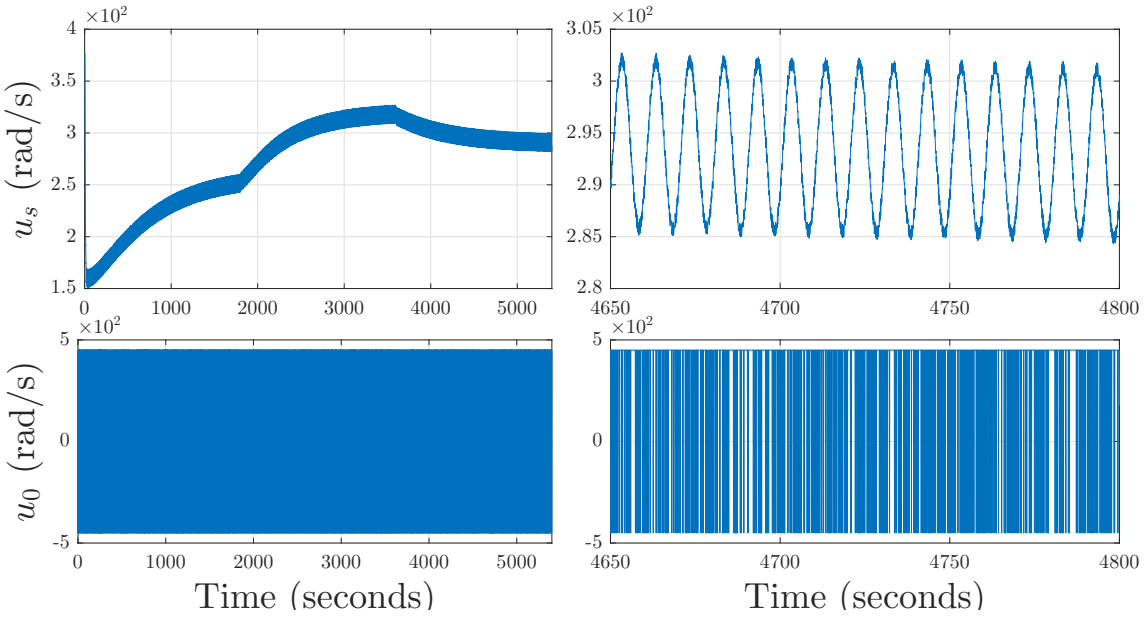

FIGURE 6.3: Control Signals

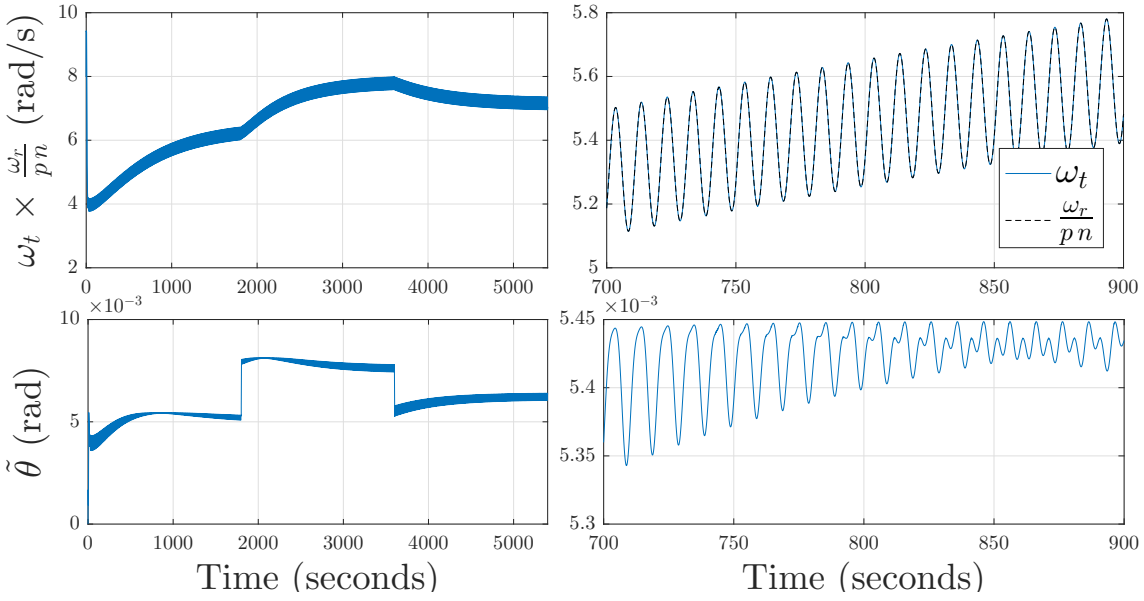

FIGURE 6.4: Rotor and Turbine speeds

The rotor angle θ_0 always increase due to the fact that ω_0 is its time-derivative and the control input, see figure 6.5. This does not represent an issue because θ_0 in terms of ISS because θ_0 enters into sines and cosines, hence limited, factors within the WECS dynamics.

Finally, considering the electrical part of the state vector, graphs in figure 6.6 show how flux and current are continuously adapted in order to maintain control.

6.1.2 Outer Loop (ESC) and MPPT

Now, the outer loop is considered. In figure 6.7, the ESC signals show how the Extremum Seeking Algorithm works, in terms of estimating the cost-function gra-

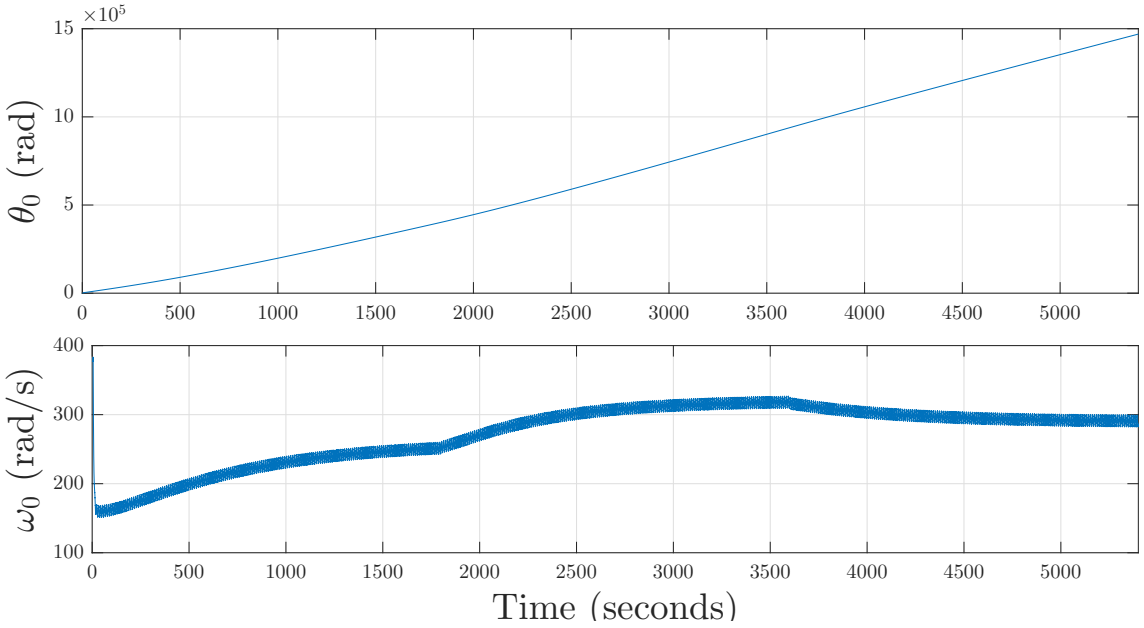

FIGURE 6.5: Rotor angle and stator frequency

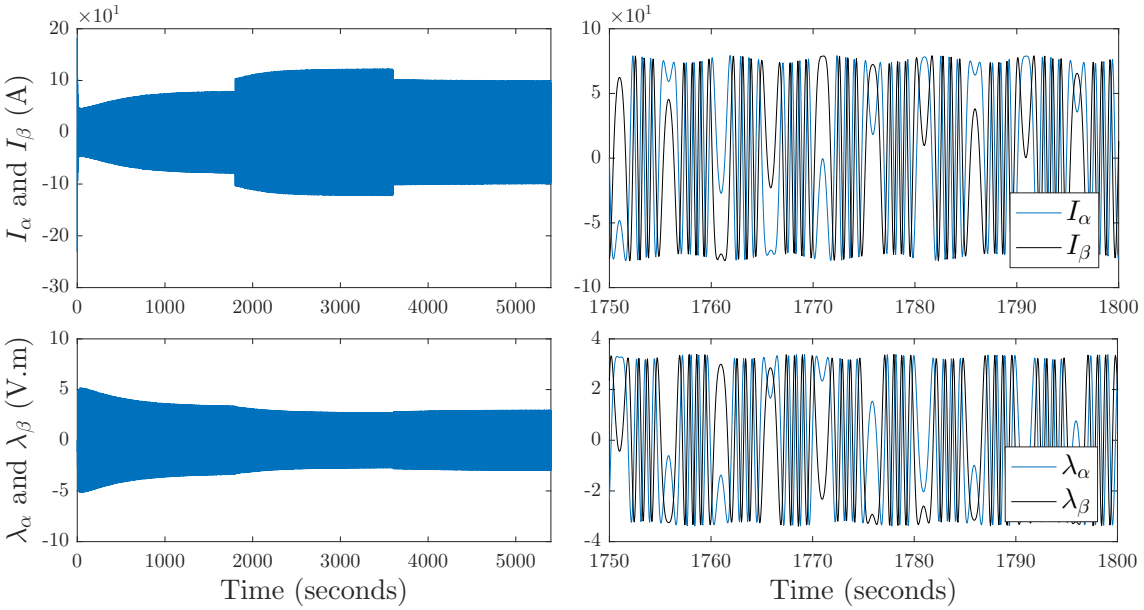

FIGURE 6.6: Currents and Flux

dient and then integrating it to find the optimal parameter that maximizes $\Phi(\cdot)$. Thus, from figure 6.7, it becomes clear that the ESC is performing as it is supposed to in both removing the DC-level via the high-pass filter and in estimating the outputs‘gradient after demodulation.

Finally, figure 6.8 shows the optimal value for the maximizer ω_t^* obtained through polynomial interpolation of the C_p-curve maxima, the ESC-calculated inner-loop setpoint y_m and the actual ω_t value. As shown in the figure, the wind turbine speed remains in a bounded neighborhood close to the maximizer ω_t^* and consequently, the power remains also close to its maximum once the dynamic response settles (see figure 6.9). The order of this error is given by the results presented in Chapter 5.

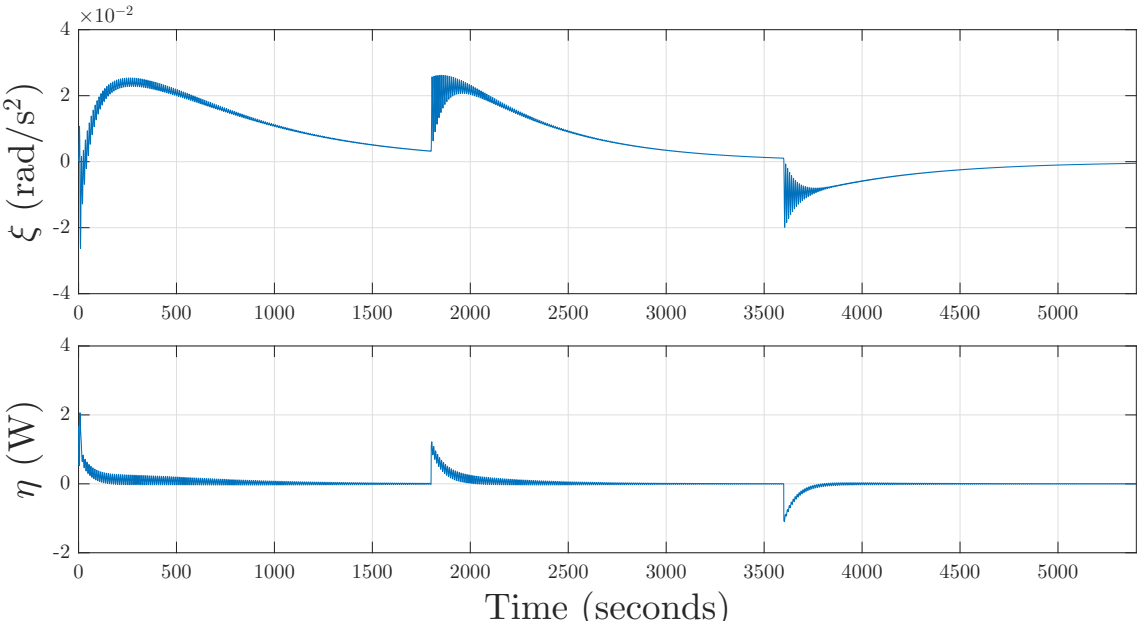

FIGURE 6.7: ESC Signals

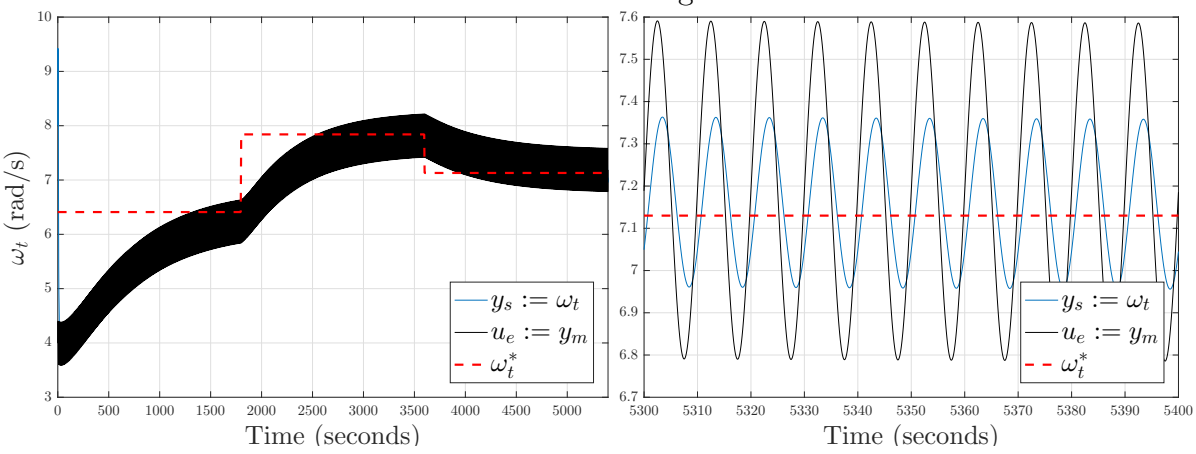

FIGURE 6.8: WECS MPPT

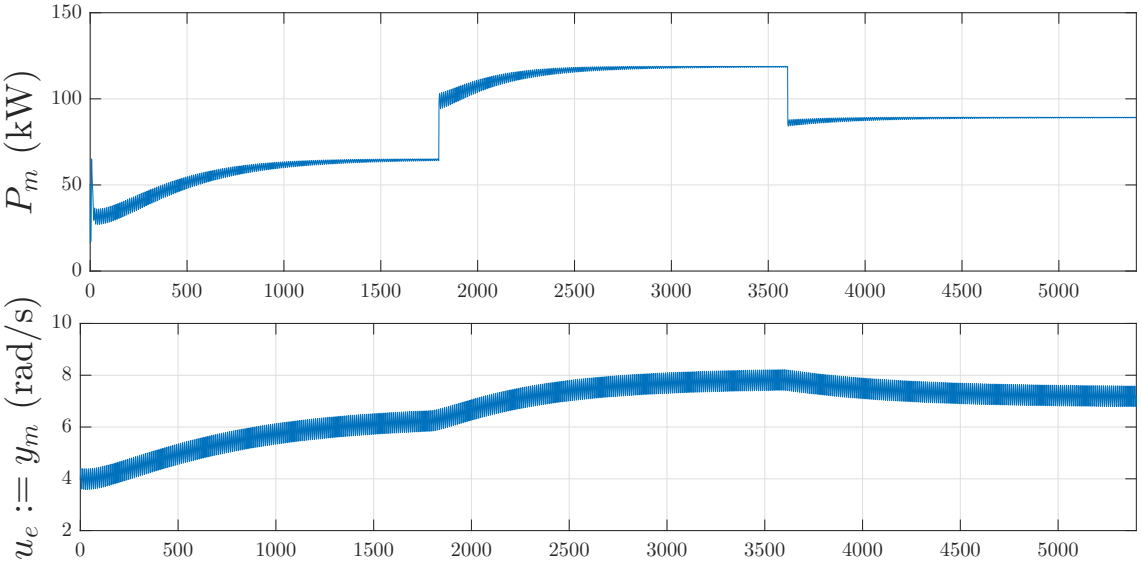

FIGURE 6.9: Mechanical Power

6.2 Variable Wind Signal

Also, real wind data was collected from [67]. The data collected represents more than three months (from 2010-11-10 to 2011-02-20) of real wind speeds measurements at each second. Smoother variations on the wind are considered in [68] and on the precious section, the goal here is to push the proposed scheme to its limits considering a more real scenario even though the lemmas and theorem presented in previous chapters were based on the hypothesis that the ESC cost-function was not time-varying.

In order to be able to achieve MPPT in the presence of this other type of wind speed profile, the ESC needs some new-tuning (given in table 6.4). Besides that, some of the electrical parameters have been slightly relaxed so that a higher simulation step could be achieved without causing numerical problems. Despite that slight change, the concepts remain the same and following results are extremely important:

TABLE 6.4: ESC Parameters and Initial Conditions

Parameter	Value
ω	100π
ω_l	$\omega/10$
$\xi(0)$	0
ω_h	$\omega/2$
$\eta(0)$	0
a	0.4
k	8
k_s	1
u_M	80
u_m	10
$\tau_o(0)$	0
$x_o(0)$	0
$\hat{\theta}(0)$	20

For simulation purposes, the whole dataset would be is too much, so, a hundred-minutes time window with enough wind variation to capture wind gusts and other abrupt speed changes was chosen. This data is represented in figure 6.10 and will be considered on the simulation results of the following sections.

The validation of the inner control loop's performance is straightforward. The desired set-point y_m is given by the ESC law and the signal $y_s = \omega_t$ is available for feedback, so it is only necessary to evaluate the tracking error response over time and the control signal calculated by the SSC algorithm. However, in order to guarantee that the maximum of the (*unknown-by-the-controller*) $\Phi(.)$ function is being tracked, the reference signal has been generated by polynomial interpolation of the maxima as obtained in figures 2.8, 2.7, 2.6. Here, two cases are considered. In

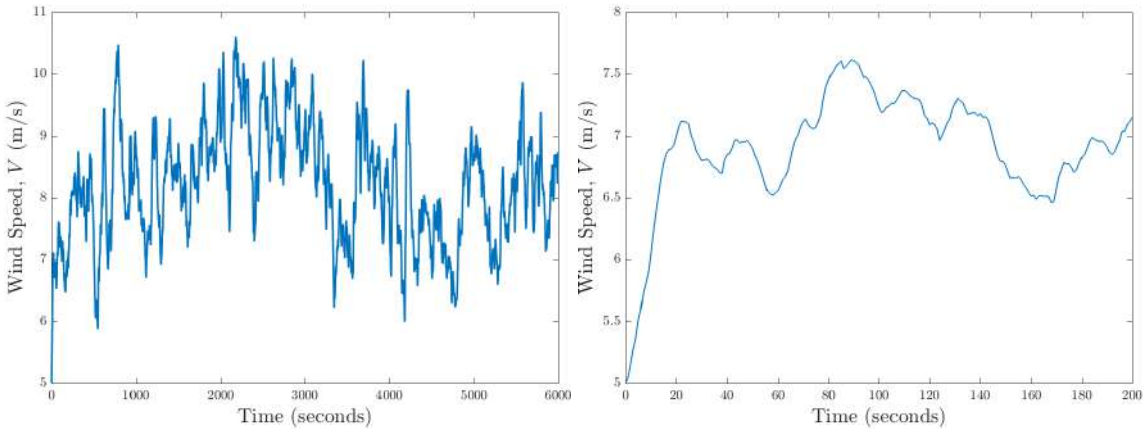

FIGURE 6.10: Real wind speed data during 1 hour and 40 minutes (left) and zoomed on the 200 first seconds

the first one, the estimated aerodynamic torque (T_a^V) is used as the static-mapping $\Phi(.)$. In the second one, estimated mechanical power (P_m) is used on the torque's place. The estimation error (in percentage) defined in equation 6.1 is also analyzed to prove that the estimation of Φ stays close to the its real value and then can be used as ESC's input signal.

$$\tilde{\Phi}_{\%} = 100 \times \frac{\mid \Phi - \hat{\Phi} \mid}{\Phi} \tag{6.1}$$

As explained in Chapter 3 choosing $\Phi(.) = C_p(\lambda)$ would require the knowledge of the C_i parameters in equation 2.6 and also a measurement or estimate of the wind speed, which is not the purpose of this study. The results and implications of using both torque and power as choices for $\Phi(.)$ are discussed in the following sections.

6.3 MPPT via Torque (T_a^V) Maximization

In this case, the aerodynamic torque is to be maximized by the proposed control strategy.

Tracking Problem First, analyzing the inner loop performance in figure 6.11, one can see on the up left corner, as proved in Chapter 4, that the tracking error $e := y_s - y_m = \mu_i$ stays in a bounded region for all times since the sliding surface is reached.

On the up right corner, the same simulation is zoomed in the time interval $t \in [0, 200]$ seconds so that it can be viewed that the controller takes approximately 30 seconds to drive the wind turbine angular speed from its initial condition to the desired set-point given by the ESC law. The control effort u_s is shown in the bottom of figure 6.11, pointing that the modulation function design was adequate since the controller is not saturating and the sliding is maintained for all times once the sliding

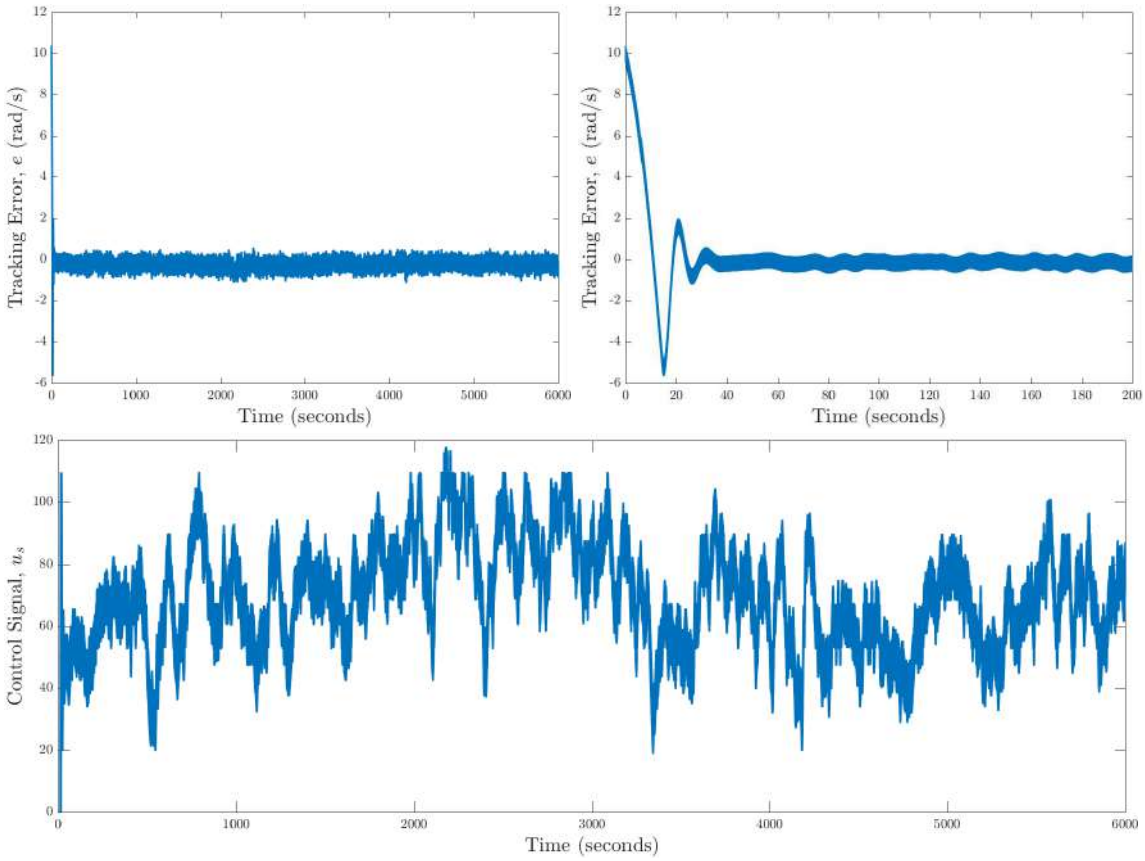

FIGURE 6.11: Turbine's angular speed tracking error e and control signal u_s for Torque Maximization.

surface is reached.

Optimization Problem Regarding the outer loop, its task is to provide to the inner loop, the maximizer w_t^* that makes Φ achieves each maximum for every wind speed within the sub-rated region. The first thing that must be analyzed is if the estimate $\hat{\Phi}$ is really providing a good approximation of Φ. Figure 6.13 shows the estimate error given by 6.1. The left image covers an error spectrum from 0-100%, but to better visualize that this error is not greater than 6%, the right image zooms into $\tilde{\Phi}_{\%} \in [0, 20]\%$.

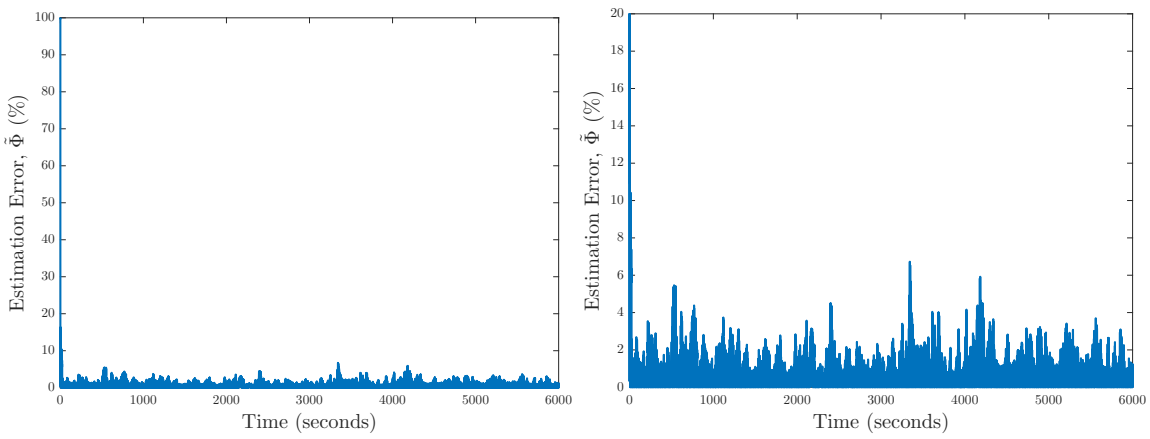

FIGURE 6.12: Error between on Φ and $\hat{\Phi}$ expressed in percentage of Φ.

Once the estimate can be trusted, the aerodynamic torque is provided as input signal to the ESC algorithm which calculates the adequate w_t^* that would maximize T_a^V. Figure 6.13 presents Φ's maximum point (in that case torque) tracking showing what would be the optimal trajectory to always have maximum torque no matter the wind speed. It can be seen from 6.13 that the ESC algorithm is really efficient on bringing the turbine's angular speed to close to the optimal one so that almost at all times the maximum torque is extracted. As before, the right side of figure 6.13 zooms into the first 200 seconds to provide more details about the tracking.

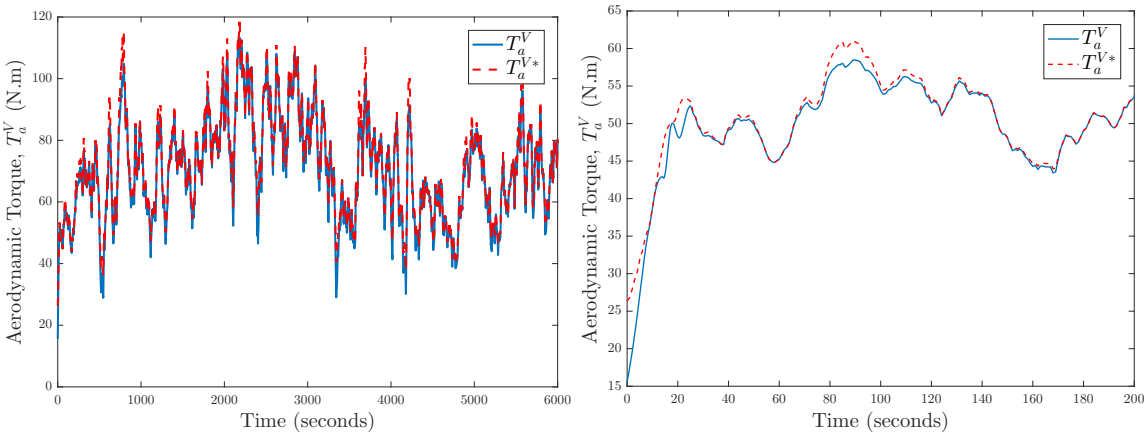

FIGURE 6.13: Tracking maximum aerodynamic torque.

One might note that all reference trajectories presented from this moment on will always be above the actual Φ since they represent the theoretical limit imposed by the system as explained in Chapter 2.

Although the objective of tracking maximum torque has been achieved, the goal here is to capture as much power as possible from the wind's kinetic energy. As explained in Chapters 2 and 3, this is achieved by exploiting the maximum power coefficient (C_p) and consequently achieving the highest mechanical power (P_m) possible. At a first glance, figures 2.8, 2.7, 2.6 seem to imply that maximum torque (T_a^{V*}) yields to maximum power (P_m^*). However, analyzing in more details the polynomial fitting for the maxima in these two different cases, one can see that these maxima occur with different maximizers (w_t^*).

Thus, as can be seen in figures 6.14 and 6.15, using the maximizers calculated for torque maximization yield to suboptimal performance on MPPT.

Fortunately, the proposed control scheme and the theorems presented here are also valid considering the mechanical power as the static mapping to be maximized ($\Phi = P_m$). These results are discussed in the next section.

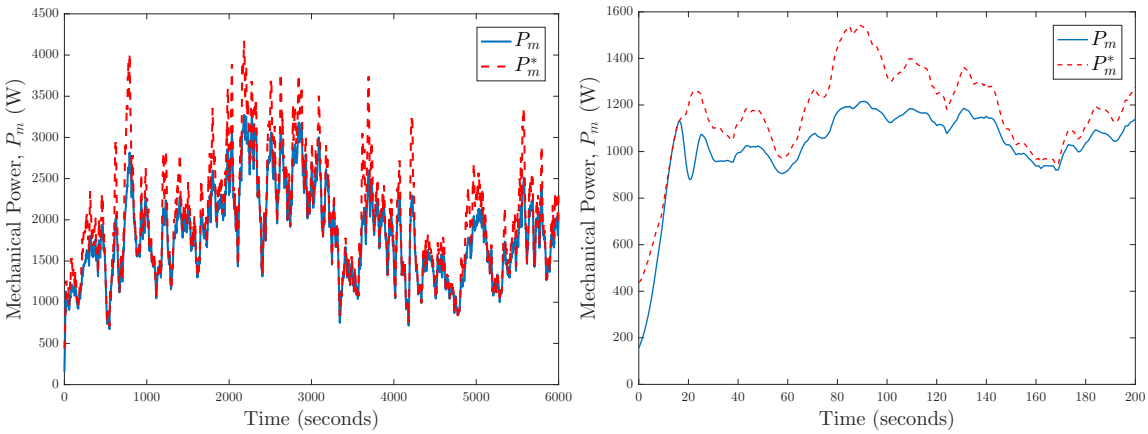

FIGURE 6.14: Implication on power tracking.

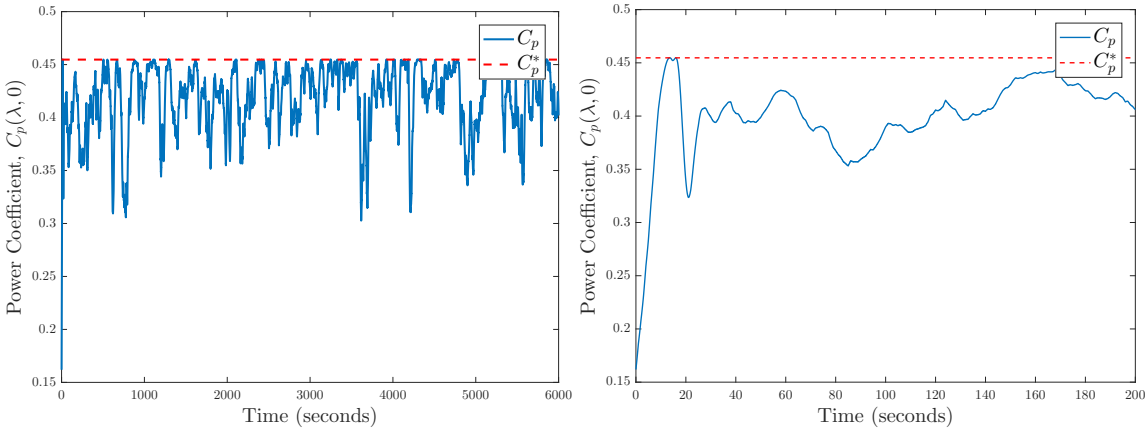

FIGURE 6.15: Implication on the power coefficient.

6.4 MPPT via Power (P_m) Maximization

Tracking Problem Once again the analysis starts on the inner loop performance. As the SSC controller remains the same and the same nature of reference signal is being applied to the inner loop, very similar behavior is evidenced in figure 6.16. Thus, the same comments from previous section apply here.

Optimization Problem Now, it is not expected that the torque actually follows its desired maximum trajectory and figure 6.17 does prove that. However, in this case, both profiles for P_m and C_p follow their correspondent maximum trajectories and that happens because $P_m^*(t) \Leftrightarrow C_p^*(t)$ for the same set of maximizers $w_t^*(t),\ \forall t$.

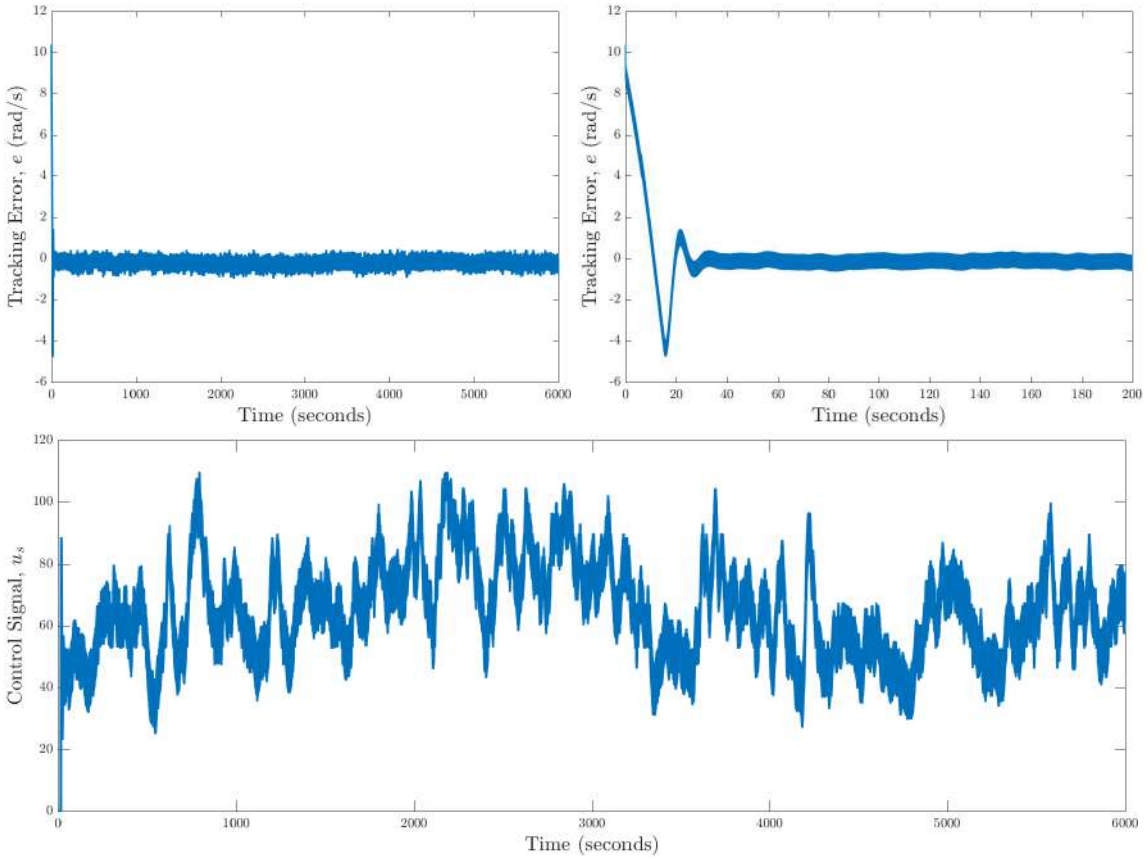

FIGURE 6.16: Turbine's angular speed tracking error e and control signal u_s for Power Maximization.

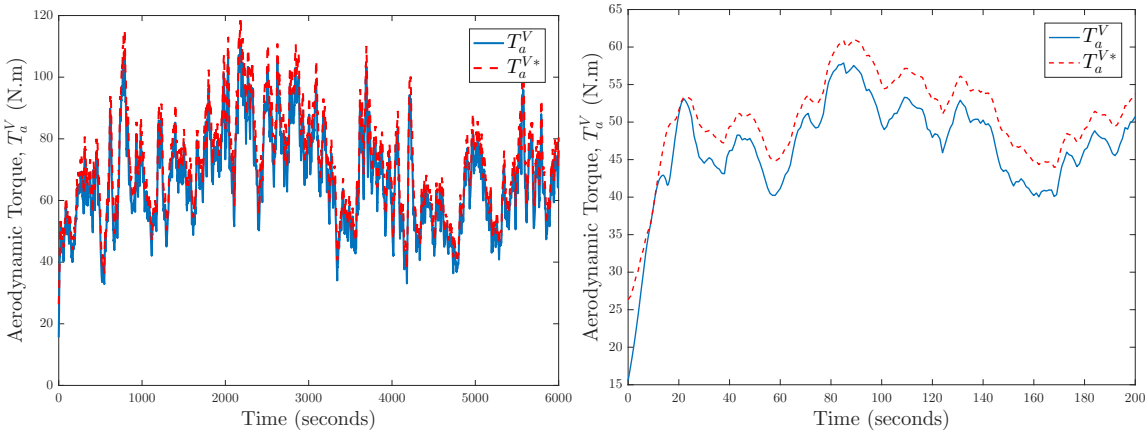

FIGURE 6.17: Not-tracking the maximum aerodynamic torque.

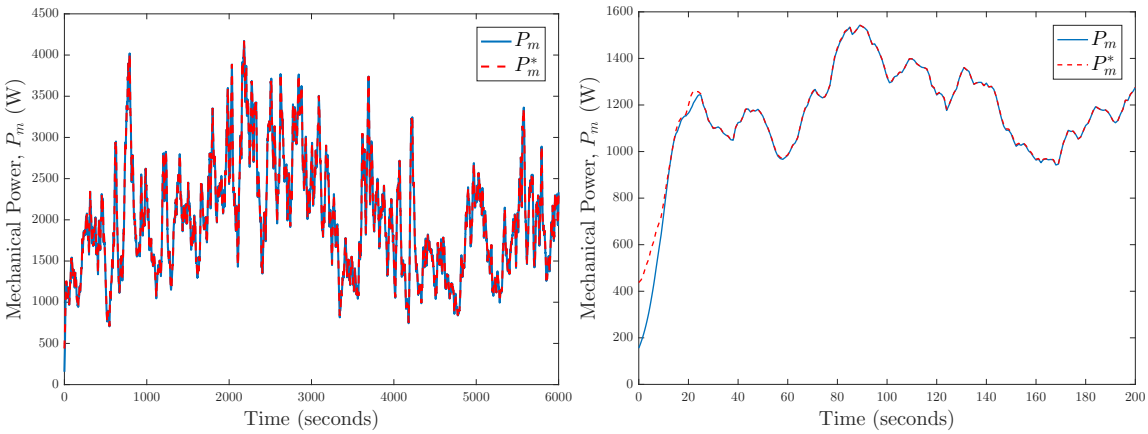

FIGURE 6.18: Tracking maximum mechanical power.

Figures 6.18 and 6.19 show that the maximum power point is tracked almost perfectly during the whole duration of the simulation scenario. Once more, the right images give more detailed visual information about the tracking.

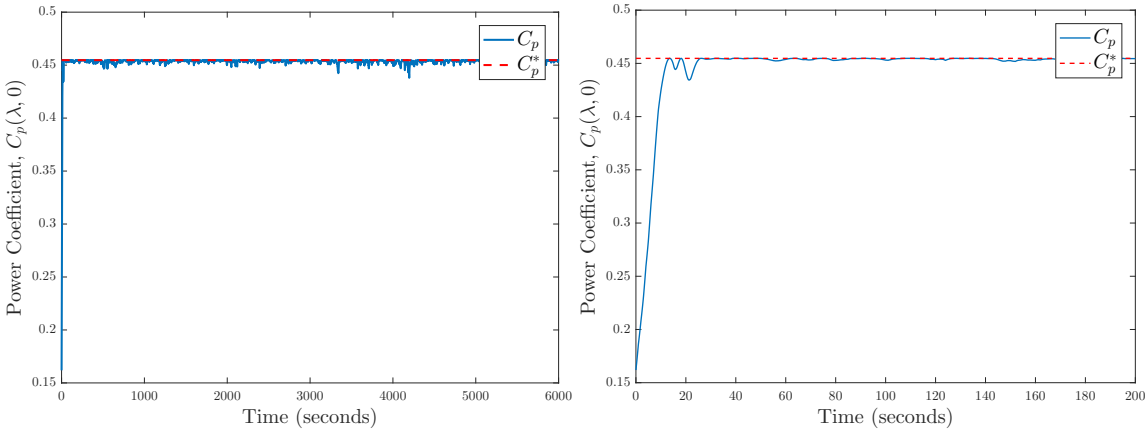

FIGURE 6.19: Achieving maximum power coefficient.

6.5 Robustness Analysis

In order to test the robustness of the proposed scheme, it is necessary to introduce some inaccuracies into the model so that both the inner and outer loop are tested in uncertain situations. The results presented on the following have been obtained by increasing 12% of J_t, decreasing 8% of B, increasing 10% of K and increasing 17% of R. The same SSC and ESC controllers were used.

Regarding the tracking error, figure 6.20 there is still good performance on keeping ω_t at the desired variable set-point. However, one might note that, in some moments, the control signal is saturated, achieving the maximum defined by the modulation value. In these exact moments, naturally, the tracking error increases but the controller can still bring it down because it doesn't spend too much time in this scenario. However, a better solution would be to increase a little the modulation function value so that the controller could overcome all disturbances due to

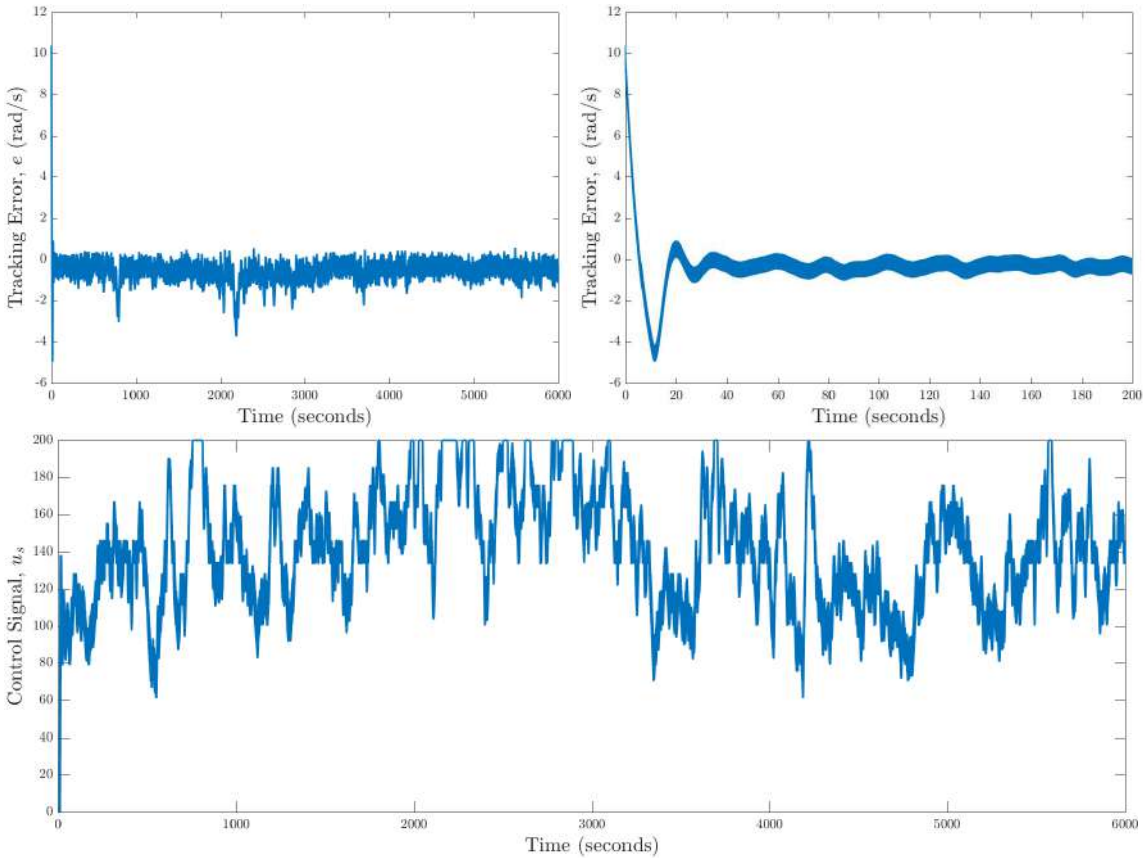

FIGURE 6.20: Robustness analysis: Turbine's angular speed tracking error e and control signal u_s for Power Maximization.

uncertainties at all times. For a better tuning of the modulation function value, it would be necessary a more detailed study on the magnitude of all disturbances.

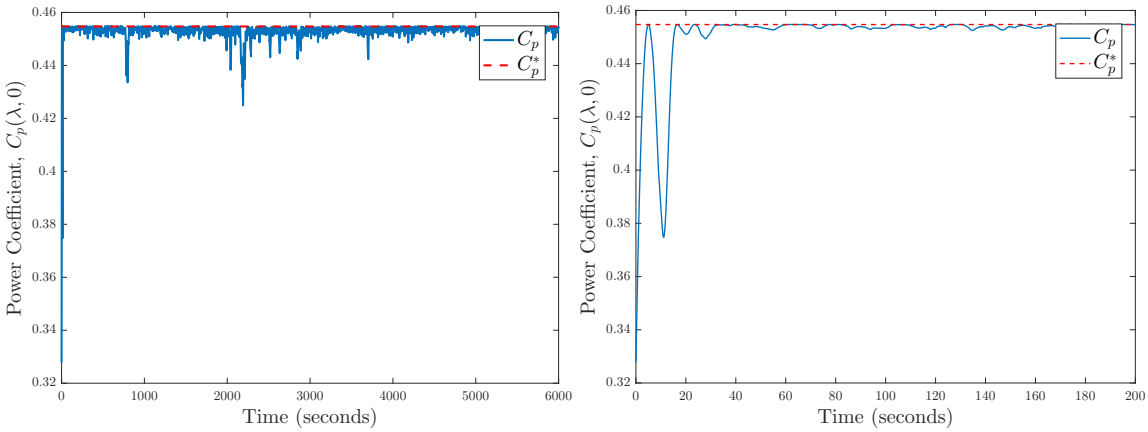

FIGURE 6.21: Robustness analysis: Mechanical power tracking

Considering maximum power tracking, one can see in figure 6.21 that the ESC algorithm is still capable of maintaining C_p close to its optimum. However, from both graphs in figures 6.21, there are more variability around the optimum introduced by the non-idealities. This shows that the proposed scheme is robust enough to still accomplish its task providing good results even in uncertain scenarios, but it has certainly a better performance once the errors on the estimates of J_t, B, K_s and R

are minimized.

To conclude, as per all the results presented, it is clear that the control signal remains on a limited region, taking acceptable values and having a coherent profile to track the changes on the inner control loop reference (the ESC signal). Regarding the aerodynamic torque or power estimation, it can be seen that, even considering noise on the measurement of the angular velocity, the estimation is acceptable. This implies that ω_t tracks almost perfectly y_m and that the ESC can practically consider a static I/O mapping $\Phi(y_m)$ as $y = T_a^V(\omega_t)$ *or* $P_m(\omega_t) \approx \Phi(y_m)$. These signals are all bounded and confirm that the SSC is tracking the reference signal as well as that the estimation error is bounded within the vicinity of zero.

Chapter 7

Conclusion

This chapter summarizes the work presented on the document while also pointing out its scientific contribution. The limitations of the present work are also discussed and, finally, a list of possible future works in order to continue and improve this study is presented.

7.1 Summary

In this study, the control of a wind energy conversion system (WECS) to extract its maximum power or torque was considered. The optimization and control strategy was performed by applying extremum seeking control (ESC) in an outer control loop to perform the optimization and a nonlinear robust controller in an inner control loop to guarantee global practical tracking rotor speed tracking. It was proved that the WECS is input-to-state stable w.r.t. the turbine angular velocity and its time derivatives. For power or torque maximization, the key idea of the method is to maximize an auxiliary output which is an estimate of the mechanical power or aerodynamic torque, with a real-time control to handle wind speeds varying from the cut-in wind speed to the rated wind speed (i.e. Phase II in figure 1.5).

A smooth sliding control (SSC), based on variable structure control (VSC) but applying a smooth control effort was implemented in the inner loop, resulting in a *chattering* free control law, without the need for stator flux measurements of the induction generator nor for wind speed measurement/estimation. The overall closed-loop stability analysis including the ESC employed in the outer loop and the SSC in the inner loop was provided.

Numerical simulations illustrated the performance of the proposed scheme. The WECS considered was a horizontal axis variable speed and fixed pitch wind turbine with a three blade rotor, which is the most usual type of wind turbine in the market. However, as explained throughout the text, the developed optimization and control strategy can be used for many different types of wind turbines, such as the

Darrieus turbines for the urban electricity generation for example, as long as the the same kind of mechanical transmission is considered, the generator is a Squirrel Cage Induction Generator (SCIG) and the power grid control side is performed by a Matrix Converter (MC).

7.2 Contributions

This study provides a useful method for maximum power point tracking in wind energy converting systems focusing on both theoretical aspects of the used controllers and their stability and robustness analysis and the practical application of the discussed techniques considering the whole mechatronic system. More specifically, this work contributes with a generalization of the SSC for the class of nonlinear plants considered here and the open loop stability (ISS) property obtained for this class of WECS, the overall closed loop stability analysis including the SSC and the ESC variation with anti-windup and the proposed scheme to estimate the mechanical power and/or aerodynamic torque. On the overall closed loop stability analysis, a different approach exploiting the ISS properties, considering calculated boundaries and controller limitations such as saturation and anti-windup has been taken into account for lemmas and theorem‘s ‘proofs in Chapter 5.

Additionally, the proposed scheme has two advantages when compared to other hill-climb search (HCS) controls on SCIGs such as [33–35]: The first is that the rotor flux is not necessary for feedback, avoiding hall-effect sensors or observers and the second is that one can use an estimate of the mechanical power or aerodynamic torque by means of the turbine's rotor speed only to feed the optimization portion of the algorithm, making it more flexible to conditions where the power signal is not available for feedback.

Some of the work presented on this text has been accepted and will be presented on the *American Control Conference* (ACC) taking place in Milwaukee - June, 2018 [68].

7.3 Future Work

Possible future topics of research are closely associated to limitations that are still present in this study. For instance, extending the stability results obtained to the general class of nonlinear plants presented in Chapter 3, formally establishing the parallel between other SMC-based controllers with SSC, extending the stability theorem using these controllers as inner loops and performing experiments with a prototype or real wind turbine to validate the simulations results obtained and test its real-time capabilities.

Finally, other improvements that would enrich this study would be dealing with the power grid-side controls and modulation algorithms notably for the MCs, simulating and verifying the proposed scheme performance for other type of wind turbines and simulating the whole system, with a state machine for handling operation modes and developing dedicated controllers for each power curve phase (cut-in, sub-rated, rated and cut-out).

Bibliography

[1] Global Wind Energy Council. Global wind statistics 2016, 2017.

[2] University of Michigan. Wind energy factsheet. *Center for Sustainable Systems*, (CSS07-09), 2017.

[3] Rene Bos. Self-starting of a small urban darrieus rotor. *Delft University of Technology*, 2012.

[4] Martin Kaltschmitt, Wolfgang Streicher, and Andreas Wiese. *Renewable energy: technology, economics and environment*. Springer Science & Business Media, 2007.

[5] Inverse Park Park and Inverse Clarke Transformations MSS Clarke. Software implementations user guide. *Microsemi Inc.*

[6] Roberto Cárdenas, Rubén Pena, Jon Clare, and Patrick Wheeler. Analytical and experimental evaluation of a wecs based on a cage induction generator fed by a matrix converter. *IEEE transactions on Energy Conversion*, 26(1):204–215, 2011.

[7] NL Panwar, SC Kaushik, and Surendra Kothari. Role of renewable energy sources in environmental protection: a review. *Renewable and Sustainable Energy Reviews*, 15(3):1513–1524, 2011.

[8] Ibrahim Dincer. Environmental impacts of energy. *Energy policy*, 27(14):845–854, 1999.

[9] Ibrahim Dincer and Marc A Rosen. *Exergy: energy, environment and sustainable development*. Newnes, 2012.

[10] Suaad Jaber. Environmental impacts of wind energy. *Journal of Clean Energy Technologies*, 1(3):251–254, 2013.

[11] John K Kaldellis and Dimitris Zafirakis. The wind energy (r) evolution: A short review of a long history. *Renewable Energy*, 36(7):1887–1901, 2011.

[12] Guy de Carmoy. The usa faces the energy challenge. *Energy policy*, 6(1):36–52, 1978.

[13] Ronald L Thomas and William H Robbins. Large wind-turbine projects in the united states wind energy program. *Journal of wind engineering and industrial aerodynamics*, 5(3-4):323–335, 1980.

[14] Paul Gipe. Wind energy comes of age california and denmark. *Energy Policy*, 19(8):756–767, 1991.

[15] James F Manwell, Jon G McGowan, and Anthony L Rogers. *Wind energy explained: theory, design and application*. John Wiley & Sons, 2010.

[16] World Energy Council. World energy resources 2016, 2016.

[17] Luis Barrios and Alejandro Rodriguez. Behavioural and environmental correlates of soaring-bird mortality at on-shore wind turbines. *Journal of applied ecology*, 41(1):72–81, 2004.

[18] Erin F Baerwald, Genevieve H D'Amours, Brandon J Klug, and Robert MR Barclay. Barotrauma is a significant cause of bat fatalities at wind turbines. *Current biology*, 18(16):R695–R696, 2008.

[19] R Saidur, NA Rahim, MR Islam, and KH Solangi. Environmental impact of wind energy. *Renewable and sustainable energy reviews*, 15(5):2423–2430, 2011.

[20] Albert Betz. Introduction to the theory of flow machines. 1966.

[21] Albert Betz. *Introduction to the theory of flow machines*. Elsevier, 2014.

[22] K. E. Johnson, L. Y. Pao, M. J. Balas, and L. J. Fingersh. Control of variable-speed wind turbines: Standard and adaptive techniques for maximizing energy capture. *IEEE Control Syst. Mag.*, 26(3):70–81, Jun. 2006.

[23] Jogendra Singh Thongam and Mohand Ouhrouche. MPPT control methods in wind energy conversion systems. *Fundamental and Advanced Topics in Wind Power*, pages 339–360, 2011.

[24] Azad Ghaffari, Miroslav Krstic, and Sridhar Seshagiri. Power optimization and control in wind energy conversion systems using extremum seeking. *IEEE Transactions on Control Systems Technology*, 22(5):1684–1695, sep 2014.

[25] S.M. Barakati, M. Kazerani, and J.D. Aplevich. Maximum power tracking control for a wind turbine system including a matrix converter. *IEEE Transactions on Energy Conversion*, 24(3):705–713, sep 2009.

[26] Rupp Carriveau. Fundamental and advanced topics in wind power. *InTech, Rijeka, Croatia*, 2011.

[27] M.A. Abdullah, A.H.M. Yatim, C.W. Tan, and R. Saidur. A review of maximum power point tracking algorithms for wind energy systems. *Renewable and Sustainable Energy Reviews*, 16(5):3220 – 3227, 2012.

[28] Umberto Ciri, Mario A Rotea, and Stefano Leonardi. Nested extremum seeking control for wind farm power optimization. In *American Control Conference (ACC), 2017*, pages 25–30. IEEE, 2017.

[29] Hui Li, KL Shi, and PG McLaren. Neural-network-based sensorless maximum wind energy capture with compensated power coefficient. *IEEE transactions on industry applications*, 41(6):1548–1556, 2005.

[30] MG Molina and PE Mercado. A new control strategy of variable speed wind turbine generator for three-phase grid-connected applications. In *Transmission and Distribution Conference and Exposition: Latin America, 2008 IEEE/PES*, pages 1–8. IEEE, 2008.

[31] Whei-Min Lin, Chih-Ming Hong, and Fu-Sheng Cheng. Fuzzy neural network output maximization control for sensorless wind energy conversion system. *Energy*, 35(2):592–601, 2010.

[32] Ahmed G Abo-Khalil and Dong-Choon Lee. Mppt control of wind generation systems based on estimated wind speed using svr. *IEEE transactions on Industrial Electronics*, 55(3):1489–1490, 2008.

[33] Azad Ghaffari, Miroslav Krstic, and Sridhar Seshagiri. Power optimization and control in wind energy conversion systems using extremum seeking. *IEEE Transactions on Control Systems Technology*, 22(5):1684–1695, sep 2014.

[34] M Godoy Simoes, Bimal K Bose, and Ronald J Spiegel. Fuzzy logic based intelligent control of a variable speed cage machine wind generation system. *IEEE transactions on power electronics*, 12(1):87–95, 1997.

[35] Ahmed G Abo-Khalil, Dong-Choon Lee, and Jul-Ki Seok. Variable speed wind power generation system based on fuzzy logic control for maximum output power tracking. In *Power Electronics Specialists Conference, 2004. PESC 04. 2004 IEEE 35th Annual*, volume 3, pages 2039–2043. IEEE, 2004.

[36] Quincy Wang and Liuchen Chang. An intelligent maximum power extraction algorithm for inverter-based variable speed wind turbine systems. *IEEE Transactions on power electronics*, 19(5):1242–1249, 2004.

[37] Mikihiko Matsui, Dehong Xu, Longyun Kang, and Zongqing Yang. Limit cycle based simple mppt control scheme for a small sized wind turbine generator system-principle and experimental verification. In *Power Electronics and Motion Control Conference, 2004. IPEMC 2004. The 4th International*, volume 3, pages 1746–1750. IEEE, 2004.

[38] Shengtie Wang, Zhiyuan Qi, and Tore Undeland. State space averaging modeling and analysis of disturbance injection method of mppt for small wind turbine generating systems. In *Power and Energy Engineering Conference, 2009. APPEEC 2009. Asia-Pacific*, pages 1–5. IEEE, 2009.

[39] Tobias Gybel Hovgaard, Stephen Boyd, and John Bagterp Jørgensen. Model predictive control for wind power gradients. *Wind Energy*, 18(6):991–1006, 2015.

[40] H. Khalil. *Nonlinear Systems*. Prentice Hall, 3 edition, 2002.

[41] L. Hsu, F. Lizarralde, and A.D. Araújo. New results on output-feedback variable structure adaptive control: design and stability analysis. *IEEE Trans. Aut. Contr.*, 42(3):386–393, 1997.

[42] P. Ioannou and K. Sun. *Robust Adaptive Control*. Prentice Hall, 1996.

[43] A. F. Filippov. Differential equations with discontinuous right-hand side. *American Math. Soc. Translations*, 42(2):199–231, 1964.

[44] Nguyen Phung Quang, Jörg-Andreas Dittrich, et al. *Vector control of three-phase AC machines*, volume 2. Springer, 2008.

[45] F Blaabjerg, Marco Liserre, and Ke Ma. Power electronics converters for wind turbine systems. 48:281 – 290, 10 2011.

[46] Boubekeur Boukhezzar. *Sur les stratégies de commande pour l'optimisation et la régulation de puissance des éoliennes à vitesse variable (in French)*. PhD thesis, Université Paris Sud-Paris XI, 2006.

[47] Magdi Ragheb and Adam M. Ragheb. *Fundamental and Advanced Topics in Wind Power*, chapter Wind Turbines Theory - The Betz Equation and Optimal Rotor Tip Speed Ratio, pages 19–38. InTech, 2011. 978- 953-307-508-2.

[48] Eduardo D Sontag. Smooth stabilization implies coprime factorization. *IEEE transactions on automatic control*, 34(4):435–443, 1989.

[49] Eduardo D Sontag. On the input-to-state stability property. *Eur. J. Control*, 1(1):24–36, 1995.

[50] Eduardo D. Sontag. *Input to State Stability*, pages 1–14. Springer London, London, 2013.

[51] Ying Tan, Yuping Li, and Iven M. Y. Mareels. Extremum seeking for constrained inputs. *IEEE Transactions on Automatic Control*, 58(9):2405–2410, sep 2013.

[52] L. Hsu. Self-oscillating adaptive systems (SOAS) whithout limit-cycle. In *Proc. American Contr. Conf.*, Albunquerque, 1997.

[53] A.J. Peixoto, F. Lizarralde, and L. Hsu. Further resutls on smooth sliding control of uncertain systems. In *Proceedings of the 2002 American Control Conference*, pages 2380 – 2385, Anchorage, AK USA, May 2002.

[54] A.J. Peixoto, F. Lizarralde, and L. Hsu. Experimental results on smooth sliding control of uncertain systems. In *Proceedings of the 2001 IEEE International Conference on Decision and Control*, pages 928 – 933, Orlando, Florida USA, 2001.

[55] V. I. Utkin. *Sliding Modes in Control and Optimization*. Springer-Verlag, 1992.

[56] Howard Kaufman, Itzhak Barkana, and Kenneth Sobel. *Direct Adaptive Control Algorithms*. Springer Nature, 1998.

[57] Giorgio Bartolini, Leonid Fridman, Alessandro Pisano, and Elio Usai, editors. *Modern Sliding Mode Control Theory*. Springer Berlin Heidelberg, 2008.

[58] L. Hsu. Variable structure model-reference adaptive control (vs-mrac) using only input and output measurements. ii. In *Decision and Control, 1988., Proceedings of the 27th IEEE Conference on*, volume vol.3, pages 2396–2401, Dec 1988.

[59] L. Hsu and F. Lizarralde. Redesign and stability analysis of I/O VS-MRAC systems. In *Proc. American Contr. Conf.*, pages 2725–2729, Chicago, 1992.

[60] M. Krstić and H.-H. Wang. Stability of extremum seeking feedback for general nonlinear dynamic systems. *Automatica*, 36(7):595–601, April 2000.

[61] Tiago Roux Oliveira, Liu Hsu, and Alessandro Jacoud Peixoto. Output-feedback global tracking for unknown control direction plants with application to extremum-seeking control. *Automatica*, 47(9):2029–2038, 2011.

[62] Tiago Roux Oliveira, Alessandro Jacoud Peixoto, and Liu Hsu. Global real-time optimization by output-feedback extremum-seeking control with sliding modes. *Journal of the Franklin Institute*, 349(4):1397–1415, 2012.

[63] Tiago Roux Oliveira and Miroslav Krstić. Newton-based extremum seeking under actuator and sensor delays. *IFAC-PapersOnLine*, 48(12):304–309, 2015.

[64] Tiago Roux Oliveira, Miroslav Krstić, and Daisuke Tsubakino. Extremum seeking for static maps with delays. *IEEE Transactions on Automatic Control*, 62(4):1911–1926, 2017.

[65] K. B. Ariyur and M. Krstic. *Real-Time Optimization by Extremum-Seeking Control*. John Wiley & Sons,Inc., 2003.

[66] Ying Tan, Yuping Li, and Iven M. Y. Mareels. Extremum seeking for constrained inputs. *IEEE Transactions on Automatic Control*, 58(9):2405–2410, sep 2013.

[67] UCAR/NCAR Earth Observing Laboratory. Pcaps isfs 1 second data. version 1.0. 2010-2011.

[68] A.J. Peixoto, D.P. Dias, G.F. Pacheco, and C.C. Neves. Smooth sliding control applied to power optimization via extremum seeking in variable speed wind turbines. In *Proc. American Contr. Conf.*, Milwaukee, 2018 (forthcoming).